Thermal expansion studies on low-dimensional frustrated quantum magnets: the case of κ-(BEDT-TTF)$_2$Cu$_2$(CN)$_3$ and azurite

Dissertation
zur Erlangung des Doktorgrades
der Naturwissenschaften

vorgelegt beim Fachbereich Physik
der Johann Wolfgang Goethe-Universität
in Frankfurt am Main

von
Rudra Sekhar Manna
aus Gobindapur Abad, Indien

Frankfurt am Main (2012)
(D30)

vom Fachbereich Physik der Johann Wolfgang Goethe-Universität als Dissertation angenommen.

Dekan: Prof. Dr. Michael Huth

Gutachter:

1. Prof. Dr. Michael Lang
2. Prof. Dr. Jens Müller

Datum der Disputation: 20.04.2012

Kurzfassung

Im Rahmen dieser Arbeit wurden bei sowohl Umgebungsdruck als auch unter hydrostatischem Druck Messungen der thermischen Ausdehnung durchgeführt. Diese physikalische Größe liefert wertvolle Informationen über die elektronischen, magnetischen und Gittereigenschaften eines Materials. Der Ausdehnungskoeffizient ist über folgende Beziehung mit der spezifischen Wärmekapazität verbunden - $\beta = \Gamma \cdot \kappa_T \cdot V_m^{-1} \cdot C_V$. Dabei ist β der Volumenausdehungskoeffizient, $\Gamma = C_V^{-1} \cdot (\partial S / \partial \ln V)_T$ die Grüneisenfunktion, welche die Volumenabhängigkeit (V) der im System vorhandenen Entropie S bestimmt, κ_T = -$(\partial \ln V / \partial P)_T$ die isotherme Kompressibilität, V_m das Molvolumen und C_V die spezifische Wärmekapazität bei konstantem Volumen. Dieser Grüneisenformalismus kann dazu angewandt werden die Volumenabhängigkeit der charakteristischen Energien (ϵ) eines Materials zu bestimmen, da Γ = -dlnϵ/dln$V$. Im Falle eines Phasenübergangs zweiter Ordnung kann darüberhinaus die Druckabhängigkeit der Übergangstemperatur (T_c) aus der Ehrenfestrelation gewonnen werden - vorausgesetzt die Beiträge des Volumenausdehnungskoeffizienten (β) und der spezifischen Wärmekapazität (C_P) sind bekannt. Besonders starke Auswirkungen auf den Ausdehnungskoeffizienten werden erwartet, wenn der Grüneisenparameter (Γ) groß ist oder sogar divergiert. Die leztgenannte Situation tritt bei Annäherung an einen Quantenphasenübergang oder einen kritischen Endpunkt bei endlicher Temperatur ein. Dies kann beispielsweise durch Anwendung von hydrostatischem Druck geschehen.

Verbindungen aus der Familie der quasi-zweidimensionalen Ladungstransfersalze κ-(ET)$_2$X (ET steht für BEDT-TTF), mit X = Cu(NCS)$_2$, Cu[N(CN)$_2$]Br and Cu[N(CN)$_2$]Cl sind Spin $S = 1/2$ Mott-Isolatoren, welche bei Variation des chemischen oder hydrostatischen Drucks ein vielfältiges Phasendiagramm offenbaren. Eine Besonderheit der sogenannten κ-Phase ist die Tatsache, dass jeweils zwei ET-Moleküle ein Dimer mit einer beträchtlichen Intradimer-Wechselwirkung bilden. Dementsprechend wurde die elektronische Struktur dieses Materials durch ein effektives Dimermodell beschrieben und

diskutiert. Bei diesen Verbindungen sind antiferromagnetische (AFM) und supraleitende (SC) Zustände voneinander durch eine s-förmige Mott Metall-Isolator Grenzlinie erster Ordnung getrennt, welche in einem kritischen Punkt zweiter Ordnung endet. Da diese Grenzlinie in κ-$(ET)_2Cu[N(CN)_2]Cl$ bei einem im Labor leicht zu realisierenden Druck von lediglich $\sim$ 30 MPa zugänglich ist, handelt es sich dabei um einen aussichtsreichen Kandidaten für die Untersuchung des kritischen Verhaltens in der Umgebung des Endpunkts. Allerdings gibt es von experimenteller Seite eine Kontroverse bezüglich der Universalitätsklasse des Mott-Übergangs in der Familie der κ-$(ET)_2X$ Ladungstransfersalze. Messungen der Leitfähigkeit sowie der Spin-Gitter-Relaxation geben Hinweise auf eine unkonventionelle Mott-Kritikalität. Andererseits fand man aus Messungen der thermischen Ausdehnung am deuterierten κ-$(ET)_2Cu[N(CN)_2]Br$ eine ebenfalls unkonventionelle Kritikalität, welche jedoch nicht mit einer der vorgeschlagenen Universalitätsklassen in Einklang zu bringen ist. Diese Schlussfolgerung basiert auf der Annahme, dass der Grüneisen-Skalierungsansatz gültig ist. Allerdings wurde vor kurzem eine Skalierungstheorie der Gittereffekte vorgeschlagen, welche bei endlichen Temperaturen und in der Umgebung des kritischen Endpunktes gültig ist. Von dieser Theorie ausgehend wurde gezeigt, dass die Grüneisenskalierung in der Umgebung eines kritischen Punktes bei endlichen Temperaturen zusammenbricht. Tatsächlich wurden ein beinahe divergierendes Verhalten und ein Vorzeichenwechsel des thermischen Ausdehnungskoeffizienten bei Annäherung an den kritischen Endpunkt vorhergesagt. Nach erneuter Analyse der Messdaten der thermischen Ausdehnung im Bezug auf eine Skalierungsfunktion wurde festgestellt, dass sie sich mit der 2D Ising Universalitätsklasse in guter Übereinstimmung befinden. Eine Messung der thermische Ausdehnung unter Druck wäre eine entscheidende Überprüfung dieser Annahme. Unter anderem um solche Messungen zu ermöglichen, wurde als Bestandteil dieser Arbeit eine Apparatur zur Messung der thermischen Ausdehnung unter hydrostatischem Druck aufgebaut.

Um dies zu ermöglichen wurde eine aus *CuBe* bestehende Druckzelle mit dem Volumen von 81,4 cm^3 konstruiert, welche die hochauflösende Dilatometerzelle mit einem Volumen von $\sim$ 20 cm^3 aufnehmen kann. Der maximal zulässige Druck für diese Zelle im Temperaturbereich von $T = 1{,}4$ K bis $T = 293$ K liegt bei 250 MPa. Zum Probenwechsel ist es nötig, den Verschluss an der Unterseite der Druckzelle, welcher die Dilatometerzelle, einen Drucksensor und die elektrischen Durchführungen beinhaltet, zu entfernen. Ein druckdichter Verschluss der Druckzelle wird durch eine Messing-beschichtete Metallquetschdichtung gewährleistet. Zur Herstellung von hydrostatischem Druck wird als Druckmedium (^4He) eingesetzt. Bei den ersten Experimenten wurde als Druckquelle ein Druckreservoir mit einem Volumen von 50.000 cm^3 in Kombination mit einem Heliumgaskompressor (Unipress Gas Compressor U11) verwendet, um Drücke von $P \leq 18$ MPa herzustellen. Bei dem benutzten Drucksensor handelt es sich um einen stark dotierten n-*InSb* Einkristall, welcher es ermöglicht mit dieser Apparatur die thermische Ausdehnung als Funktion der Temperatur bei verschiedenen konstanten Drücken mit einer Auflösung des Drucks von $\pm$ 0.1 MPa zu messen

Als zweiter Schwerpunkt dieser Arbeit ist die Untersuchung des κ-$(ET)_2Cu_2(CN)_3$-Systems, bei dem Frustrationseffekte eine wichtige Rolle spielen, zu nennen. Aufgrund der starken Quantenfluktuationen zeigt diese Verbindung bis hinunter zu Temperaturen im Millikelvinbereich keine langreichweitige magnetische Ordnung und wurde daher als guter Kandidat für einen Quanten-Spinflüssigkeitsgrundzustand vorgeschlagen. Aktuell von Interesse ist unter anderem die Frage nach der Art der tiefligenden Elementaranregungen, welche mit der bei 6 K beobachteten Anomalie - eine mögliche Spinflüssigkeitsinstabilität - zusammenhängen, welche sich in Messungen der spezifischen Wärmekapazität, der NMR Relaxationsrate der thermischen Leitfähigkeit äußert. Es gibt eine Reihe von Szenarien, die die 6 K Anomalie in Bezug auf Spinflüssigkeitsinstabilitäten erklären könnten. Darunter sind ein Crossover vom thermisch ungeordneten zum Quantenungeordneten Zustand, ein Phasenübergang verbunden mit der Bildung von Spinonen und die Exzitonenkondensation in der Nähe einer Z_2 Spinflüssigkeit aus bosonischen Spinonen. Mit Hilfe von Messungen der thermischen Ausdehnungs entlang der drei verschiedenen Achsen des monoklinen Systems konnte eine ausgeprägte und scharfe Anomalie bei 6 K beobachtet werden, welche stark an die Gitterfreiheitsgrade koppelt, also das Merkmal eines Phasenüberganges zeigt. Das Fehlen einer Hystere beweist, dass es sich um einen Phasenübergang zweiter Ordnung handelt. Der Ausdehnungskoeffizient innerhalb der (bc) Ebene zeigt klar anisotropes Verhalten, entsprechend einer signifikanten Verzerrung des Dreicksgitters. Die Ableitung der magnetischen Suszeptibilität nach der Temperatur zeigt ebenfalls eine deutliche Anomalie bei 6 K, was darauf hindeutet, dass die Spinfreiheitsgrade am Übergang beteiligt sind. Durch den Einsatz eines Grüneisen-Skalierungsansatzes wurde der entsprechenden Beitrag zur spezifischen Wärme, welcher ebenfalls eine deutliche Anomalie bei 6 K zeigt, berechnet. Die Änderung der Entropie am Phasenübergang legt nahe, dass Ladungsfreiheitsgrade am Übergang beteiligt sind. An dieser Verbindung kürzlich durchgeführte dielektrische Messungen zeigen Relaxor-artiges dielektrisches Relaxationsverhalten bei Temperaturen unter $\sim$ 60 K, was zufällig orientierte elektrische Dipole nahelegt. Diese Dipole könnten sich bei 6 K anordnen, was die Beteiligung der Ladungsfreiheitsgrade erklären könnte. Interessanterweise verhält sich der Volumenausdehungskoeffizient weniger ungewöhnlich und zeigt keine Anomalie bei 6 K. Nach der Ehrenfest-Relation deutet das Ausbleiben der Anomalie im Volumenausdehnungskoeffizienten darauf hin, dass die 6 K - Anomalie von hydrostatischem Druck unbeeinflußt bleibt. Da die supraleitende Sprungtemperatur dieser Verbindung unter endlichem Druck bei $T_c = 4{,}5$ K liegt, könnte es eine interessante Wechselbeziehung zwischen dem 6 K Phasenübergang und Supraleitung geben.

Basierend auf Muon-Spin-Relaxations-Experimenten an einer polykristallinen Probe wurde in der Literatur festgestellt, dass der Quanten-Spinflüssigkeitszustand von κ-$(ET)_2Cu_2(CN)_3$ in einem Magnetfeld instabil ist. Es hat sich herausgestellt, dass bereits ein sehr kleines magnetisches Feld von einigen mT ausreicht, um einen Quantenphasenübergang vom *QSL*-Zustand zur antiferromagnetischen (AFM) Phase mit stark unterdrücktem Moment zu verursachen. Dies kann als Bose-Einstein Kondensation von Spinanregungen mit einer extrem kleinen Energielücke ($\Delta_s(H) = 3{,}5$ mK) erklärt wer-

den. Bei Feldern von ungefähr 4 T wurde ein zweiter Quantenphasenübergang entdeckt, was auf ein "Deconfinement" der Spinanregungen hindeutet. Unsere Messungen zeigen eine starke Abhängigkeit der thermischen Ausdehnung entlang einer bestimmten kristallographischen Richtung des Magnetfeldes, nämlich der in der Ebene liegenden b-Achse, während die beiden anderen Achsen nicht vom Feld beeinflusst werden. Die Messergebnisse der relativen Längenänderung im Nullfeld zeigen übereinstimmend mit einem Vorzeichenwechsel des thermischen Ausdehnungskoeffizienten entlang der b-Achse ein um 8 K zentriertes, breites Minimum. Andereseits ist der Phasenübergang bei 6 K unempfindlich gegenüber magnetischen Feldern $B \leq 10$ T, der größten angelegten Feldstärke. Ein endliches Feld von 0.5 T $< B_c \leq 1$ T wird jedoch benötigt, um den Effekt beobachten zu können. Mit steigendem Feld wächst die Anomalie und sie verschiebt sich zu tieferen Temperaturen. Eine Besonderheit dieser B-induzierten Anomalie ist das unter-, bzw. überschwingende Verhalten oberhalb, bzw. unterhalb der Temperatur der Anomalie. Messungen der Magnetostriktion, *d.h.* der Längenänderungen in Abhängigkeit des Magnetfeldes bei konstanter Temperatur zeigen bei zunehmendem Magnetfeld zwei stufenartige Anomalien. Aus dem B-T Diagramm der Anomalie kann entnommen werden, dass die beiden Anomalien bei ungefähr 8,4 K verschmelzen. Interessanterweise liegt eine der beiden Anomalien in der Nähe der vor kurzem in der Literatur berichteten Phasengrenze zwischen quantentkrischer (QC_H) und schwach antiferromagnetischer (WAF_H) Phase. Dieses Phänomen erinnert an "Flux-Pinning Effekte", jedoch erscheint das Fehlen der Hysterese beim Aufwärmen und Abkühlen rätselhaft. Alternativ könnte man an feldinduzierte Kreisbewegungen der Elektronen denken, die die Hoppingamplituden beeinflussen und dadurch Auswirkungen auf die Austauschwechselwirkungen haben.

Temperaturabhängige strukturelle und elektronische Eigenschaften spielen für diese Spinflüssigkeitsverbindung ebenfalls eine wichtige Rolle. Basierend auf der Kenntnis der Kristallstruktur des Materials durch Einkristall-Röntgenbeugung im Temperaturbereich zwischen 5 K und 300 K wurde die elektronische Struktur durch Anwendung der Dichte-Funktional-Theorie und Tight-Binding Methoden ausgewertet. Es wird gezeigt, dass sich der Grad der Frustration und die Stärke der Wechselwirkung in Abhängigkeit der Temperatur signifikant ändern. Interessanterweise zeigt das Verhältnis t'/t, welches die Auswirkungen von Frustration in einem anisotropen Dreieck-Gitter bestimmt, eine Anomalie bei etwa 150 K. Beginnend bei Raumtemperatur steigt die Wechselwirkungsstärke (U/t) monoton beim Abkühlen an. Das Verhältnis zwischen c und b Gittervektoren als Funktion der Temperatur ändert sich signifikant. Gemäß der Dreiecksgitterstruktur beeinflußt der b-Gittervektor t', während der c-Gittervektor Auswirkungen auf t hat. Demzufolge hat das Verhältnis c/b einen Einfluß auf t'/t. Entsprechend zeigt das c/b ebenfalls ein Maximum bei etwa 150 K. Ein Grund für diese Anomalie könnten das Ordnen der Ethylengruppen sein. Aus der Datenanalyse kann man ablesen, dass die Anordnung der Ethylengruppen in gestaffelter Konfiguration schrittweise von Raumtemperatur (77%) bis 200 K (93%) zunimmt und bei unter 150 K vollständig ist. Tatsächlich steht dies gut im Einklang mit Beobachtungen aus ^{1}H-NMR-Messungen, wonach sich ein starker Beitrag von thermisch aktivierten Schwingungen der Ethylen-Gruppe ergibt, der

unterhalb von 150 K verschwindet. Die Temperaturabhängigkeit von t'/t könnte auch mit der scharfen Veränderung in der Thermokraft bei rund 150 K zusammenhängen, da es sich dabei um die Energieableitung der Zustandsdichte am Fermi-Niveau handelt.

Um die Leistungsfähigkeit der Apparatur zur Messung der 'thermischen Ausdehnung unter Heliumgasdruck' zu demonstrieren wurde zunächst Azurit $Cu_3(CO_3)_2(OH)_2$, welches eine Realisierung der eindimensionalen verzerrten Diamantkette darstellt bei sowohl Umgebungsdruck ($P \simeq 0$) als auch unter hydrostatischem Druck untersucht. Der uniaxiale thermische Ausdehnungskoeffizient (α) im Temperaturbereich von $T = 1{,}5$ K bis $T = 100$ K entlang der [010]-Richtung, also der b-Achse von Azurit unter Umgebungsdruck deckt sich mit bereits publizierten Daten. Zwei Drittel der im Material vorhandenen Cu^{2+} Spins bilden bei $T \approx 20$ K Spin-Singulett $S_{dimer} = 0$ Dimere. Die kurzreichweitige Ordnung der verbleibenden Cu^{2+} Monomer Spins tritt bei $T \approx 4$ K auf. Die antiferromagnetische intra-Dimer Austauschwechselwirkung $J_2/k_B \simeq 33$ K, welche mit der Bildung der Spin Singuletts $S_{dimer} = 0$ Dimere zusammenhängt, ist die im System vorherrschende Energieskala. Dahingegen ist die entsprechende antiferromagnetische Monomer-Monomer Austauschwechselwirkung $J_m/k_B \simeq 4{,}6$ K um eine Größenordung kleiner. Bei weiterem Abkühlen kommt es bei $T_N = 1{,}88$ K zu langreichweitiger antiferrormagnetscher Ordnung als Folge von schwacher dreidimensionaler magnetischer Wechselwirkung.

Die Experimente haben gezeigt, dass kleine, endliche Drücke (2,0 MPa, 6,2 MPa, 9,5 MPa) erstaunlich starke Auswirkungen auf den Tieftemperaturausdehungskoeffizienten von Azurit haben. Durch den höchsten angewendeten Druck von $P = 9{,}5$ MPa wird eine allgemeine Verringerung des Ausdehnungskoeffizienten offenbart, was von einer starken Unterdrückung des ausgeprägten Maximums in α_b bei ungefähr 20 K begleitet wird und zu einer Ausbildung einer Schulter unter Druck führt. Ebenfalls scheint sich die Anomalie in α_b unter hydrostatischem Druck zu tieferen Temperaturen zu verschieben. Dies wird durch den Grüneisen Formalismus vorhergesagt, da der Volumenausdehnungskoeffizient($\beta \simeq$ - 13×10^{-6} K^{-1}) im Bereich um die Anomalie ein negatives Vorzeichen besitzt. Aufgrund der Tatsache, dass in diesem Material verschiedene, miteinander konkurrierende Austauschwechselwirkungen eine wichtige Rolle spielen, wäre von Interesse zu untersuchen, wie sich diese Wechselwirkungen unter Einwirkung von Druck verändern. Die Messung der thermischen Ausdehnung bietet sich dazu als ein höchst empfindliches Werkzeug zur Identifikation und Erforschung der dominanten Wechselwirkungen an.

dedicated to my parents

Contents

1 Introduction **13**
1.1 Definition and thermodynamic relations 14
1.2 The Mott metal-insulator transition 17
1.3 Tight-binding model 18
1.4 Critical exponents and universality class 19
1.5 Quantum spin liquids 21
1.6 Distorted diamond-chain model 23
1.7 Outline of the thesis 24

2 Experimental section **27**
2.1 Thermal expansion at ambient-pressure 27
2.2 Thermal expansion under pressure 29
2.3 Electrochemical crystallization technique 38
2.4 Calculation of thermal expansion coefficient (α) 40
2.4.1 Cell effect calculation 40
2.5 Van der Waals equation of state 41
2.6 Calculation of the dielectric constant (ε_r) 43
2.6.1 Pressure-induced cell effect 45

3 Charge-transfer salts **47**
3.1 Quasi-one-dimensional salts 47
3.2 Quasi-two-dimensional salts : κ-$(ET)_2X$ 48
3.3 Ultrasonic measurements under helium gas pressure 51
3.4 Controversy on the Mott universality class 52

4 Organic 2D quantum spin-liquid – κ-$(BEDT\text{-}TTF)_2Cu_2(CN)_3$ **55**
4.1 Thermal expansion measurements 61
4.2 Entropy calculation from specific heat 64

4.3 Magnetic field dependency in κ-(BEDT-TTF)$_2$Cu$_2$(CN)$_3$ 69
4.3.1 Field-induced effect in thermal expansion 70
4.4 Temperature dependence of structural and electronic properties 77

5 Azurite – $Cu_3(CO_3)_2(OH)_2$ 83
5.1 Thermal expansion at ambient-pressure 88
5.2 Pressure effect on T_N 90
5.3 Thermal expansion under pressure 90
5.3.1 Experimental conditions and limitation 90
5.3.2 Experimental observation 91
5.3.3 Discussion 93

6 Summary 97

7 Outlook 101

Bibliography 103

List of Figures 113

List of Tables 115

Acknowledgements 117

Curriculum Vitae 121

1 Introduction

The physics of low-dimensional frustrated quantum magnets has attracted a lot of interest in recent years. Theoretically different properties of these frustrated quantum magnets have been claimed a while back, but this field has become more interesting with the evidence of many motivating experiments. Organic charge-transfer salts, namely, the two-dimensional κ-(BEDT-TTF)$_2$X, where BEDT-TTF (in abbreviation ET) refers to *bis(ethylenedithio)-tetrathiafulvalene* ($C_6S_8[(CH_2)_2]_2$) and X is the monovalent anion, are among the prime examples of frustrated quantum magnets. The κ-phase is the special variety of packing where two ET-molecules form a dimer. In the limit of strong dimerization a dimer-dimer interaction model can be constructed. Based on this model, nearest-neighbor hopping integrals t and t' and the on-site Coulomb repulsion U can be calculated thereby defining the degree of frustration and interaction strength, respectively. These materials are Mott insulators, but varieties of phases can be obtained either by changing the anions, which act as a chemical pressure, or by the application of hydrostatic pressure. As there is an interplay between spin, charge and lattice degrees of freedom, organic charge-transfer salts can be thought of as model systems. Moreover, the phase diagram of organics resembles that of the high-temperature cuprate superconductors, a further motivation for studying in order to have a better understanding of the effects of strong electronic correlations.

Of particular interest, when the anion X = Cu[N(CN)$_2$]Cl is replaced by Cu$_2$(CN)$_3$, is that the effect of frustration gets stronger. This frustration can be explained when the nearest-neighbor hopping integrals t and t' are comparable in their triangular-lattice arrangement. As no long-range order has been observed down to millikelvin temperatures, this confirms the spin-liquid state in this compound even though the exchange interaction is $J = 250$ K. In early 1970, Anderson proposed that the absence of long-range order and no spin rotational symmetry breaking in the Heisenberg spin $S = 1/2$ triangular-lattice are the signatures of a spin-liquid ground state. One of the major parts of the present thesis is to study this material by performing mainly thermal expansion measurements

as a function of temperature and magnetic field.

Thermal expansion is a powerful technique to investigate the lattice effects of a material and its coupling to other degrees of freedom such as charge and spin of the electrons. The heart of this setup, the dilatometer cell, which is used to study the material has a resolution of $\Delta l/l \sim 10^{-10}$ for a sample of length 10 mm. The effect of hydrostatic pressure on a material plays an important role in solid state physics as it can induce various phase transitions. Moreover, the pressure effect on organic charge-transfer salts is enormous, sometimes a few megapascals are enough to cross the phase boundary. As a matter of fact, the 'thermal expansion under pressure' is a unique instrument to study the pressure dependent lattice effects of materials.

The natural mineral azurite, $Cu_3(CO_3)_2(OH)_2$, has also attracted much interest in recent years. The effect of frustration plays also an important role in this compound. The spins are arranged in an antiferromagnetic fashion in a diamond-chain which causes frustration. Extensive theoretical studies have been performed to model this system and it has been proposed that azurite is a realization of quasi-one-dimensional distorted diamond-chain. The microscopic model which can explain the essential properties of azurite is the monomer-dimer model, *i.e.*, monomer spins $S = 1/2$ are separated by the $S_{dimer} = 0$ dimers on the diamond-chain backbone. There is a controversy of the exchange coupling constants in the triangular-lattice structure. Experimentally, double-peak structures have been observed by performing specific heat, magnetic susceptibility, ultrasound measurements at 20 K and 4 K. These anomalies signify the dimer $S_{dimer} = 0$ formation for $S = 1/2$ and the short-range ordering of monomer spins, respectively. Upon cooling further, three-dimensional antiferromagnetic long-range order happens at 1.88 K. This phase transition anomaly has a huge pressure effect, calculated from the thermodynamic Ehrenfest relation. Thermal expansion measurements have been carried out at ambient-pressure as well as finite pressure values for this compound.

Some definitions and models, which are relevant to this thesis, are discussed below. Finally at the end of this chapter, an outline of the whole thesis is described.

1.1 Definition and thermodynamic relations

The thermal expansion coefficient (α) is defined as

$$\alpha(T) = \left(\frac{\partial \ln l(T)}{\partial T}\right)_P \tag{1.1.1}$$

where l is the length of the sample and T is the temperature. In general, this coefficient α can be measured along the three crystallographic directions of a crystal, namely the a, b and c-axes. The volumetric thermal expansion coefficient (β) is nothing

but the sum of the thermal expansion coefficients along the three axes, provided they are orthogonal to each other. So one can write

$$\beta(T) = \alpha_a + \alpha_b + \alpha_c = \left(\frac{\partial \ln V(T)}{\partial T}\right)_P \tag{1.1.2}$$

The volumetric coefficient (β) is related to the Helmholtz free energy *F(V,T)* and the Gibbs free energy *G(P,T)* via thermodynamic relations. The relation between β and *F(V,T)* is as follows

$$\begin{aligned} \beta &= -\left(\frac{\partial \ln V}{\partial P}\right)_T \left(\frac{\partial P}{\partial T}\right)_V = \kappa_T \left(\frac{\partial P}{\partial T}\right)_V \\ &= -\kappa_T \left(\frac{\partial^2 F}{\partial V \partial T}\right) = \kappa_T \left(\frac{\partial S}{\partial V}\right)_T \end{aligned} \tag{1.1.3}$$

where κ_T is the isothermal compressibility and S is the entropy. β is related to the volume dependence of the entropy with a factor κ_T, the compressibility. So the temperature dependence of the thermal expansion depends mainly on the factor $(\partial S/\partial V)_T$, but the compressibility remains finite when the temperature tends to zero.

The relation between β and *G(P,T)* is as follows

$$\beta = \left(\frac{\partial \ln V}{\partial T}\right)_P = \frac{1}{V}\left(\frac{\partial^2 G}{\partial P \partial T}\right) = \frac{\left(\frac{\partial^2 G}{\partial P \partial T}\right)}{\left(\frac{\partial G}{\partial P}\right)_T} \tag{1.1.4}$$

Since the isothermal bulk modulus, B_T is reciprocal to κ_T, so Eq. (1.1.3) modifies to

$$\beta B_T = -\frac{\partial^2 F}{\partial V \partial T} \tag{1.1.5}$$

Now, the specific heat, at constant volume (C_V), is defined in terms of the Helmholtz free energy which is

$$C_V = -T\left(\frac{\partial^2 F}{\partial T^2}\right)_V \tag{1.1.6}$$

Due to the interaction between the electrons, magnetic spins or electric dipoles, thermodynamic transformations occur as a function of temperature which is nothing but a

change in entropy. The temperature where the transformation occurs, namely the transition temperature (T_c) is directly related to the change in volume expansion coefficient and specific heat via the Ehrenfest relation which is

$$\frac{1}{T_c}\frac{\mathrm{d}T_c}{\mathrm{d}P} = V_{mol}\frac{\Delta\beta}{\Delta C_P}, \tag{1.1.7}$$

where V_{mol} is the molar volume.

Thermodynamically, the thermal expansion and the specific heat are related via the Grüneisen relation. The change in entropy can be written in terms of the change in volume and the change in temperature which is

$$\begin{aligned} \mathrm{d}S &= \left(\frac{\partial S}{\partial T}\right)_V \mathrm{d}T + \left(\frac{\partial S}{\partial V}\right)_T \mathrm{d}V \\ &= C_V\frac{\mathrm{d}T}{T} + \beta B_T \mathrm{d}V \\ &= C_V \mathrm{dln}T + \beta B_T V \mathrm{dln}V \end{aligned} \tag{1.1.8}$$

For a constant value of entropy, Eq. (1.1.8) transforms to

$$\frac{\beta B_T V}{C_V} = -\left(\frac{\partial \mathrm{ln}T}{\partial \mathrm{ln}V}\right)_S \equiv \Gamma(T,V) \tag{1.1.9}$$

$\Gamma(T,V)$ is called the Grüneisen function [1] which has a relatively weak temperature dependence.

One can write the above equation in the following form

$$\Gamma(T,V) = \frac{(\partial S/\partial \mathrm{ln}V)_T}{C_V} \tag{1.1.10}$$

So the entropy (S) is one of the key factors to define the Grüneisen function (γ). It may have different contributions like lattice, electronic, spin, magnetic, etc., which can be expressed as

$$S = \sum_r S_r \tag{1.1.11}$$

The specific heat can be also be written as the sum of different contributions

$$C_V = \sum_r (\partial S_r/\partial \mathrm{ln}T)_V = \sum_r C_r \tag{1.1.12}$$

For each contribution the Grüneisen functions can be written in general

$$\Gamma_r = \frac{1}{C_r}\left(\frac{\partial S_r}{\partial \ln V}\right)_T \tag{1.1.13}$$

So the Γ can be written as an average of the Γ_r weighted by the respective heat capacities

$$\Gamma = \frac{\sum_r \Gamma_r C_r}{\sum_r C_r} \tag{1.1.14}$$

1.2 The Mott metal-insulator transition

The Mott metal-insulator transition is driven by electron-electron correlations. Experimentally, a large change in resistivity is associated with this transition in general. The ordering of spin, charge and lattice degrees of freedom play an important role near the transition point. Organic charge-transfer salts provide prime examples of Mott insulators [2], with the remarkable property that upon applying pressure, superconductivity can be achieved [3, 4]. The Mott transition is first-order in nature and is not associated with the spontaneous symmetry breaking [5, 6].

The theoretical model for addressing the metal-insulator transition is the well-known *Hubbard model*. This model in its simplest form considers only one electron in a single band and its Hamiltonian is given by

$$\mathcal{H}_H = \mathcal{H}_t + \mathcal{H}_U - \mu_N \tag{1.2.1}$$

$$\mathcal{H}_t = -t \sum_{<ij>} (c^\dagger_{i\sigma} c_{j\sigma} + H.c.) \tag{1.2.2}$$

$$\mathcal{H}_U = U \sum_i (n_{i\uparrow} - \frac{1}{2})(n_{i\downarrow} - \frac{1}{2}) \tag{1.2.3}$$

$$N \equiv \sum_{i\sigma} n_{i\sigma} \tag{1.2.4}$$

where $c^\dagger_{i\sigma}$ and $c_{i\sigma}$ are the creation and the annihilation operator of the single-band electron at site i with spin σ, respectively. $n \equiv c^\dagger_{i\sigma} c_{i\sigma}$ is the number operator, μ the chemical potential and U the on-site Coulomb repulsion [7]. In the case of the Mott transition, two terms t and U are very important. If the electrons have a sufficient amount of kinetic energy ($E_K \sim t$) to overcome the Coulomb energy U, then they are

allowed to move. But for $t \ll U$, *i.e.*, in the narrow band limit, the electrons do not have enough kinetic energy to delocalize. As a result, a gap opens in the single-particle excitation spectrum which leads to the Mott insulating behavior.

1.3 Tight-binding model

The tight-binding model is an approach in solid-state physics for calculating the electronic band structure. The electronic structure (in the case of a condensed matter system) refers to the electronic wave function and the description of the binding energy associated with it which keeps the atoms together. The basis function of this model are the atomic orbitals. One-electron Bloch functions can be written in the following form

$$\psi_{\mathbf{k}}(\boldsymbol{r}) = \frac{1}{\sqrt{N}} \sum_{R} \varphi_n(\boldsymbol{r} - \boldsymbol{R}) e^{i\mathbf{k}\cdot\mathbf{R}} \tag{1.3.1}$$

where $\boldsymbol{k}$ is the wave vector, φ_n an atomic wave function and n the orbital quantum number for a particular band index.

In an independent-electron approximation, the single electron time-independent Schrödinger equation has the following form

$$\mathcal{H}\psi_k(\boldsymbol{r}) = \epsilon_k \psi_k(\boldsymbol{r}) \tag{1.3.2}$$

where ϵ_k are the different eigenenergies corresponding to the eigenstates. The Hamiltonian operator is given as

$$\mathcal{H} = -\frac{1}{2}\nabla^2 + V(\boldsymbol{r}) \tag{1.3.3}$$

where $V(\boldsymbol{r})$ is the potential energy operator.

As there is an overlap between the π-molecular orbitals in the case of organic charge-transfer salts, tight-binding band-structure calculations can be employed to estimate the electronic states. The most well-known approximation is the extended-Hückel approximation, which determines the transfer integrals and the corresponding transfer energies t between the π-orbitals of adjacent molecules. The energy-dispersion relation for the extended-Hückel tight-binding bands is derived as follows

$$E(\boldsymbol{k}) = 2t_a cos(k_a a) + 2t_b cos(k_b b) + 2t_c cos(k_c c) \tag{1.3.4}$$

where a, b, and c are the intermolecular distances for the corresponding a-, b- and c- axes, t the corresponding transfer energies. The transfer energies depend on the molecular arrangement. The different transfer energies in the case of two-dimensional κ

type-arrangements of BEDT-TTF molecules are discussed in chapter 4 (see Fig. 4.0.5).

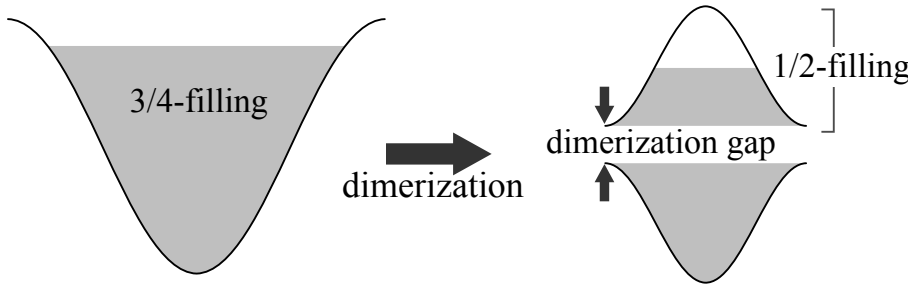

Figure 1.3.1: Schematic diagram of the conduction band in the case of a three-quarter filling and half filling due to strong dimerization (adapted from ref. [8]).

The degree of band filling is also an important parameter in the organic charge-transfer salts and this is completely determined by the stoichiometry between the donor and acceptor molecules. In most cases, this ratio is 2:1 which states that two donor molecules transfer one electron to the acceptor. As a matter of fact, the conduction band is three-quarter-filled. But in the case of strong dimerization of the donor molecules, *e.g.*, BEDT-TTF, the conduction band splits into two parts giving rise to a gap in between. As a result, the conduction band becomes effectively half-filled. A schematic diagram of the conduction band in the case of a three-quarter filling and half filling due to strong dimerization is shown in Fig. 1.3.1 [8].

1.4 Critical exponents and universality class

A phase transition occurs when the state or phase of a matter changes from one state to another state by means of a thermodynamic transformation. The temperature at which this thermodynamic transformation happens is known as phase transition temperature or critical temperature (T_c). A normalized parameter which describes the degree of order of a system is known as an order parameter. For a totally disordered system, the value of the order parameter is 0 and in the case of a complete order it is 1. For example, the order parameter for a paramagnet-ferromagnet transition is the spontaneous magnetization, whereas for a liquid-gas transition, it is the density. The paramagnet-ferromagnet transition is a continuous phase transition with spontaneous symmetry breaking and the liquid-gas transition is a first-order phase transition where the symmetry between the two phases is the same.

In the vicinity of a continuous phase transition, *i.e.*, a second-order phase transition, thermodynamic quantities like specific heat, spontaneous magnetization, magnetic susceptibility and correlation functions behave as power laws which are independent of microscopic parameters of the system. The power laws are characterized by the universal

Exponent	Ising_2	Ising_3	XY_3	Heisenberg_3
α	0(log)	0.110(1)	-0.015	-0.10
β	1/8	0.3265(3)	0.35	0.36
γ	7/4	1.2372(5)	1.32	1.39
δ	15	4.789(2)	4.78	5.11

Table 1.1: The values of the critical exponents (α, β, γ and δ) of Ising, XY and Heisenberg universality classes (adapted from ref. [9]). Index indicates the dimensionality.

exponents for $T \to T_c$, the so called critical exponents. The exponents for different microscopic constituents can have the same values. For that reason, these exponents values are universal. In the following, critical exponents are defined as a power of reduced temperature t

$$t = \frac{T - T_c}{T_c}. \tag{1.4.1}$$

The exponents which can be measured experimentally are α (from specific heat *C(t)*), β (from spontaneous magnetization *m(t)*), γ (from magnetic susceptibility χ*(t)*) and δ (from critical isotherm *m(h)*). The critical isotherm gives the magnetic field (h) dependence of the magnetization at $T = T_c$.

$$C(t) \propto |t|^{-\alpha} \tag{1.4.2}$$

$$m(t) \propto (-t)^{\beta}, t \leq 0 \tag{1.4.3}$$

$$\chi(t) \propto |t|^{-\gamma} \tag{1.4.4}$$

$$m(h) \propto |h|^{1/\delta} sgn(h), t = 0 \tag{1.4.5}$$

In Table 1.1 the values of the critical exponents are shown for Ising, XY and Heisenberg universality classes. The subscripts of the header line signify the dimensionality. The exponents of the two-dimensional Ising universality class are exact, in contrast to the three-dimensional case which is approximate [9].

The critical exponents are related via scaling relation by the following equations

$$2 - \alpha = 2\beta + \gamma \tag{1.4.6}$$

$$2 - \alpha = \beta(\delta + 1) \tag{1.4.7}$$

Limelette *et al.* determined the critical exponents near the Mott insulator to metal

critical endpoint for the *Cr*-doped V_2O_3 system by performing conductivity experiments as a function of temperature and pressure. The values of the critical exponents are ($\delta = 3$, $\gamma = 1$, $\beta = 0.5$). From these values they concluded that the exponents show some indication of the three-dimensional Ising universality class [10]. Organic charge-transfer salts, namely, the two-dimensional κ-(BEDT-TTF)$_2$X are also studied in the literature to explore their Mott criticality. κ-(BEDT-TTF)$_2$Cu[N(CN)$_2$]Cl shows an insulator to metal transition by applying only $\sim$ 30 MPa pressure, which is first-order in nature, and a first-order *s*-shaped transition line is formed as a function of pressure, which ends at a second-order critical end point where the criticality has been studied. Kagawa *et al.* studied this system by employing thermal conductivity measurements as a function of temperature and pressure, and calculated the critical exponent values near to the second-order critical end point. The critical exponents values obtained are ($\delta = 2$, $\gamma = 1$, $\beta = 1$). From these values they concluded that the Mott transition in the present two-dimensional system is not consistent with any of the known universality classes [11]. Very recently, they again confirmed the critical exponent value ($\delta = 2$) by performing ^{13}C-NMR experiments under pressure [12].

Thermal expansion measurements have been performed on the κ-(d8-ET)$_2$Cu[N(CN)$_2$]Br compound [2]. A large anomaly was found at $T_0 \simeq 32$ K, which was attributed to the second-order critical end point. The value of the specific heat critical exponent ($\alpha \simeq 0.8 \pm 0.15$) was calculated by employing a Grüneisen-scaling Ansatz [2]. This unusual and large critical exponent value was considered to indicate an important role of the lattice degrees of freedom [2]. However, a more recent work based on the scaling theory for the finite-temperature critical end point suggests the breakdown of Grüneisen-scaling upon approaching the critical end point ($T_0 \simeq 32$ K and $P_0 \simeq 22$ MPa) followed by a sign change in the thermal expansion coefficient. According to the scaling analysis, the expansivity data are consistent with the two-dimensional Ising universality class (critical exponent $\beta = 1/8$) [13]. A reexamination of the conductivity data [11], revealed that under certain conditions - a dominant coupling of the conductivity to the energy density - the data are consistent with the two-dimensional Ising universality class [14]. Consequently, a good check would be to perform the thermal expansion under pressure measurements. These will be discussed in the next chapter in detail.

1.5 Quantum spin liquids

A quantum spin-liquid (*QSL*) is defined as quantum mechanical ground state in which there is no long-range magnetic order (*LRMO*) and no breaking of spatial (rotational or translation) symmetries even at $T = 0$ K. A quantum spin-liquid state is different compared to disorder due to classical fluctuations which is mainly driven by the thermal energy. A valance bond state (*VBS*) is a non-magnetic state where the nature of interaction is antiferromagnetic and spins form a spin-0 singlet state. As the arrangement

of the valence bonds is not unique in a *VBS* state, it typically breaks lattice symmetries and lacks long-range entanglement. When the quantum fluctuations are included in the case of valence bonds, a quantum spin-liquid ground state is built and this ground state will be of a superposition of different partitionings of spins into valence bonds. Resonating valence bonds (*RVB*) [15] will be formed when the distribution of these partitionings is broad which leads to no preference for any specific valence bond [16]. In this respect, κ-(BEDT-TTF)$_2$Cu$_2$(CN)$_3$ [17], EtMe$_3$Sb[Pd(dmit)$_2$]$_2$ [18] are proposed to be good candidates for having a quantum spin-liquid ground state. Cs$_2$CuCl$_4$ is a quasi-two-dimensional spin-1/2 triangular lattice frustrated Heisenberg antiferromagnet where also a spin-liquid phase is realized in a small part of the B-T phase diagram. The spin-liquid phase ($T_N < T < T_{max}$) is characterized by strong intralayer antiferromagnetic correlations, where T_N (0.6 K) is the Néel temperature and T_{max} (2.65 K) is the maximum of the magnetic susceptibility [19]. Very recently, one more compound, Ba$_3$CuSb$_2$O$_9$ was found, which shows also indications for a quantum spin-liquid ground state with an $S = 1/2$ triangular-lattice [20]. The spin-liquid phase of the multiple-spin exchange model on a triangular lattice can be studied by employing an exact diagonalization method. This particular spin-liquid phase is characterized by the lack of Néel long-range order, short-ranged magnetic correlations, and a spin gap [21].

There are a couple of ways to classify the different categories of spin liquids. Depending on the excitation spectrum, there are three different kinds of spin liquids which are stated below.

1. $\Delta_S \neq 0$ and $\Delta_T \neq 0$
2. $\Delta_S = 0$ and $\Delta_T \neq 0$
3. $\Delta_S = \Delta_T = 0$,

where Δ_T is the energy gap between the singlet ground state and the lowest-lying triplet state, and Δ_S is the gap to the first excited singlet state [22].

There are a couple of proposals which describe the low-lying excitations involved in the spin-liquid ground state [23, 24]. The low-lying excitations in the case of a one-dimensional antiferromagnetic spin chain, which has a spin-liquid ground state, are gapless spinons. The spinon carries only spin but no charge, and it contributes to the specific heat and thermal conductivity even in the insulating state [23]. Spinons have total spin-1/2 and obey "semion" statistics which are intermediate between fermion and boson statistics, *i.e.*, there is a phase factor $\pi/2$ associated with particle exchange [25]. So according to the statistics of quasi-particles, spin liquids are classified into four classes [22].

• **Rigid spin-liquid:** spinons (and all other excitations) are fully gapped and may have either bosonic, fermionic, or fractional statistics.
• **Fermi spin-liquid:** spinons are gapless and are described by a Fermi-liquid theory

(the spinon-spinon interactions vanish as the Fermi energy is approached).
• **Algebraic spin-liquid:** spinons are gapless, but they are not described by free fermionic and free bosonic quasi-particles.
• **Bose spin-liquid:** low-lying gapless excitations are described by a free-boson theory.

An empirical measure of frustration has been proposed and widely used [26]. At high-temperature, the spin susceptibility of a local-moment magnet is given by Curie-Weiss formula

$$\chi = \frac{C}{T - \theta_{CW}}, \tag{1.5.1}$$

where T is the temperature, C is the Curie constant and θ_{CW} is the Curie-Weiss temperature. The strength of the magnetic interaction can be estimated by plotting $1/\chi$ vs T. If $\theta_{CW} < 0$, then it would be an antiferromagnet. The frustration parameter (f) is defined by: $f = |\theta_{CW}|/T_c$, where T_c is the temperature where order freezes. A system can be called a frustrated system if $f >$ 5-10 and the temperature range $T_c < T < |\theta_{CW}|$ defines the spin-liquid regime [16].

1.6 Distorted diamond-chain model

The distorted diamond-chain model is a theoretical model which describes the physics of a certain class of low-dimensional quantum spin systems in terms of their exchange coupling constant. The Hamiltonian which can describe the model is as follows

$$\mathcal{H} = \mathcal{H}_0 + \mathcal{H}_z, \tag{1.6.1}$$

where

$$\mathcal{H}_0 = J_1 \sum_{j=1}^{N/3} (\mathbf{S}_{3j-1} \cdot \mathbf{S}_{3j} + \mathbf{S}_{3j} \cdot \mathbf{S}_{3j+1}) + J_2 \sum_{j=1}^{N/3} \mathbf{S}_{3j+1} \cdot \mathbf{S}_{3j+2} + J_3 \sum_{j=1}^{N/3} (\mathbf{S}_{3j-2} \cdot \mathbf{S}_{3j} + \mathbf{S}_{3j} \cdot \mathbf{S}_{3j+2}) \tag{1.6.2}$$

$$\mathcal{H}_z = -H \sum_{l=1}^{N} S_l^z. \tag{1.6.3}$$

Here $\boldsymbol{S}_l$ is the spin operator with $S = 1/2$ and N is the total number of spins in the system. J_1, J_2 and J_3 are the coupling constants which are positive in the case of antiferromagnetism. H denotes the applied magnetic field.

Fig. 1.6.1 shows the schematic representation of the distorted diamond-chain model. The open circles stand for the $S = 1/2$ spins, full lines denote the exchange coupling

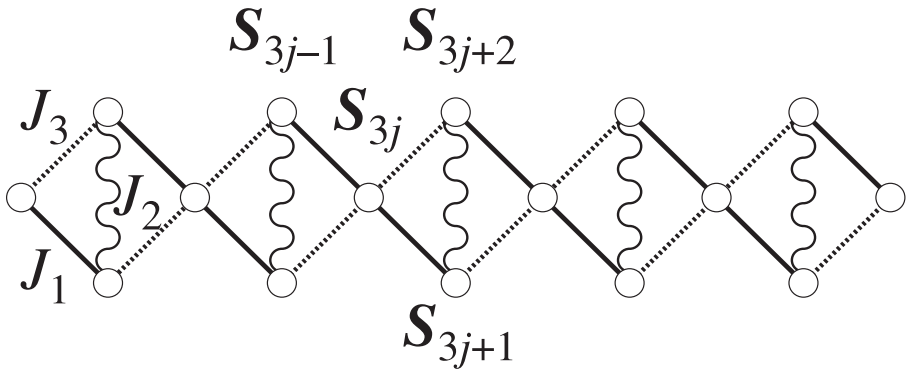

Figure 1.6.1: Schematic diagram of the distorted diamond-chain model with exchange couplings constants J_1, J_2 and J_3. The open circles stand for the $S = 1/2$ spins [27].

constant J_1, wavy lines J_2 and dotted lines J_3. It is known as a distorted diamond-chain model due to the fact that $J_1 \neq J_3$ in general [27, 28]. The experimental realization of the one-dimensional distorted diamond-chain model has been found in the compound azurite, $Cu_3(CO_3)_2(OH)_2$ which will be discussed in detail in chapter 5. A magnetization plateau is observed in this compound at 1/3 of the saturation magnetization (M_s). This phenomenon can also be explained by the diamond-chain model [29]. By interchanging the role of J_1 and J_3, $J_1 < J_3$ and $J_1 > J_3$ are equivalent. Because of this, one can assume that $J_1 \geqslant J_3$ without loss of generality. It is possible to have also $J_1 = J_3$ which is symmetric, called the diamond-chain model [30].

1.7 Outline of the thesis

This thesis is mainly dedicated to explore frustrated quantum magnets by means of thermal expansion measurements. The outline of the thesis is as follows:

Chapter 2 explains the experimental techniques which are used in this thesis. At the beginning, thermal expansion measurements at ambient pressure are described followed by a brief description of the sample loading. However, the new apparatus, the 'thermal expansion under pressure' is discussed in detail. The design of the gas-pressure cell, the special designing of the cryostat-insert, and the means taken to ensure constant-pressure condition are explained elaborately. The procedure of the data analysis, *viz.*, the cell effect calculation under pressure, the variation of the dielectric constant as a function of pressure and temperature are discussed.

Chapter 3 describes the properties of organic charge-transfer salts and why they are so interesting to study. Structural aspects as well as their chemical and physical pressure effects are also explained. Varieties of phases leading to a rich phase diagram in one- and two-dimension are also focused on in this chapter.

Chapter 4 focuses explicitly on the organic spin-liquid material κ-$(ET)_2Cu_2(CN)_3$. Initially, the motivation will be discussed why this material has attracted such as interest in recent years. Thermal expansion measurements have been performed in order to study the lattice effects along the three different crystallographic axes. A pronounced and strongly anisotropic anomaly at 6 K, a clear signature of a second-order phase transition and the entropy release at the phase transition are discussed in detail. The field-induced length changes along the particular crystallographic b-axis are also described. This chapter finishes with the studies based on the structural and electronic properties as a function of temperature which effect the degree of frustration and interaction strength.

Chapter 5 discusses the thermal expansion studies on azurite, $Cu_3(CO_3)_2(OH)_2$ which is the experimental realization of the quasi-one-dimensional distorted diamond-chain. Ambient-pressure as well as finite hydrostatic pressure measurements have been performed to demonstrate the functionality of the new instrument 'thermal expansion under pressure'. Hydrostatic pressure effects on azurite and also on helium, used as a pressure-transmitting medium, are also elaborated.

Chapter 6 summarizes all the work that has been performed within the frame of this thesis with some concluding remarks.

Chapter 7 explicates the future studies which can be done based on the achievements made in this thesis. In fact, many open questions have appeared which can be studied further.

2

Experimental section

Thermal expansion measurements provide a sensitive tool for exploring a material's thermodynamic properties. When such an experiment is performed, electronic, magnetic and lattice properties of the material can be studied. As was discussed in the previous chapter, the expansivity is related thermodynamically to the specific heat of a material via the following relation, $\beta = \Gamma \cdot \kappa_T \cdot V_m^{-1} \cdot C_V$, where β is the volume expansion coefficient, $\Gamma = C_V^{-1} \cdot (\partial S / \partial \ln V)_T$ the Grüneisen function measuring the volume (V) dependence of the system's entropy S, κ_T = -$(\partial \ln V / \partial P)_T$ the isothermal compressibility, V_m the molar volume, and C_V the specific heat at constant volume. This Grüneisen formalism can be applied to obtain the volume dependence of the characteristic energies (ϵ) of a material as Γ = -dlnϵ/dln$V$. The pressure dependence of the transition temperature (T_c) in the case of a second-order phase transition can be obtained from the Ehrenfest relation provided the contribution of the volume expansion coefficient (β) and the specific heat (C_P) across the transition is known. Particularly strong effects in the expansivity are expected in cases where the Grüneisen parameter (Γ) is large or even diverges. The latter situation is encountered upon approaching a quantum phase transition [31] or a finite-temperature critical end point [13], by, *e.g.*, the application of hydrostatic pressure.

In this chapter, the instrumentation of both thermal expansion measurements at ambient-pressure and under hydrostatic pressure conditions will be discussed.

2.1 Thermal expansion at ambient-pressure

The thermal expansion can be measured by different techniques, but the capacitive technique is the most sensitive method to measure the thermal expansion of solids. Fig. 2.2.3 shows the detailed construction of the high-resolution capacitive dilatometer which is used to perform thermal expansion measurements, built after [32]. Because of its high-resolution, even tiny anomalies in the expansivity can be detected by performing this

experiment.

The dilatometer cell which has been used to measure the thermal expansion at ambient-pressure has a sensitivity of $\Delta l/l \sim 10^{-10}$ for a sample of length 10 mm. This cell is made of high-purity (99.999%) copper (Cu). The capacitance value of the cell without sample is 16.7 pF and it has a maximum capacitance of $\sim$ 500 pF. Length changes as a function of temperature can be measured from $T = 1.3$ K to $T = 200$ K. The data $T >$ 200 K are not reliable anymore due to the contribution of copper oxide contaminations, formed over a period of several years, showing some anomalies.

A liquid-^4He glass cryostat with a superconducting magnet is used to perform the measurements as a function of temperature (T) and magnetic field (B). At lower temperature, preferably below $T \lesssim 45$ K, the temperature can be controlled via a temperature controller (TS 530) with suitable P, I & D values. In order to study the anomalies, *e.g.*, phase transitions, etc., a very small sweep rate of $\pm$ 1.5 K/hour is used in general. Magnetic fields up to $B = 10$ T can be applied by a superconducting solenoid connected to a magnetic power supply, Oxford Instruments (PS 120^3). Magnetostriction measurements, *i.e.*, length changes as a function of applied magnetic field while the temperature is kept constant, can also be performed with the magnetic field being ramped up and down.

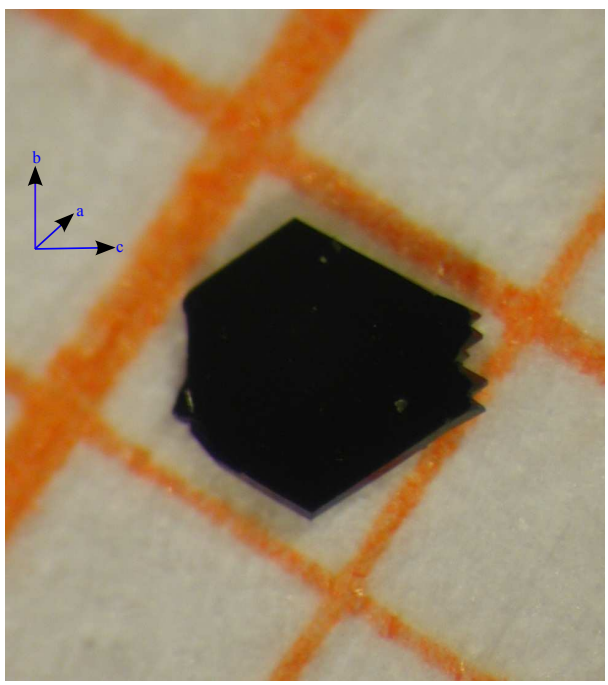

Figure 2.1.1: Typical single crystal of organic conductors. This is a picture of the spin-liquid compound κ-(BEDT-TTF)$_2$Cu$_2$(CN)$_3$ which is measured along the b-axis of length 0.8 mm. Inset: different crystallographic axes (in-plane b and c axes, out-of plane a axis) are shown.

Fig. 2.1.1 shows the size and shape of a typical two-dimensional organic charge-

transfer salt of κ-(BEDT-TTF)$_2$X. This is a picture of the spin-liquid compound where X = Cu$_2$(CN)$_3$. The inset shows the crystallographic axes. In order to measure the directional dependence of a very small, thin, fragile single crystal [33], gallium (Ga) spheres are used whose thermal expansion are negligible. In other words, the Ga-spheres act as a sample holder which is shown in Fig. 2.1.2. The cell effect which has to be deducted from the raw data is discussed in the next section in detail.

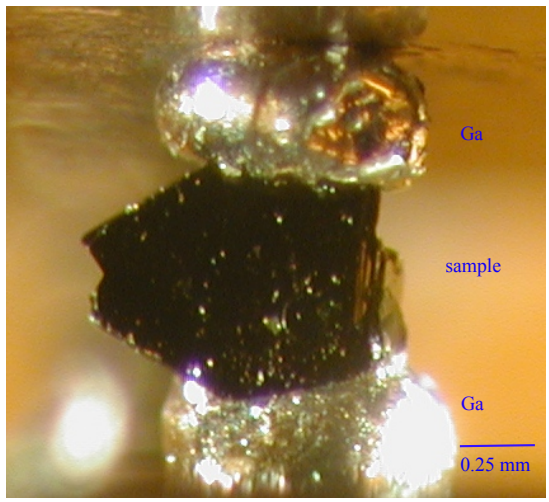

Figure 2.1.2: Picture of the sample after mounting inside the dilatometer cell. Here gallium (Ga) spheres are used as a sample holder in order to measure the directional dependance of such tiny and fragile single crystals. The spin-liquid compound κ-(BEDT-TTF)$_2$Cu$_2$(CN)$_3$ is mounted for measurements along the b-axis.

Temperature-dependent resistances, *i.e.*, thermometers are connected via the four-probe method. A calibrated platinum (Pt) thermometer is used to measure at higher temperature $T \gtrsim 25$ K and a calibrated germanium (Ge) thermometer is used to measure at lower temperature $T \lesssim 25$ K. Two more calibrated thermometers (Pt and Ge) are placed in the compensated zone of the magnet to avoid the effect of the magnetic field on the sensor and used to measure the temperatures when the magnetic field is applied. ^{3}He exchange gas is used to provide the thermal coupling between the ^4He-bath and the sample via the inner and outer chambers.

2.2 Thermal expansion under pressure

Thermal expansion under pressure [34] is a powerful technique to explore the thermodynamic properties of the materials, the properties of which depend on pressure. This area will be focused upon the designing of the thermal expansion setup containing a pressure

cell. Fig. 2.2.1 shows the overview of the high-pressure helium gas cell (HGC cell) [35]. The pressure cell is made of *CuBe* with a volume 81.4 cm^3. It has an inner and outer diameter of 36 mm and 56 mm, respectively, and an inner length of 80 mm. The weight of the pressure cell is 2.9 kg. Such a big pressure cell is needed to place the dilatometer cell of volume $\sim$ 20 cm^3. The maximum allowable pressure is 250 MPa within the temperature region of $T = 1.4$ K to $T = 293$ K. The plug has to be removed from the lower side of the pressure cell each and every time in order to change the sample. The plug contains mainly the dilatometer cell, a pressure gauge, electrical feed-throughs with cables for connecting the pressure gauge and the capacitor. A metal seal, made of brass coated with tin with a diameter 35.5 mm is needed to close the pressure cell and to make it pressure tight. A 60 Nm torque is needed in order to screw the retaining screw so that the seal is crushed properly between the plug and the pressure cell. Helium gas (^4He) is used as a pressure-transmitting medium. As a pressure reservoir a helium gas bottle or a helium gas compressor (Unipress Gas Compressor U11), is used as a pressure source for $P \leq 18$ MPa and $P > 18$ MPa, respectively. The pressure cell is connected by a *CuBe* capillary with an inner and outer diameter 0.3 mm and 3 mm, respectively, and a length of $\sim$ 10 m to the external pressure reservoir.

An *L*-piece, shown in Fig. 2.2.2, is placed on the mounting plates with legs inside the pressure cell and the dilatometer cell attested to this *L*-piece.

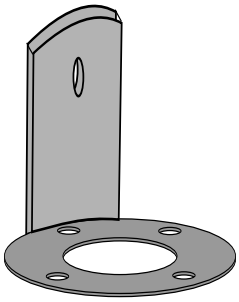

Figure 2.2.2: The dilatometer cell is placed inside the pressure cell via an *L*-piece made of *CuBe*.

The dilatometer which is used to perform thermal expansion measurements under pressure is relatively smaller and less sensitive (5×10^{-2} Å) compared to the dilatometer cell which is used in thermal expansion at ambient-pressure. This cell is made of pure silver (99.999%) with gold coating, but the capacitor plates are without coating. The design of this dilatometer cell is similar to the cell, cf. Fig. 2.2.3. The resolution of the present dilatometer is less due to the smaller size of the capacitor plates compared to the other ones. The capacitance value of the cell without sample is 5.8 pF and it has a maximum capacitance of $\sim$ 60 pF.

A Lakeshore temperature controller (LS 340) is used for the temperature stabilization and regulation. For this purpose, suitable P, I & D values are found out for different temperature ranges up to room temperature by using the standard procedure [36]. There are two heaters, namely, one is attested around the pressure cell and another one is attested around the inner copper can. A special kind of heater foils (*MINCO*, France) are used as heaters. All the experiments are performed by using the heater which is attested around the inner copper can for better efficiency. Heater foils are wrapped around the inner copper can and the pressure cell by putting a small amount of silicone grease in between

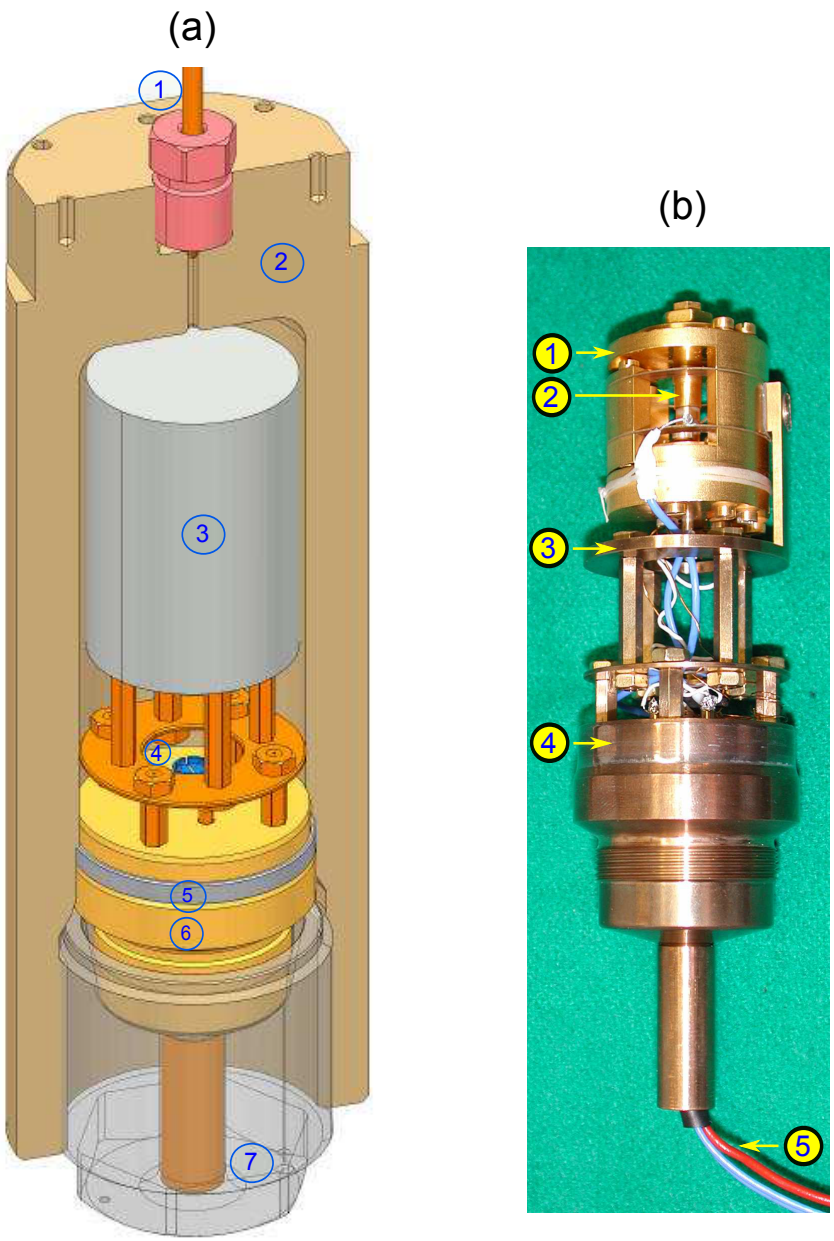

Figure 2.2.1: (a) Overview of the pressure cell (made of *CuBe*) of maximum allowable pressure 250 MPa: 1 capillary, 2 cell body, 3 dilatometer cell, 4 heavily doped *n-InSb* pressure sensor, 5 seal, 6 plug with electrical feed-throughs, 7 retaining screw [35]. (b) Detailed view of the plug of the pressure cell with the dilatometer cell: 1 dilatometer cell, 2 sample, 3 *L*-piece, 4 place where metal seal sits, 5 cables from the dilatometer cell and pressure gauge. The pressure cell is a joint development between University of Frankfurt, Frankfurt and Unipress, an Institute of High-Pressure Physics, Warsaw.

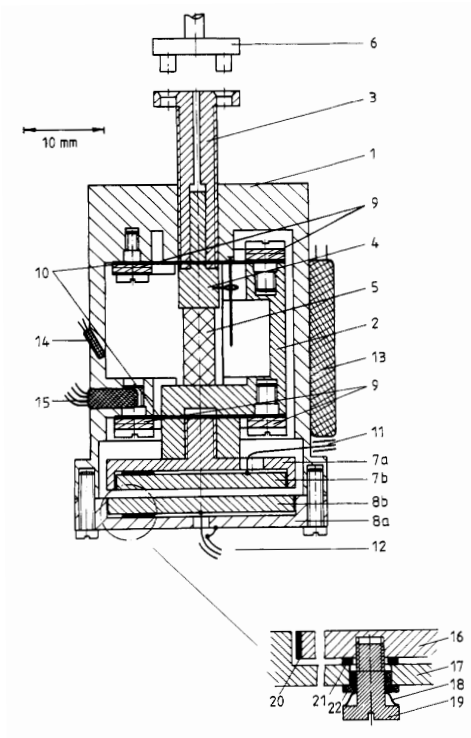

Figure 2.2.3: Construction of the dilatometer cell (adapted from ref. [32]): 1 frame, 2 movable part, 3 screw, 4 piston, 5 sample, 6 bayonet fitting (not used anymore), 7a guard ring, 7b capacitor plate, 8a guard ring, 8b capacitor plate, 9 washers, 10 springs, 11-12 electrical leads, 13 platinum resistor, 14 silicon diode, 15 germanium resistor. Inset: 16 capacitor plate, 17 guard ring, 18 spring, 19 screw, 20 kapton foil, 21 sapphire spacer, 22 kapton foil washer.

and finally to make those foils fixed kapton tapes are used. In order to get precise capacitance measurements, a high-precision Andeen-Hagerling capacitance bridge (AH 2550A) is used. Cernox resistors (model: CX-1080-CU, CX-1050-CU) are used as temperature sensor and these are placed on the top of the pressure cell. While the sensor CX-1080-CU is a high-temperature sensitive (20 K to 325 K) thermometer, the CX-1050-CU is the low-temperature sensitive (1.4 K to 325 K) thermometer. Thermometers are connected via the four-probe method. ^4He-exchange gas is used to provide the thermal coupling between the ^4He-bath and the sample via the inner and outer chambers.

The lower part of the specially designed home-made insert is concentric, *i.e.*, the pressure cell is isolated from the ^4He-bath via the inner and outer chambers. Fig. 2.2.4 shows the overall design of the insert whereas in Fig. 2.2.5 the detailed construction of the lower part of the insert with all specifications is shown on expanded scales. In order to have the thermal coupling to the bath, ^4He-exchange gas is used in the outer and inner chambers. The outer chamber acts as an isolation from the inner chamber and the He-bath with a suitable amount of exchange gas, one of the main advantages of this concentric construction. Heater foils are attested on the outer surface of the inner

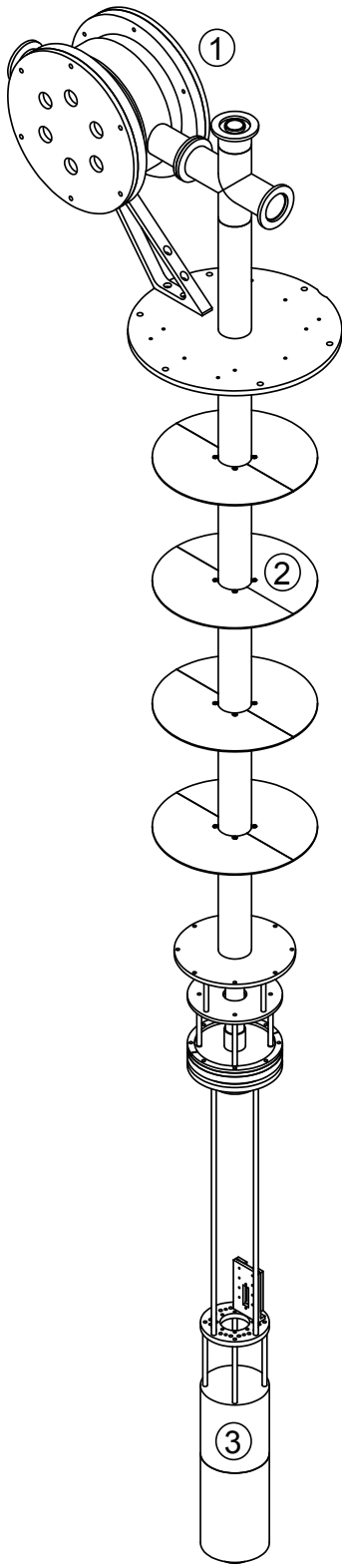

Figure 2.2.4: Complete overview of the cryostat insert: 1 distribution box for wires, 2 heat shields, 3 pressure cell.

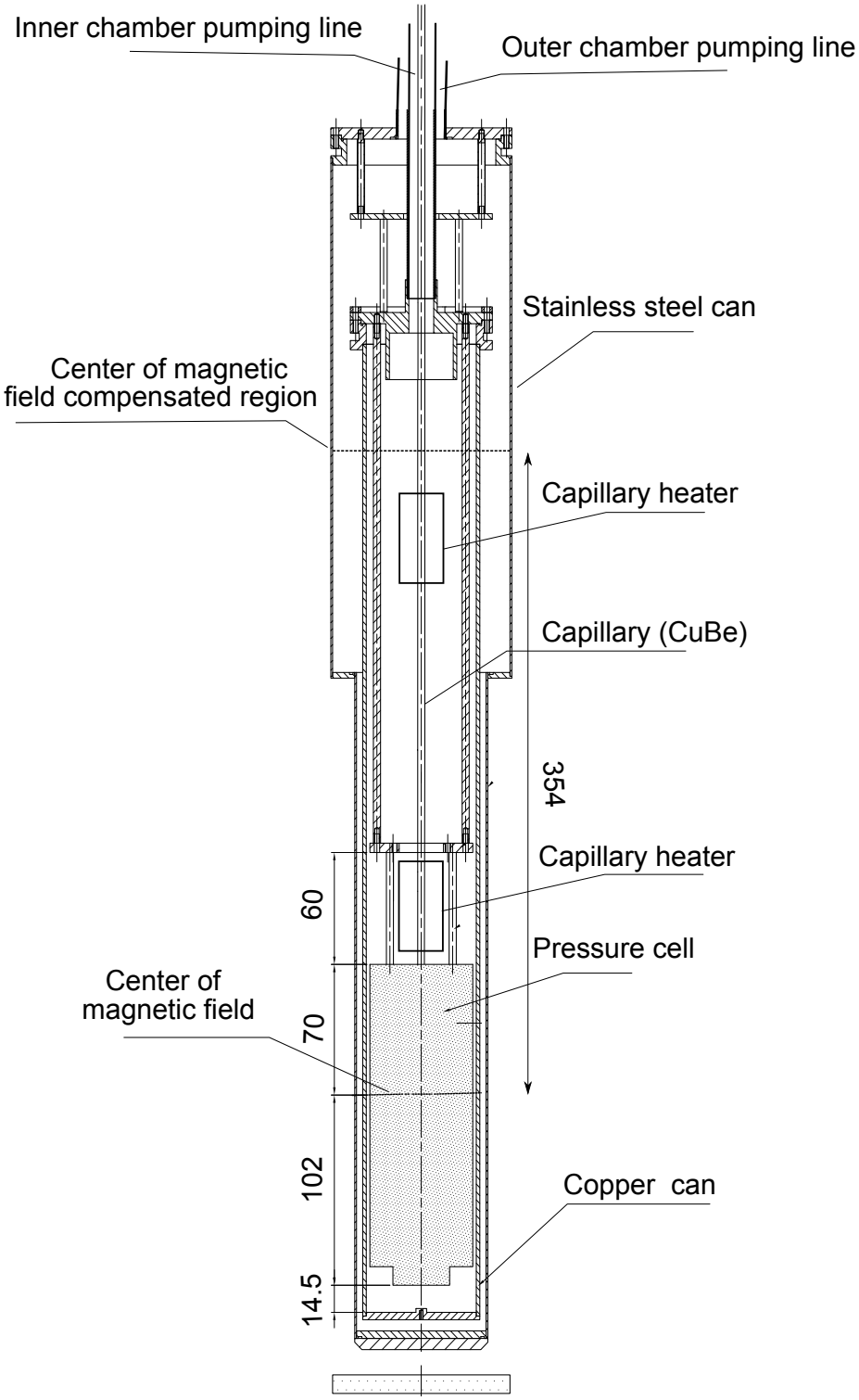

Figure 2.2.5: Concentric construction of the lower part of the specially designed home-made insert on expanded scales.

can and the pressure cell in order to have a uniform temperature regulation. The inner can is made of copper whereas the outer is made of stainless steel. The lower part of the insert is shown in Fig. 2.2.6 before and after putting the inner copper can. The concentric construction of the insert helps to control the exchange gas separately in the inner and outer chambers. The typical amount of ^4He exchange gas in the inner can is $\sim$ 0.02 MPa at room temperature which is kept constant throughout the whole accessible temperature range. This amount of exchange gas is enough to provide a good thermal contact between all parts within the can. But the amount of exchange gas in the outer chamber is $\sim$ 0.005 MPa at room temperature which can be varied, depending on the temperature range.

Capillary heaters are installed around the lower part of the capillary where it is connected to the pressure cell in order to overcome the blockage in the capillary. Sometimes, the capillary is blocked when the pressure medium, helium is not so pure. The capillary heaters can be seen in Fig. 2.2.6. Two 3 Ω resistances with a maximum power of 10 Watt are placed on the two rectangle copper blocks, respectively and connected in series. The copper blocks are then fixed around the lower part of the capillary where the blockage might happen. In order to read out how the temperature changes after switching on the capillary heater, one more Cernox (model: CX-1080-CU) resistor, which is a high-temperature sensitive (20 K to 325 K) thermometer, is placed on the upper copper block. The temperature of the capillary, where the capillary heaters are installed, is kept about 10 K above the temperature of the pressure cell in order to avoid the blockage while cooling.

An Oxford Instruments (IPS$^{120-10}$) magnetic power supply is used for magnetic field measurements and a specially-designed ^4He-gas compressor (Unipress Gas Compressor U11) of maximum allowable pressure, $P = 600$ MPa is used as a reservoir for pressure measurements.

With this setup, a magnetic field can be applied up to maximum of 12 T at 4.2 K, and 14 T at 2.2 K. In order to avoid the effect of the field on the sensor while applying magnetic field, there is a magnetic field compensated zone ($B < 0.01$ T) where the temperature sensors can be placed. The center of the compensated zone is 354 mm above the center of the main magnetic field region.

In order to carry out constant-pressure measurements, the volume of the pressure cell has to be very small compared to the pressure reservoir. In the present case, a very pure (5N) helium gas (^4He) in a gas bottle is used which is connected via a ^4He-gas compressor. In this configuration, using a passive, *i.e.*, a non-controllable compressor, the maximum pressure is limited to $P \leq 18$ MPa, the highest pressure allowed for the gas bottle of volume 50,000 cm^3. The valve connecting the pressure cell with the reservoir should be opened at all times during the measurement in order to allow the system to compensate for pressure changes due to temperature sweeps thereby fulfilling constant-pressure con-

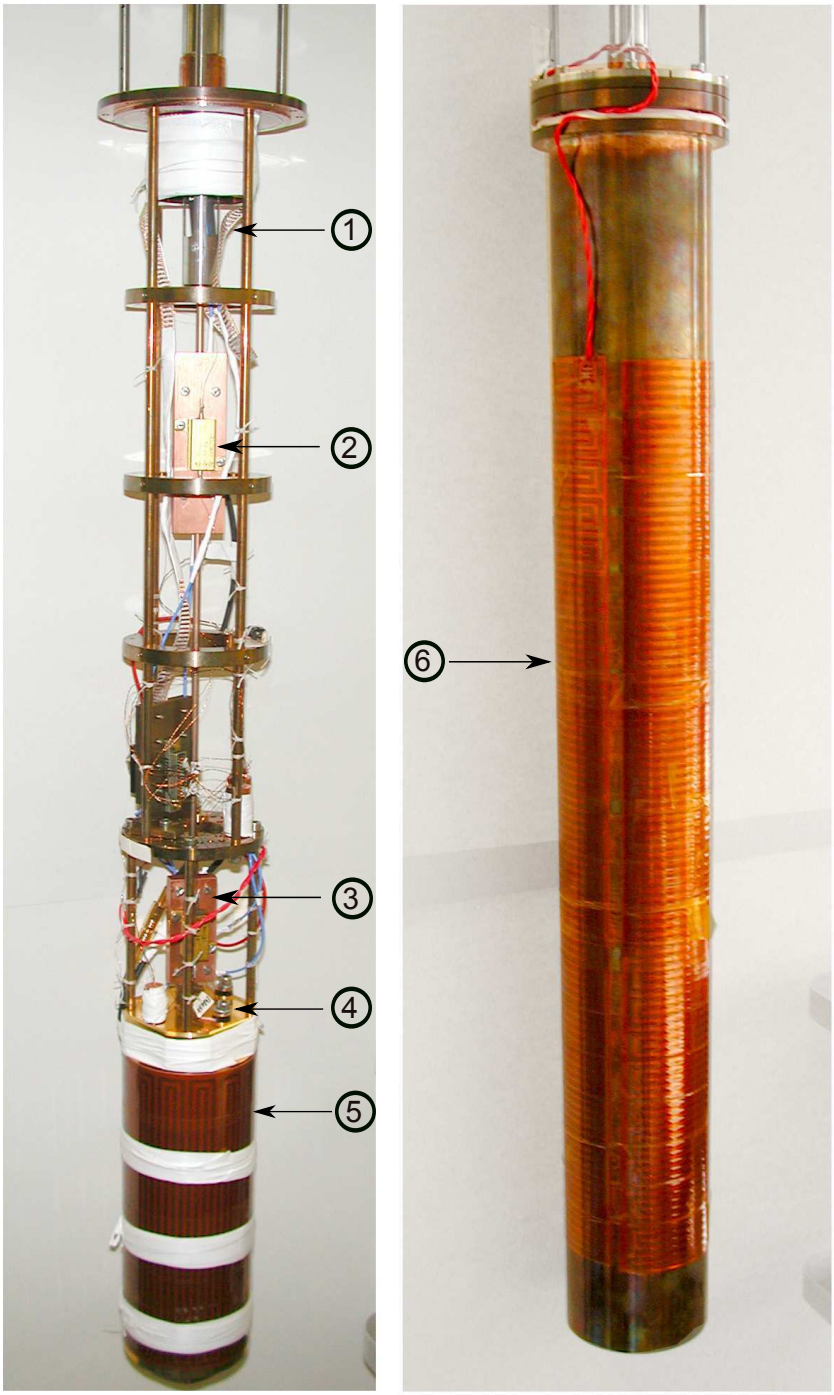

Figure 2.2.6: Detailed construction of the lower section of the insert before and after insertion of the inner copper can: 1 special loom with 12-pairs of 100 μm *Cu*-wire used for wiring, 2 and 3 capillary heaters: two rectangle *Cu*-blocks are placed around the capillary and on the top of those rectangles two 3 Ω resistances with a maximum power of 10 Watt are placed (resistances are connected in series), 4 Cernox temperature sensors (model: CX-1080-CU, CX-1050-CU) are connected via four probe method, 5 pressure cell with a heater foil (*MINCO*, France), 6 inner can (made of *Cu*) with heater foils (*MINCO*, France).

ditions. In order to use the ^4He-gas compressor for high-pressure measurements ($P >$ 18 MPa), a large volume of the high-pressure stage together with a micro-pump will be installed to compensate for the pressure change due to temperature sweeps. The limitation of this capacitive dilatometer is given by the pressure medium, *i.e.*, helium should not go to the solid phase which for a given pressure sets a limit for the lowest accessible temperature, cf. the P-T phase diagram [37, 38].

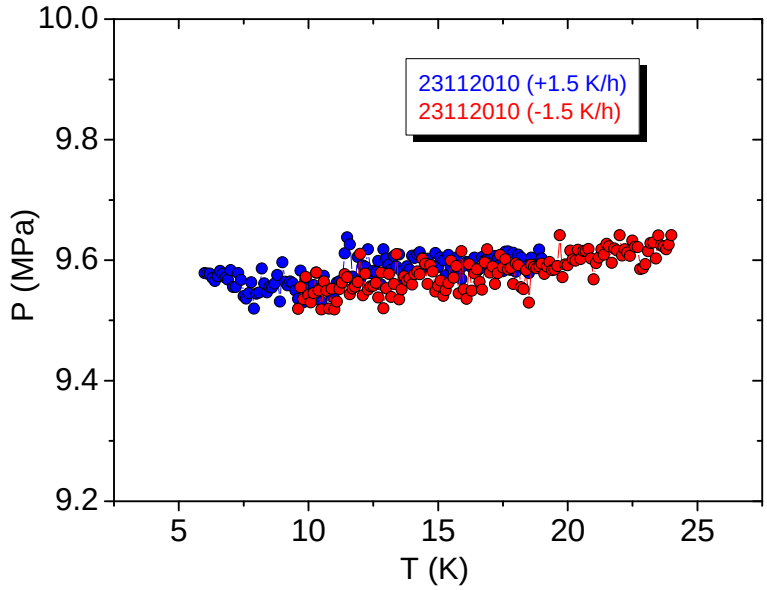

Figure 2.2.7: Readout of the pressure sensor (heavily doped *n-InSb* single crystal) for a temperature sweep in measurements on azurite at $P \approx 9.5$ MPa. A temperature sweep rate of $\pm$ 1.5 K/hour is used.

A heavily doped *n-InSb* single crystal is used as a pressure sensor, placed inside the pressure cell in order to detect the actual pressure in the pressure cell. This gauge is also connected via the four-probe method where the maximum allowable current is 50 mA. A HP 3245A Universal Source is used as a current source and a Keithley 2182A Nanovoltmeter is used to detect the voltage drop across the gauge by a DC method. This gauge is calibrated as a function of temperature (T) and pressure (P). By employing this technique, it is possible to resolve the pressure within $\Delta P \simeq \pm$ 0.1 MPa. The main idea of this pressure experiment is to measure the length changes of the material as a function of temperature (T) while the pressure is kept constant, *i.e.*, constant-pressure condition. Fig. 2.2.7 shows the readout of the pressure sensor in measurements on azurite at $P \approx$ 9.5 MPa. The temperature sweep (warming up or cooling down) rate is important in order to ensure thermal equilibrium and check for hysteresis of the pressure. In this case, warming up and cooling down with a rate of $\pm$ 1.5 K/hour is optimum rate to nullify

the pressure hysteresis.

The following empirical formula is used to determine the actual pressure inside the pressure cell:

$$P(T) = [2.73 + 6.434 \cdot 10^{-4} \cdot (T - 77.4K)] \cdot \ln\left[\frac{R(P,T)}{R(P=0,T)}\right](GPa) \tag{2.2.1}$$

where $R(P,T)$ is the resistance of the pressure gauge at any pressure and temperature, $R(P = 0,\ T)$ is the resistance measured as a function of temperature at ambient-pressure. In order to make a precise determination of pressure, the temperature of the pressure gauge should be carefully controlled during the resistance determination [35]. As a matter of fact, continuous measurements have been done with a very slow warming or cooling rate ($\leq \pm$ 1.5 K/hour). When there is a temperature mismatch between the resistances at ambient and finite pressure, the error in pressure determination would be

$$\frac{\Delta P}{\Delta T} = 3 \cdot 10^{-3} GPa/K \tag{2.2.2}$$

That means for $\Delta T = 0.1$ K, the error in pressure would be 0.3 MPa.

A TestPoint v7® program is used as an interface between the devices and the computer to control all measurements [2.2.1].

The overview of the 'thermal expansion under pressure' setup without the compressor is shown in Fig. 2.2.8.

2.3 Electrochemical crystallization technique

Electrocrystallization is a unique technique to produce single crystals of organic charge-transfer salts. The electrodes are made of platinum and separated by an ultra-fine porosity glass frit. An electrolyte solution which contains the anions is inserted in both chambers and the donor molecules are added to the solution. The glass frit acts as a filter. The whole process has to be done in an inert-gas atmosphere. After that, the electrodes have to be connected with a power supply. Single crystals are grown generally on the anode surface. The whole process takes long time, usually several days, weeks or even few months [8].

[2.2.1] The test point program for Lakeshore340 temperature controller was originally written by Prof. Dr. Jens Müller.

Figure 2.2.8: Picture of the whole setup 'thermal expansion under pressure'.

2.4 Calculation of thermal expansion coefficient (α)

For the ideal plate capacitor with area A, the capacitance is given by

$$C = \epsilon_r \cdot \epsilon_0 A/d \tag{2.4.1}$$

where $\epsilon_0 = 8.854\times 10^{-12}$ F m^{-1} is the free space permittivity and ϵ_r is the dielectric constant of the medium. As the sample is placed on the top of the upper moveable capacitor plate, the thermal expansion of the sample causes the variation of the distance between the parallel capacitance plates d. After taking into account the inhomogeneities of the electric field at the border of the capacitor plates, the change in the distance between the two capacitor plates is related to changes in the capacitance via

$$\Delta d = -\epsilon_0 \pi r^2 (1+\delta)\left(\frac{C_2 - C_1}{C_1 \cdot C_2} - 2\frac{\Delta r}{r_1}\cdot\frac{1}{C_2}\right) \tag{2.4.2}$$

where the last term takes into account the lateral expansion of the capacitor plates, r is the radius of the plate and δ is a constant whose value can be calculated by knowing the geometrical parameters of the capacitor [32]. The dilatometer cell, used to perform thermal expansion under pressure measurements, is made of silver (Ag). By putting all the values for the geometry factors and constants, Eq. (2.4.2) gives for the silver-made dilatometer cell, used for thermal expansion under pressure measurements

$$\Delta d = -0.1398\left(\frac{C_2 - C_1}{C_1 \cdot C_2} - 2\frac{\Delta r}{r_1}\cdot\frac{1}{C_2}\right) cmpF \tag{2.4.3}$$

2.4.1 Cell effect calculation

The cell effect has to be subtracted from the measured Δd in order to get the effect from the sample. So the measured length change is defined as

$$(\Delta l)_{meas} = -(\Delta d) = (\Delta l)_{sample} - (\Delta l)_{cell} \tag{2.4.4}$$

$(\Delta l)_{cell}$ can be obtained by measuring a known reference sample, *e.g.*, aluminium (Al)[2.4.1] whose thermal expansion is known [39].

$$(\Delta l)_{cell}(T) = (\Delta l)_{Al}(T) - (\Delta l)^{Al}_{meas}(T) \tag{2.4.5}$$

If the length of the reference sample and the unknown sample is the same, namely l, then Eq. (2.4.4) gives,

$$\left(\frac{\Delta l}{l}\right)_{sample}(T) = \frac{1}{l}\left[(\Delta l)^{sample}_{meas}(T) - (\Delta l)^{Al}_{meas}(T)\right] + \left(\frac{\Delta l}{l}\right)_{Al}(T) \tag{2.4.6}$$

[2.4.1] In order to calculate the cell effect for the 'thermal expansion under pressure' setup, an aluminium (Al) sample of length 7 mm is used. To cross-check the cell effect calculated from the Al sample, two other samples, namely, copper (Cu) and silver (Ag) each of length 7 mm are used.

In order to get the value of the thermal expansion coefficient (α), one has to differentiate the above Eq. (2.4.6) with respect to temperature (T), *i.e.*,

$$\alpha = \left.\frac{\mathrm{dln}l(T)}{\mathrm{d}T}\right|_P \tag{2.4.7}$$

So if one knows the literature value of the material from which the capacitor plates are made and the cell effect, the thermal expansion coefficient of the unknown sample can be calculated easily.

2.5 Van der Waals equation of state

The ideal gas equation of state is defined by

$$PV = nRT \tag{2.5.1}$$

where P is the absolute pressure of the gas, V is the volume, n is the amount of substance, R is the gas constant and T is the absolute temperature. This equation is most accurate in the case of monatomic gases at high temperatures and low pressures. But at higher pressure and lower temperature, one has to take into account the volume correction of the molecules and the attraction between them. This results in an equation of state, known as van der Waals equation

$$\left(P + \frac{n^2 a}{V^2}\right)(V - nb) = nRT \tag{2.5.2}$$

where a is a measure of the attraction between the particles and b is the volume excluded by a mole of particles. So the particle number is an important factor to deal with which is a function of P, V and T. The above Eq. (2.5.2) can be written in terms of n

$$\left(\frac{ab}{V^2}\right)n^3 + \left(\frac{-a}{V}\right)n^2 + (RT + Pb)n + (-PV) = 0 \tag{2.5.3}$$

This is a cubic equation of n which can be simplified to

$$An^3 + Bn^2 + Cn + D = 0 \tag{2.5.4}$$

The solution of the above equation gives how the number of particles (n) change as a function of temperature (T) and pressure (P) while the volume (V) is kept constant.

There are some standard methods for achieving the solution of the above cubic equation. First of all, one has to modify the equation by replacing

$$n = m - \frac{B}{3A} \tag{2.5.5}$$

After replacing one gets,

$$m^3 + Em = F \tag{2.5.6}$$

which is known as *depressed cubic equation*, where

$$E = \frac{m}{A} \cdot \left(C - \frac{B^2}{3A} \right) \tag{2.5.7}$$

and

$$F = \frac{1}{A} \cdot \left(\frac{BC}{3A} - \frac{2}{27} \frac{B^3}{A^2} - D \right) \tag{2.5.8}$$

Now one can find s and t such that

$$3st = E \tag{2.5.9}$$

$$s^3 - t^3 = F \tag{2.5.10}$$

It turns out that $m = s$ - t will be a solution of the depressed cubic equation. After substituting and simplifying, one can easily get the solution where

$$s = \left(\frac{F \pm \sqrt{F^2 + \frac{4E^3}{27}}}{2} \right)^{1/3} \tag{2.5.11}$$

and

$$t = \left(\frac{-F \pm \sqrt{F^2 + \frac{4E^3}{27}}}{2} \right)^{1/3} \tag{2.5.12}$$

So the final solution of the van der Waals equation will be

$$n = \left(\frac{F \pm \sqrt{F^2 + \frac{4E^3}{27}}}{2} \right)^{1/3} - \left(\frac{F \pm \sqrt{F^2 + \frac{4E^3}{27}}}{2} \right)^{1/3} - \frac{B}{3A} \tag{2.5.13}$$

where

$$A = \frac{ab}{V^2} \tag{2.5.14}$$

$$B = -\frac{a}{V} \tag{2.5.15}$$

$$C = RT + Pb \tag{2.5.16}$$

$$D = -PV \tag{2.5.17}$$

$$E = \frac{C}{A} - \frac{B^2}{3A^2} \tag{2.5.18}$$

$$F = \frac{BC}{3A^2} - \frac{2}{27} \cdot \frac{B^3}{A^3} - \frac{D}{A} \tag{2.5.19}$$

So from the Eq. (2.5.13), the number of particles, *i.e.*, the number density (n) can be calculated for an open system, *i.e.*, a system connected to a particle reservoir, as a function of volume, pressure and temperature.

2.6 Calculation of the dielectric constant (ε_r)

As the value of the capacitance is directly proportional to the dielectric constant (ε_r) of the medium, it is very important to know the variation of the dielectric constant of the medium as a function of volume (V), pressure (P) and temperature (T). More precisely, at a particular volume and temperature, the variation of pressure causes the change in the number of particles (N), *i.e.*, the density of the medium. So it is very important to know how the number of particles changes as a function of volume, pressure and temperature (Eq. (2.5.13)). The Clausius-Mossotti equation which works pretty well for a wide class of dielectric liquids and gases [40, 41, 42] yields

$$\frac{\varepsilon - 1}{\varepsilon + 2} = \frac{N_A \rho_m \alpha}{3M} \tag{2.6.1}$$

where N_A is the Avogadro's number, ρ_m is the mass density, M is the molecular weight, α is the molecular polarizability and ε is the dielectric constant.

The above equation can be written in the following form, too

$$\frac{\varepsilon - 1}{\varepsilon + 2} = \frac{n\alpha}{3} \tag{2.6.2}$$

where n is the number density which can be obtained from the Eq. (2.5.13).

From Eq. (2.6.2), the dielectric constant of the medium, $\varepsilon_r = \varepsilon_r(P, T, V)$ can be calculated provided n is known. Fig. 2.6.1 shows the variation of the dielectric constant (ε_r) for a van der Waals gas (^4He) as a function of temperature while the pressure ($P =$ 1.0, 2.0, 6.2 and 9.5 MPa) and volume are fixed, which is relevant for our experiments as we performed temperature sweeps for different fixed pressure values. The calculated

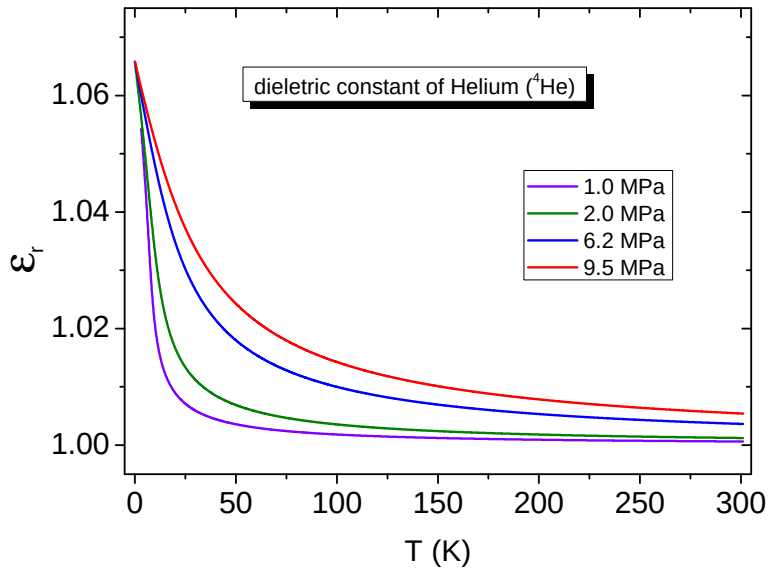

Figure 2.6.1: The variation of the dielectric constant (ε_r) for a van der Waals gas (^4He) as a function of temperature while the pressure (P = 1.0, 2.0, 6.2 and 9.5 MPa) and volume are fixed.

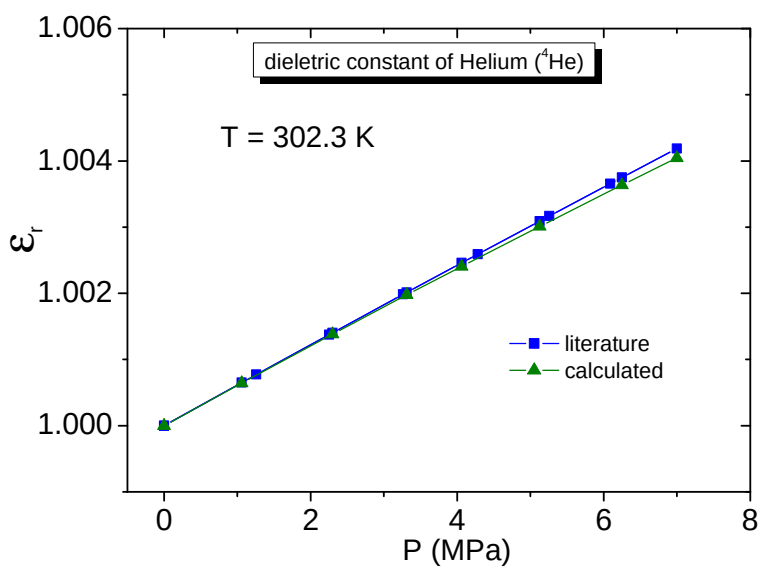

Figure 2.6.2: The variation of the dielectric constant (ε_r) for a van der Waals gas (^4He) as a function of pressure while the temperature (T = 302.3 K) and volume are fixed. Blue squares are the literature values [43] and green triangles are the calculated values.

values of the dielectric constants show a nice agreement with the literature value [43], unfortunately available only at high temperatures and low pressures, which is shown in Fig. 2.6.2. As shown in Fig. 2.6.1, the effect of the pressure on ε_r for $P \leq 10$ MPa in the temperature range of interest is expected to be in the percent range. Measurements on azurite in the same pressure range, however, indicate that at low temperatures the effect of the pressure medium on the capacitance readout is much larger. To account for that an experimentally determined "pressure-induced cell effect" needs to be subtracted from the raw data. Nevertheless an analytical formula would be helpful to estimate this cell effect at any pressure and temperature.

2.6.1 Pressure-induced cell effect

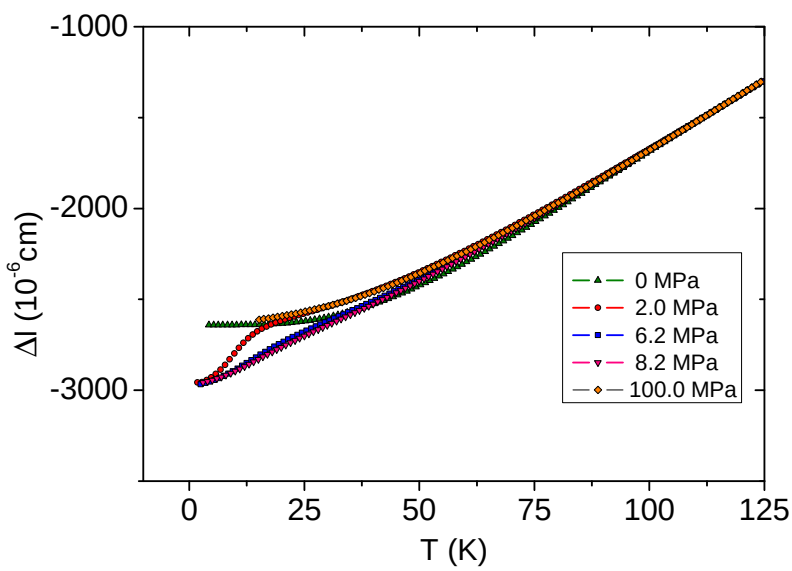

Figure 2.6.3: Cell effect as a function of temperature for different finite pressure values (2.0, 6.2, 8.2 and 100 MPa) together with the ambient-pressure cell effect. The data are shown up to a temperature of 125 K as all curves merge at higher temperatures.

As the lower pressure values ($P \lesssim 2.5$ MPa) allowed us to go down to a temperature as low as 1.5 K, so where helium is still liquid [38], some unexpectedly large anomaly at lower temperature is observed while measuring azurite (see chapter 5). As the pressure value was reduced, the corresponding effect became even bigger. In order to get the real contribution of an unknown sample under pressure, one has to find out the so-called "pressure-induced cell effect" for a sample whose literature value is known at ambient-pressure. In the present case, an annealed *Al* and *Cu* reference samples each of length 7

mm were used to calculate the "pressure-induced cell effect" for different constant-pressure values. Fig. 2.6.3 shows the cell effect for the above-mentioned reference samples for the finite-pressure values 2.0 MPa, 6.2 MPa, 8.2 MPa and 100.0 MPa together with the ambient-pressure value. The solidification temperatures of helium are 2.7 K, 3.4 K and 14.2 K for the corresponding pressure values 6.2 MPa, 9.5 MPa and 100.0 MPa, respectively. The lower pressure data, namely, 2.0 MPa shows a huge anomaly at around 15 K in the "cell effect", well distinguished from the other pressure values. The anomaly is even larger in the case of 1.0 MPa (not shown here). But at higher pressure values (6.2 MPa and 8.2 MPa), this anomaly in the "cell effect" seems to be suppressed. We believe that this anomalous behavior is related to the proximity to the critical point of helium ($P_c = 0.227$ MPa, $T_c = 5.2$ K) [37] as it is nearby. It was very difficult to perform the experiments at lower pressure values by maintaining the constant-pressure conditions. As a matter of fact, a pressure hysteresis was observed as a function of temperature upon warming and cooling. In order to avoid this problem, the measurements were performed with a much slower temperature sweep rate ($\pm$ 0.1 K/hour to $\pm$ 0.5 K/hour).

3

Charge-transfer salts

Organic charge-transfer salts display various features related to strongly correlated electron systems. In the vast majority of D_mX_n salts, the donor-acceptor molecular ratio m:n is fixed to 2:1, where D is an organic electron-donor and X is an inorganic electron-acceptor. The unpaired carriers of the charge-transfer salts are generated via a partial charge-transfer process between donor and acceptor molecules. TTF-TCNQ, a quasi-one-dimensional organic conductor (m:n = 1:1), was the first synthesized organic charge-transfer salt, where TTF is the electron donor and TCNQ is the electron acceptor [44]. There are an enormous numbers of donor molecules, *e.g.*, TMTTF, TMTSF, BEDT-TTF, etc, which act as building blocks of organic conductors and superconductors. Normally, the acceptors adopt a closed-shell configuration and are thus not involved in the electronic properties of the material.

There are similarities found in the organic superconductors and the high-temperature cuprate superconductors. The phase diagrams for both look similar including unconventional metallic properties. The layered structure and the strong interactions between the electrons make the physics interesting for these compounds [45].

3.1 Quasi-one-dimensional salts

The prominent examples of organic charge-transfer salts are the quasi-one-dimensional (1D) TTF-TCNQ, $(TM)_2X$ (TM stands for TMTTF or TMTSF) and the quasi-two-dimensional (2D) $(BEDT\text{-}TTF)_2X$ (commonly abbreviated $(ET)_2X$). In the case of TTF-TCNQ or $(TM)_2$ salts, the donor molecules form segregated infinite stacks. As a matter of fact, the overlap of π-orbitals occurs along the stacking axis which leads to a quasi-1D character. More precisely, in the case of the $(TMTSF)_2X$ compounds, the spacing between the molecules along the stacking direction is smaller than the van der Waals radii of the Se atoms which have a large electron cloud. The π-orbitals of the partially-filled

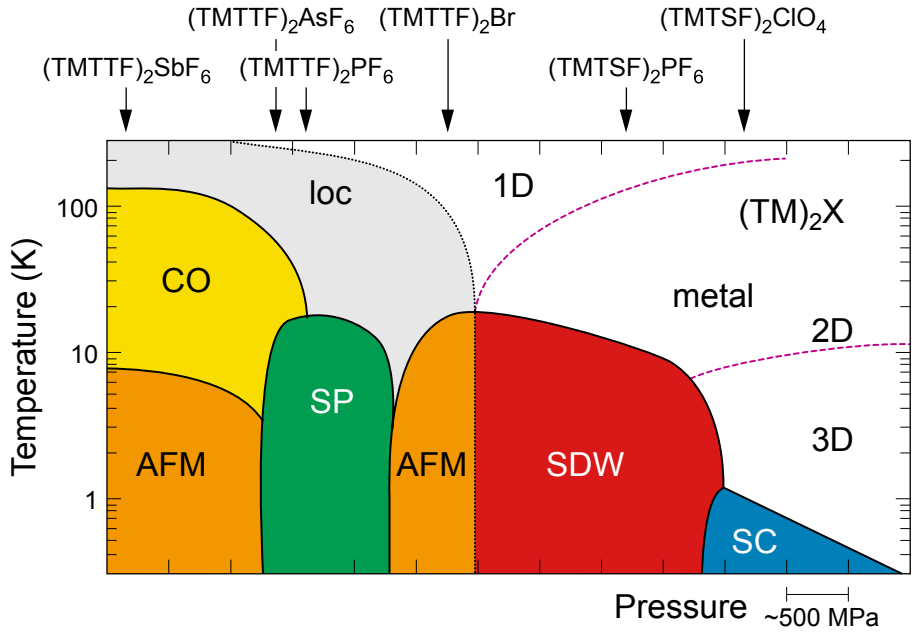

Figure 3.1.1: Temperature-pressure phase diagram of quasi-one-dimensional TMTTF and TMTSF charge-transfer salts (adapted from ref. [47]). The arrows indicate the positions of the respective salts in the phase diagram at ambient-pressure. Solid lines are the phase boundaries and the dashed lines are the indication of crossovers. By changing the chemical pressure or physical pressure, the phase diagram can be tuned to obtain different phases like localization (*loc*), charge ordering (*CO*), spin-Peierls (*SP*), antiferromagnetism (*AFM*), spin-density-wave (*SDW*), and superconductivity (*SC*).

outer molecular shells overlap and this is how the electronic band structure is formed. Depending upon the spatial arrangement and the relative angle, the electronic properties of the materials change, leading to quasi-1D or quasi-2D in character. In quasi-1D compounds, mainly the $(TM)_2X$ family, the anions are centrosymmetric, *e.g.*, $X = PF_6$, AsF_6, SbF_6. $(TMTSF)_2PF_6$ was the first organic compound where superconductivity was observed with a $T_c = 0.9$ K under hydrostatic pressure of 1.2 MPa [46], where it showed a metal-insulator transition at around 12 K at ambient-pressure. By changing the anion (chemical pressure) or applying hydrostatic pressure, a rich phase diagram can be drawn with phases like localization (*loc*), charge ordering (*CO*), spin-Peierls (*SP*), antiferromagnetism (*AFM*), spin-density-wave (*SDW*), and superconductivity (*SC*), cf. Fig. 3.1.1 [47].

3.2 Quasi-two-dimensional salts : κ-$(ET)_2X$

The BEDT-TTF (*bis(ethylenedithio)-tetrathiafulvalene*) molecule, abbreviated as ET, which is an extension of TTF-derivative with a chemical formula $C_6S_8[(CH_2)_2]_2$, is the main building block of two-dimensional organic conductors.

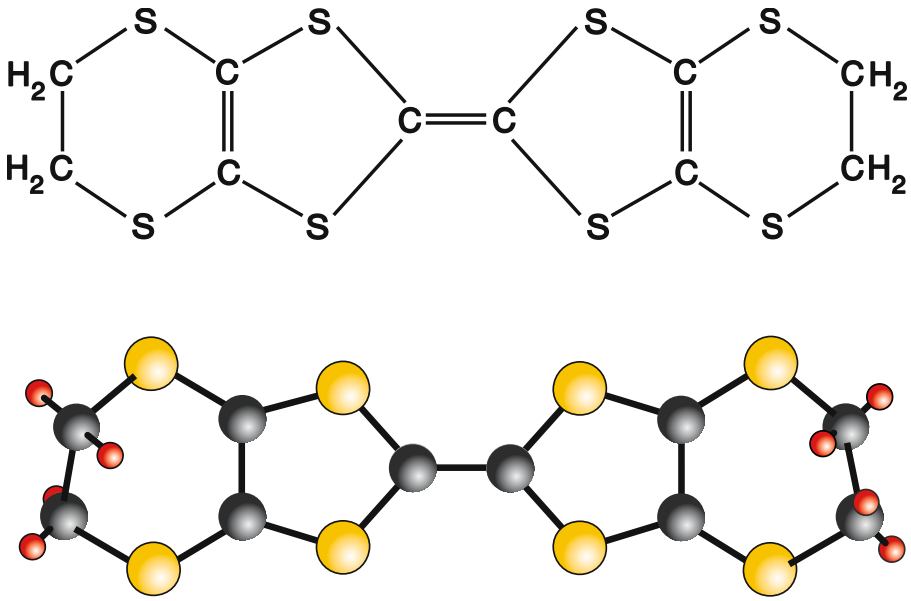

Figure 3.2.1: Structure of the BEDT-TTF (ET) molecule whose chemical formula is $C_6S_8[(CH_2)_2]_2$. There are four ethylene $[(CH_2)_2]_2$ end groups which play a key role for the kinetic, glass-like transition (T_g) (adapted from ref. [48]).

Fig. 3.2.1 shows the molecular structure of the ET molecule. The motional degrees of freedom of the ethylene $[(CH_2)_2]_2$ end groups of the ET molecule play an important role for the glass-like transition (T_g), namely, they become frozen in below T_g for the compounds κ-(BEDT-TTF)$_2$X, where X = Cu(NCS)$_2$, Cu[N(CN)$_2$]Br and Cu[N(CN)$_2$]Cl. The cooling and warming rates effect the ground-state properties of these materials [49]. For the ET-based salts, the orbital overlap between the adjacent molecules is stronger compared to the quasi-1D compounds and occasionally, there is a strong face-to-face interaction. As a matter of fact, the electronic structure of the ET-based salts show a quasi-2D character. Based on the packing motifs of the ET molecules, it is differentiated in a couple of phases, namely, defined by the Greek characters α, β, κ etc, shown in Fig. 3.2.2.

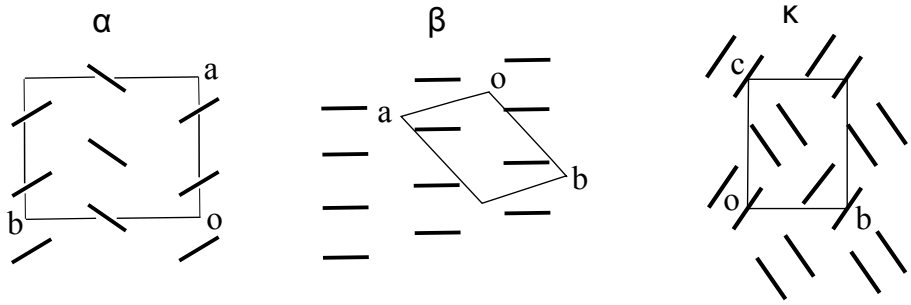

Figure 3.2.2: Schematic packing motifs of the ET molecules in the α-, β- and κ- phases, viewed along the long axis of the ET molecules [8].

Out of these phases, the κ-phase is a special type where two ET molecules form a dimer and the adjacent dimers are arranged themselves in an almost orthogonal fashion. Assuming a strong intra-dimer interaction, an effective dimer-dimer interaction model is constructed where *intra*- and *inter*-dimer interactions can be calculated.

Apart from their complicated crystal structure, $(ET)_2X$ salts form layered structures consisting of alternating conducting and insulating layers which is shown in Fig. 3.2.3.

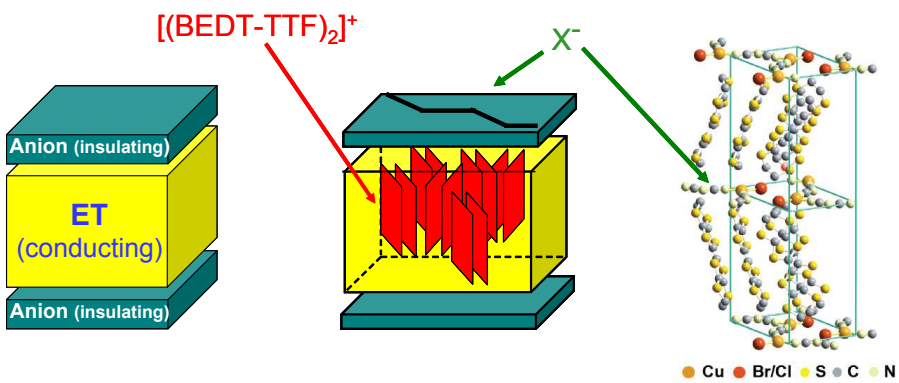

Figure 3.2.3: Structure of the κ-phase of the quasi-2D organic charge-transfer salts. They form a layered structure, namely, conducting ET layers are separated by the insulating anion (X) layers. In the extreme right side, the crystal structure of κ-$(BEDT\text{-}TTF)_2X$ is shown, where X = $Cu[N(CN)_2]Br$ and $Cu[N(CN)_2]Cl$. Different color coding signifies different atoms in the unit cell.

One material class of high interest are the quasi-2D κ-$(ET)_2X$ salts [50] with X= $Cu(NCS)_2$, $Cu[N(CN)_2]Br$, $Cu[N(CN)_2]Cl$ and modifications finely tuned across the metal-insulator transition by chemical substitution, hydrostatic pressure, and/or magnetic fields. There is no center of inversion symmetry because of the polymeric nature of the anions. So the anion substitution or little change of orientation of the ET molecules may effect significantly the overlap of the π-orbitals between the adjacent molecules. As a result, it severely changes the electronic properties of the materials.

A conceptual phase diagram has been proposed where the properties of the materials are controlled by a single parameter U/W, *i.e.*, the strength of the effective on-site Coulomb repulsion (U) relative to the width of the conduction band (W) [52, 53], cf. Fig. 3.2.4. It has been assumed that the changes in the parameter U/W can be induced either in a discrete manner by chemical substitution, or in a continuous way by applying hydrostatic pressure [54]. According to the phase diagram, the antiferromagnetic insulator (AFI) with X = $Cu[N(CN)_2]Cl$ and the correlated metal with X= $Cu[N(CN)_2]Br$ lie on opposite sides of the bandwidth-controlled Mott transition. The fully deuterated κ-$(d8\text{-}ET)_2Cu[N(CN)_2]Br$, where all the protons in the terminal ethylene groups are replaced by deuterium (d), is situated right at the AFI-to-metal/superconductor boundary. Partial substitution of the 2×4 H-atoms in the ethylene groups by deuterium atoms per-

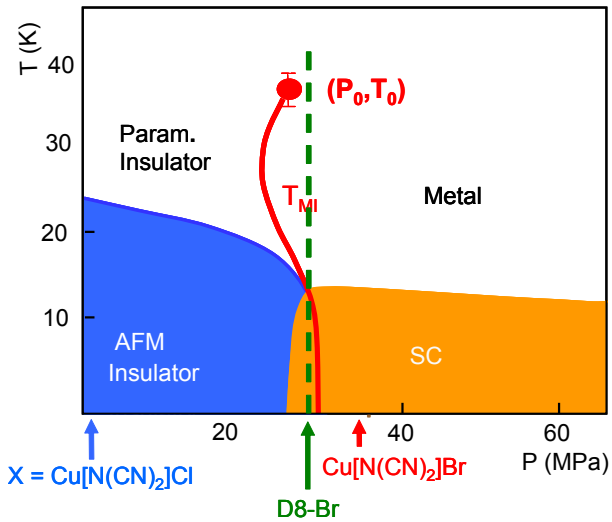

Figure 3.2.4: T-P phase diagram of the κ-(ET)$_2$X salts with the anion X = Cu[N(CN)$_2$]Br, Cu[N(CN)$_2$]Cl. The position of the anions at ambient-pressure are indicated by arrows. Antiferromagnetic (AFM) and superconducting (SC) states are separated by a first-order s-shaped transition line which ends at a second-order critical point [11, 51].

mits this system to be finely tuned across the phase boundary [2].

In contrast to the above-discussed two-dimensional charge-transfer salts, X = Cu$_2$(CN)$_3$ shows no long-range magnetic order down to 32 mK and subsequently is proposed to be a good candidate of a quantum spin-liquid ground state [17]. Interestingly, this compound does not show any glass-like transition although it has also two-dimensional BEDT-TTF as donor molecules. Properties of this compound will be discussed in detail in chapter 4.

3.3 Ultrasonic measurements under helium gas pressure

As discussed in the last section that the effect of chemical or physical pressure plays an important role in the organic materials, ultrasonic measurements under helium gas pressure is also a powerful technique to verify this. Sound velocity is proportional to the square root of the compression modulus $C_{22} \sim \kappa_e^{-1} + \kappa_l^{-1} + \kappa_{el}^{-1}$ where κ_e is the compressibility of the electronic degrees of freedom, κ_l is the lattice compressibility and κ_{el} is the strength of the electron-lattice interaction. Consequently, ultrasound measurements have been studied for the two-dimensional κ-(ET)$_2$X salts [55, 56, 57, 58]. Theoretically it has proposed from the dynamical mean-field theory ($DMFT$) of the Hubbard model that the compressibility of the electronic degrees of freedom κ_e diverges at the finite temperature second-order critical end point of the first-order Mott transition line [59, 60]. This scenario fits perfectly with the afore-mentioned organic materials. Moreover, a

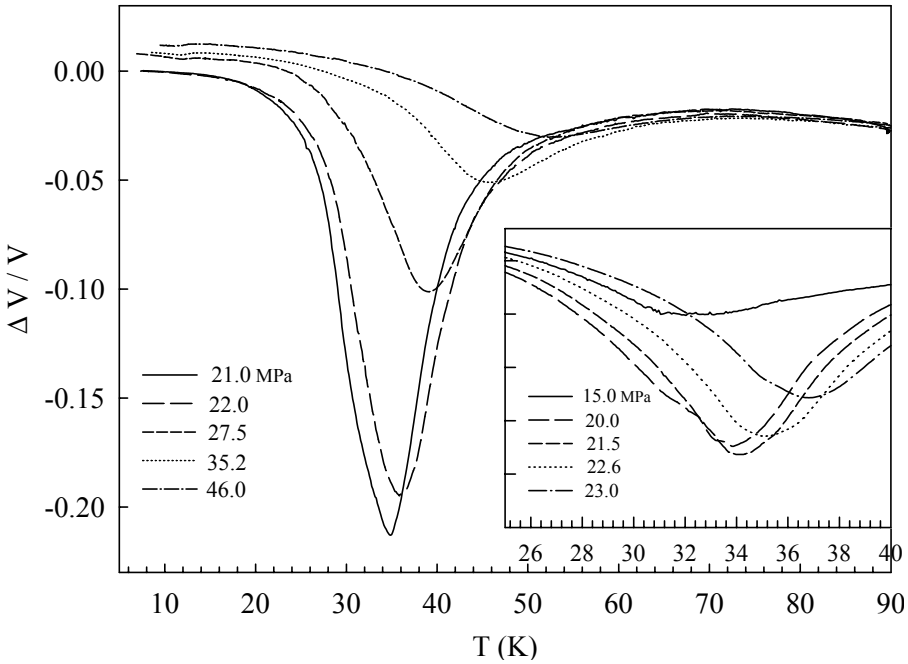

Figure 3.3.1: Temperature dependence of the relative sound velocity for κ-$(ET)_2Cu[N(CN)_2]Cl$ compound under helium gas pressure relative to the value at 90 K (adapted from ref. [55]). Inset: the data at lower pressure values ($P < 23$ MPa). For pressure 21 MPa, it shows a maximum amplitude at 34 K which is a signature of the second-order critical end point.

nonmonotonous temperature dependence due to the coupling between the phonons and electrons in a strongly correlated metal has also been predicted [61].

κ-$(ET)_2Cu[N(CN)_2]Cl$ is one of the best candidates to study the behavior near the critical end point of the first-order Mott transition line. One needs only $\sim$ 30 MPa, which is easily accessible in the laboratory, to cross the first-order phase boundary. Fig. 3.3.1 shows the temperature dependence of the relative sound velocity at different finite pressure values. The amplitude of the relative sound velocity increases in size and shifts to higher temperature as pressure increases. It shows a huge anomaly at 34 K for $P = 21$ MPa where the amplitude is maximum, signifying the critical point. This is consistent with the theoretical prediction which is mentioned earlier. Based on these measurements, the T-P phase diagram can be constructed, which is consistent with that shown in Fig. 3.2.4 [55].

3.4 Controversy on the Mott universality class

There is a controversy on the universality class of the Mott transition in the κ-$(ET)_2X$ charge-transfer salts determined near the second-order finite temperature critical end

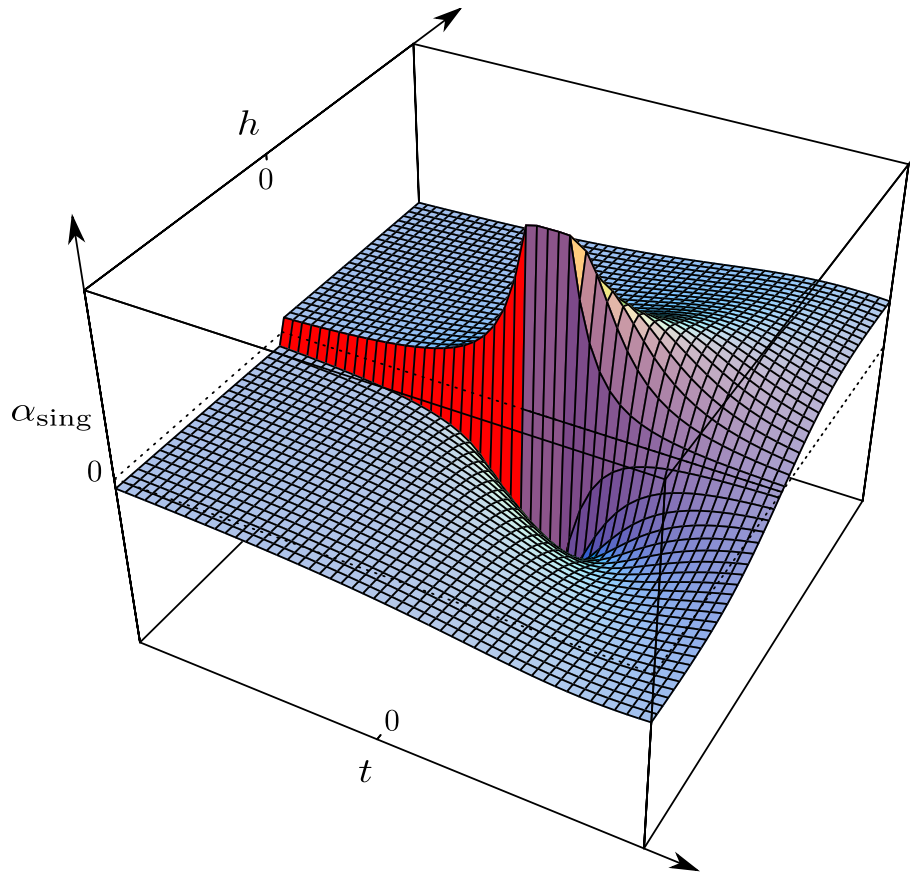

Figure 3.4.1: Singular part of the thermal expansivity α_{sing} as a function of t and h, where $t = [T\text{-}T_c\text{-}\zeta(p\text{-}p_c)]/T_0$ and $h = [p\text{-}p_c\text{-}\lambda(T\text{-}T_c)]/p_0$ (adapted from ref. [13]). The almost divergence of the thermal expansivity and the sign change are shown near the critical end point.

point. Assuming an analogy to the liquid-gas transition, proposed by Castellani *et al.*, an Ising universality class is expected [62]. For the $(V_{1-x}Cr_x)_2O_3$, a Mott insulator, it is reported that the critical behavior near the critical end point is mean-field like with some indication of 3D Ising critical exponents by performing conductivity measurements as a function of pressure and temperature [10]. For the charge-transfer salt, κ-$(ET)_2Cu[N(CN)_2]Cl$, it has been claimed, however, that the critical behavior is of unconventional type [11]. Thermal expansion measurements have been performed on the deuterated κ-$(ET)_2Cu[N(CN)_2]Br$, lying on the verge of first-order Mott transition line. By employing a Grüneisen-scaling Ansatz, *i.e.*, assuming that the anomaly in the thermal expansion is proportional to the anomaly in the specific heat, the critical behavior is determined which is also of unconventional type, but inconsistent with any of the proposed universality classes [2]. Recently, a scaling theory of the lattice effects has been proposed near the finite-temperature critical end point. Based on this theory, it is shown that the Grüneisen-scaling breaks down in the vicinity of the finite-temperature critical end point. As a matter of fact, an almost divergence and a sign change of the thermal expansion

coefficient upon approaching the critical end point have been predicted, which is shown is Fig. 3.4.1. After reanalyzing the thermal expansion data in terms of a scaling function, it is found that this is in good agreement with the 2D Ising universality class [13]. Experimentally this can be verified by measuring the thermal expansion under pressure. In fact, this was one of the motivations to design the 'thermal expansion under pressure' instrument, elaborately discussed in this thesis.

4

Organic 2D quantum spin-liquid – κ-(BEDT-TTF)$_2$Cu$_2$(CN)$_3$

The organic charge-transfer salt κ-(BEDT-TTF)$_2$Cu$_2$(CN)$_3$ is a Mott insulator with a quasi-two-dimensional (2D) triangular-lattice structure where the effect of frustration plays an important role[4.0.1]. The ground state of the other Mott insulators within this family of charge-transfer salts (κ-(BEDT-TTF)$_2$X) studied so far is antiferromagnetic. But this material lacks long-range magnetic order down to 32 mK, which is four orders of magnitude lower than the estimated nearest-neighbor Heisenberg exchange coupling $J/k_B = 250$ K, and has been proposed to be a good candidate for a quantum spin-liquid (*QSL*) ground state [17, 63]. Fig. 4.0.4 shows the magnetic susceptibility as a function of temperature after subtracting the core diamagnetic contribution for the compounds κ-(BEDT-TTF)$_2$X, where X = Cu$_2$(CN)$_3$ and Cu[N(CN)$_2$]Cl [17]. Upon cooling from room temperature, the susceptibility value for κ-(BEDT-TTF)$_2$Cu$_2$(CN)$_3$ increases monotonically followed by a broad hump at 70 K and then it decreases rapidly. At lower temperature, it stays in the paramagnetic region. This data has been fitted to the high-temperature series expansion for an $S = 1/2$ triangular-lattice Heisenberg model with $J = 250$ K. Even though there is a strong interaction between the spins, this compound shows only short-range order. ^{1}H-NMR measurements down to 32 mK confirm that there is no long-range order as there is no splitting of the NMR peaks, as shown in Fig. 4.0.2 [17]. In comparison, κ-(BEDT-TTF)$_2$Cu[N(CN)$_2$]Cl, a Mott insulator with weaker magnetic frustration, shows an antiferromagnetic transition at $T_N \simeq 27$ K which is confirmed by the magnetic susceptibility and ^{1}H-NMR measurements [17, 64].

[4.0.1] The results of this chapter have been published in the following journals.
1. **R. S. Manna**, M. de Souza, A. Brühl, J. A. Schlueter, and M. Lang, Phys. Rev. Lett. **104**, 016403 (2010).
2. M. Lang, **R. S. Manna**, M. de Souza, A. Brühl, and J. A. Schlueter, Physica B **405**, S182 (2010).
3. **R. S. Manna**, M. de Souza, J. A. Schlueter, and M. Lang, Phys. Status Solidi C, 1-3 (2012).
4. H. O. Jeschke, M. de Souza, R. Valentí, **R. S. Manna**, M. Lang, and J. A. Schlueter, Phys. Rev. B **85**, 035125 (2012).

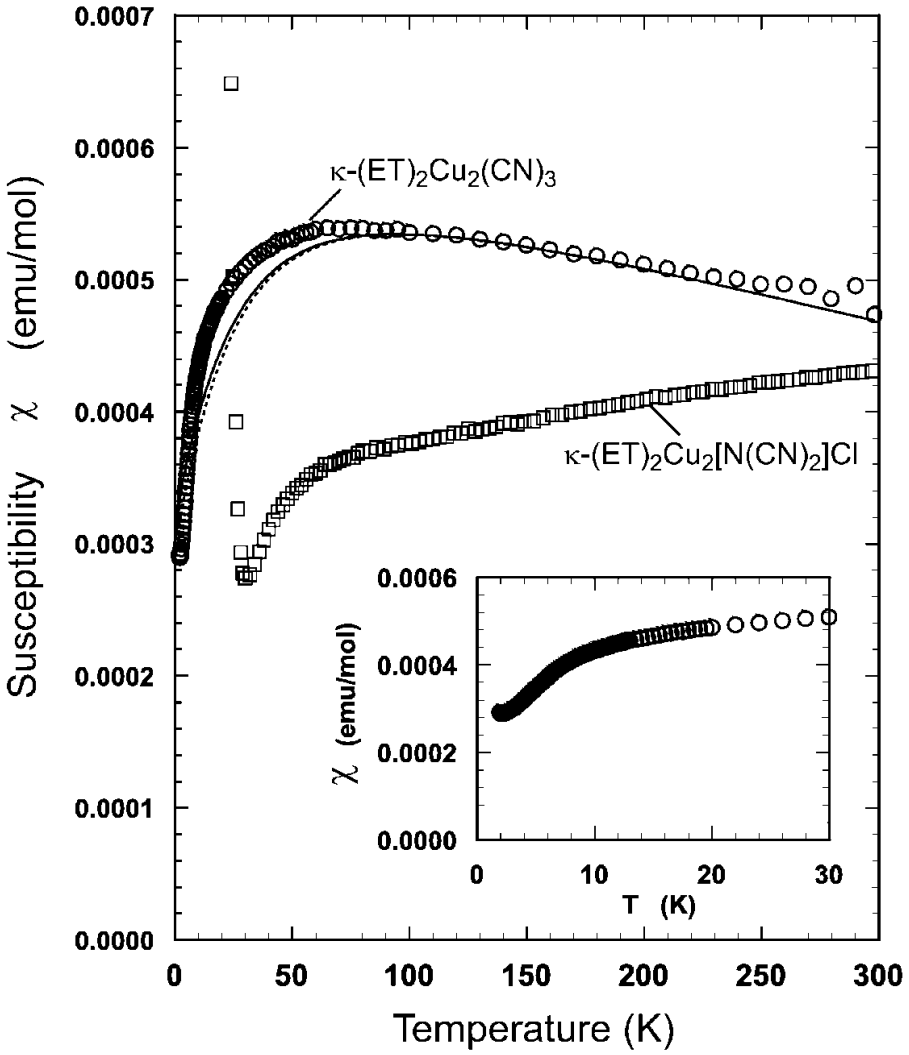

Figure 4.0.1: Magnetic susceptibility as a function of temperature for a polycrystalline sample of the spin-liquid compound κ-(BEDT-TTF)$_2$Cu$_2$(CN)$_3$ in comparison to the κ-(BEDT-TTF)$_2$Cu[N(CN)$_2$]Cl compound (adapted from ref. [17]). No long-range order has been observed for the former compound while the latter shows a long-range antiferromagnetic order at $T_N \simeq 27$ K. High-temperature series expansion of the triangular-lattice Heisenberg model with exchange coupling parameter $J = 250$ K is fitted to the data of the spin-liquid compound. Inset: low-temperature data of spin-liquid material on expanded scales showing that the system remains in the paramagnetic state, even at lower temperature.

Fig. 4.0.3 shows the temperature-pressure phase diagram of κ-(BEDT-TTF)$_2$Cu$_2$(CN)$_3$ which is based on the resistivity and NMR measurements under hydrostatic pressures. Interestingly, a metallic or superconducting state can be achieved by applying few hundred MPa ($\sim$ 350 MPa) pressure [3]. There is a controversy about the nature of the low-lying spin excitations, particularly whether there is a spin gap or not, cf. Fig. 4.0.4, as well as the actual degree of frustration in the material. From the low-temperature specific heat (C_p) measurements, a finite Sommerfeld coefficient ($\gamma = 20 \pm 5$ mJK^{-2}mol^{-1}) has been

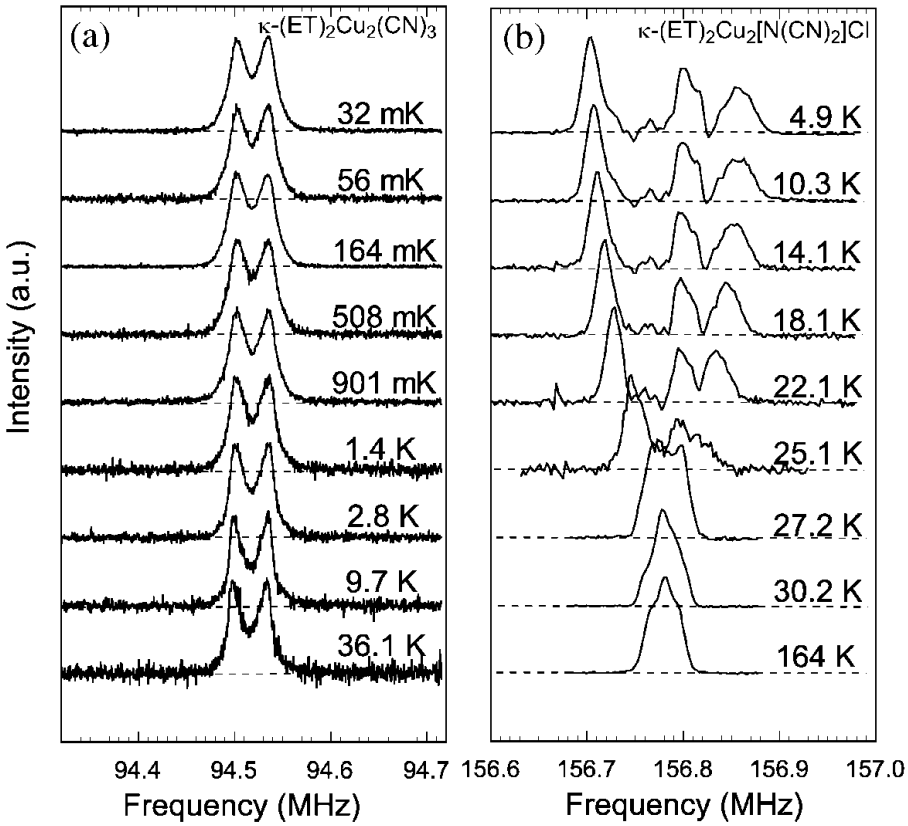

Figure 4.0.2: Temperature dependence of ^{1}H-NMR spectra for the single crystals of κ-(BEDT-TTF)$_2$Cu$_2$(CN)$_3$ and κ-(BEDT-TTF)$_2$Cu[N(CN)$_2$]Cl (adapted from ref. [17]). While the former compound shows no splitting of the NMR peaks down to 32 mK, confirming the spin-liquid ground state, the latter shows a splitting of peaks at $T_N \simeq 27$ K where antiferromagnetic long-range order happens.

obtained from the linear extrapolation in a $C_p T^{-1}$ versus T^2 plot down to $T = 0$ K after subtraction of the nuclear contribution. So it is concluded that the degeneracy of the energy states should give rise to gapless excitations [65, 66, 67]. In contrast, thermal conductivity (κ) measurements show a non-linear curve of κT^{-1} versus T^2 which vanishes at $T \to 0$ K, indicating the presence of gapped spin excitations. Thermal conductivity has been fitted to some exponential function in order to calculate the spin gap (Δ) which is 0.46 K, much smaller compared to J ($\Delta \sim J/500$) [68]. To discuss the controversy of the gapless or gapped excitations, one point to be noted is that the specific heat measurement lacks data at very low-temperature which may confirm the linear dependence of $C_p T^{-1}$ as a function of T^2, cf. Fig. 4.0.4.

Fig. 4.0.5 shows the crystal structure of the κ-phase of the two-dimensional BEDT-TTF layer viewed along the long axes of the BEDT-TTF molecules. Due to strong dimerization of the donor BEDT-TTF molecule, two BEDT-TTF molecules form a dimer unit which is shown as a black dotted circle. Theoretically, a dimer-dimer interaction model can be constructed with the nearest-neighbor hopping integrals t and t' of an anisotropic

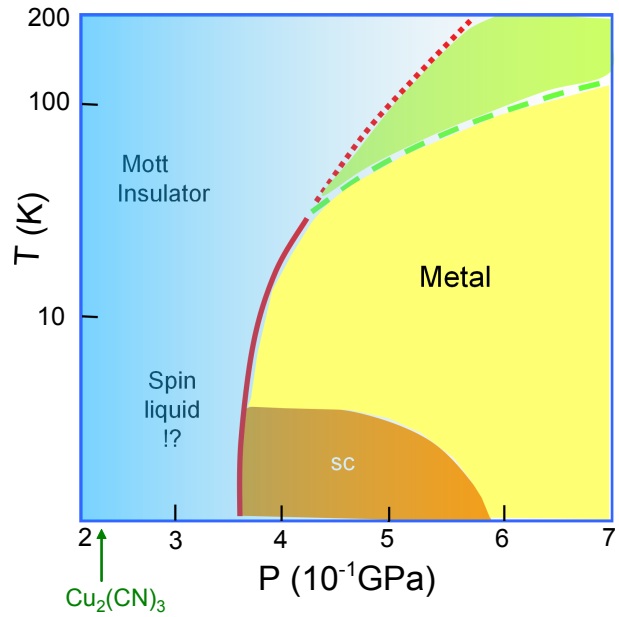

Figure 4.0.3: The temperature-pressure phase diagram of the spin-liquid compound κ-(BEDT-TTF)$_2$Cu$_2$(CN)$_3$. Although there is no long-range order down to 32 mK, superconductivity can be achieved by the application of hydrostatic pressure [3, 17].

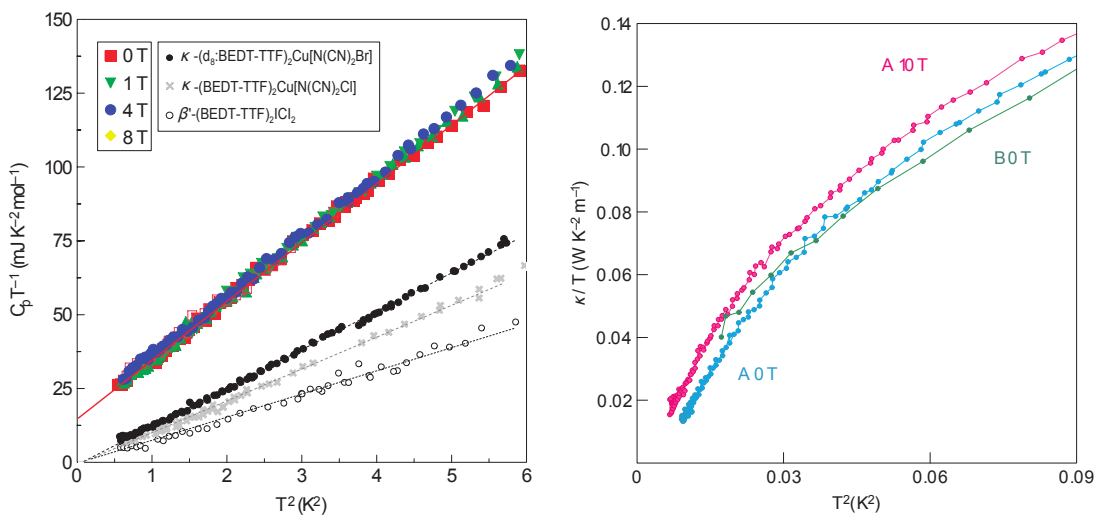

Figure 4.0.4: Specific heat (left panel) and thermal conductivity (right panel) measurements at low-temperature used to obtain the low-lying excitations in κ-(BEDT-TTF)$_2$Cu$_2$(CN)$_3$ (adapted from refs. [65, 68]). A finite Sommerfeld coefficient ($\gamma = 20 \pm 5$ mJK^{-2}mol^{-1}) is obtained from specific heat measurements whereas a spin gap of $\Delta = 0.46$ K is extracted from thermal conductivity measurements (much smaller compared to the exchange coupling constant $J = 250$ K).

triangular-lattice, where $t = (|t_p| + |t_q|)/2$ and $t' = t_{b2}/2$. In the case of κ-(BEDT-TTF)$_2$Cu$_2$(CN)$_3$, the network of *inter*-dimer transfer integrals forms a nearly isotropic triangular-lattice where $t' \sim t$. According to recent *ab initio* calculations [69, 70], the

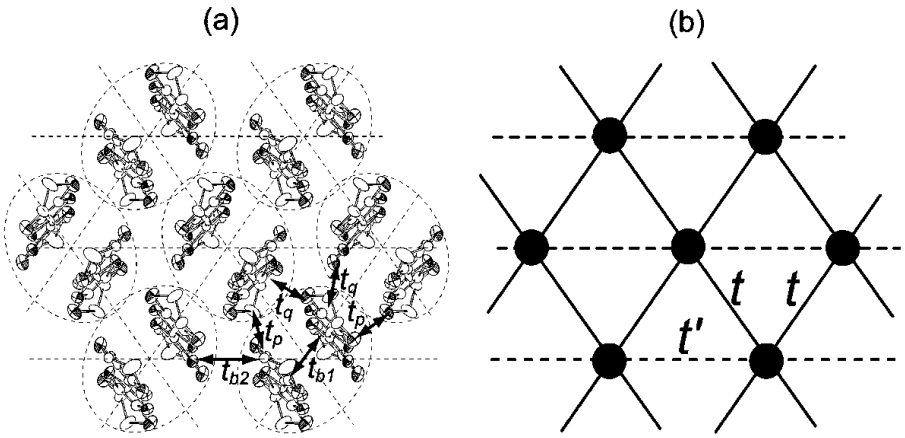

Figure 4.0.5: (a) Crystal structure of the κ-phase charge-transfer salts (BEDT-TTF layer) viewed along the long axes of the BEDT-TTF molecules with transfer integrals t_{b1}, t_{b2}, t_p and t_q. Two BEDT-TTF molecules form a dimer which is shown by the dotted circles. (b) Theoretically, a dimer-dimer interaction model can be constructed with the nearest-neighbor hopping integrals t and t' of an anisotropic triangular-lattice, where $t = (|t_p| + |t_q|)/2$ and $t' = t_{b2}/2$. Black dots correspond to one BEDT-TTF dimer (adapted from ref. [17]).

system is less frustrated ($t'/t \sim 0.8$) than previously estimated from extended Hückel calculations ($t'/t \sim 1.06$) [4]. Even though the value of $t'/t \sim 0.8$, it is still compatible with the spin-liquid ground state, recently studied by using the Monte Carlo techniques based on the backflow correlations for strongly correlated lattice systems [71].

A central issue, which may hold the key for understanding the puzzling low-temperature properties, revolves around the mysterious anomaly at 6 K observed by measuring the specific heat [65], the NMR relaxation rate [17, 72] and the thermal conductivity [68]. Fig. 4.0.6 shows that the 6 K anomaly has been detected by specific heat and thermal conductivity measurements. From the plot of C_pT^{-1} versus T^2 a clear hump is shown at around 6 K in the specific heat after subtraction of the nuclear contribution. By assuming the specific heat of κ-(BEDT-TTF)$_2$Cu(NCS)$_2$ as a phonon background, the 6 K anomaly is even more pronounced after subtraction from the specific heat data of κ-(BEDT-TTF)$_2$Cu$_2$(CN)$_3$ that of κ-(BEDT-TTF)$_2$Cu(NCS)$_2$ [65]. The thermal conductivity data also show a broad hump, and the value of thermal conductivity starts to increase at around 6 K upon cooling [68]. This mysterious anomaly has been assigned to various scenarios such as crossover from a thermal disorder state to a quantum disorder state [65], a phase transition associated with Z_2 vortex formation [73], the pairing of spinons [23], an exciton condensation [24], spin-chirality ordering [74], or a nematic paired state [75, 76]. More elaborately, Lee *et al.* suggested, the pair formation of spinons with parallel momenta breaks the lattice translation, rotational, or even time-reversal symmetries. Spontaneous breakdown of the lattice symmetry implies a finite-temperature phase transition. This model is based on spin degrees of freedom as spinon carries only spin but not charge [23]. Another proposal related to a spin-liquid instability is proposed by

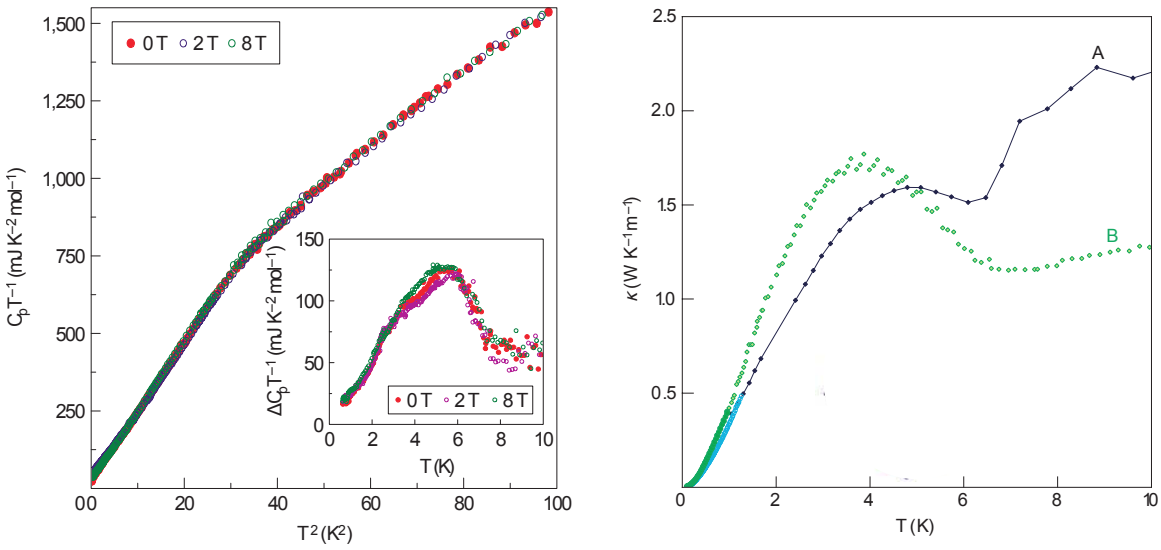

Figure 4.0.6: Mysterious 6 K anomaly of κ-(BEDT-TTF)$_2$Cu$_2$(CN)$_3$ detected by specific heat (left figure) and thermal conductivity (right figure) measurements (adapted from refs. [65, 68]). Clear hump is observed around the 6 K anomaly in the specific heat (from C_pT^{-1} versus T^2) after subtraction of the nuclear contribution and the inset shows the specific heat differences of κ-(BEDT-TTF)$_2$Cu$_2$(CN)$_3$ and κ-(BEDT-TTF)$_2$Cu(NCS)$_2$ in order to extract the 6 K anomaly. In the thermal conductivity measurements, a broad hump is observed and the value of the thermal conductivity starts to increase at around 6 K upon cooling.

Qi *et al.*, suggesting that due to the formation of neutral charge pairs of charge +e and -e fermions, an excitonic condensation can form near a Z_2 spin-liquid of bosonic spinons. This condensate breaks the lattice space group symmetry [24]. Recently, it has been proposed by Zhou *et al.*, in the long-wavelength limit, that spinons can couple to the phonons, like they do with electrons. As a matter of fact, ultrasound attenuation can be measured in order to explore the mass and lifetime of spinons [77].

A new dimer-based organic Mott insulator EtMe$_3$Sb[Pd(dmit)$_2$]$_2$, where 1,3-dithiole-2-thione-4,5-dithiolate is abbreviated to dmit, has been reported recently to show the instability of the quantum spin-liquid as evidenced by thermal conductivity [18], specific heat [78], magnetic susceptibility [79] and NMR [79, 80] measurements. This compound also forms a two-dimensional triangular-lattice structure with antiferromagnetic interaction J = 220-250 K. ^{13}C-NMR measurements down to 19.4 mK for this compound show no splitting of the peak which means no classical ordering or freezing happens [80]. A T-linear contribution has been found in thermal conductivity and specific heat confirming the low-lying gapless excitations which is analogous to the excitations near the Fermi surface in pure metals [18, 78]. Apart from that, a hump-like anomaly shows up in the specific heat measurement at 3.7 K [78] reminiscent to the specific heat measurement in κ-(BEDT-TTF)$_2$Cu$_2$(CN)$_3$ at 6 K, which has to be investigated more carefully. The overall properties of the above-mentioned two spin-liquid compounds have been exten-

sively discussed in recent reviews [22, 81].

4.1 Thermal expansion measurements

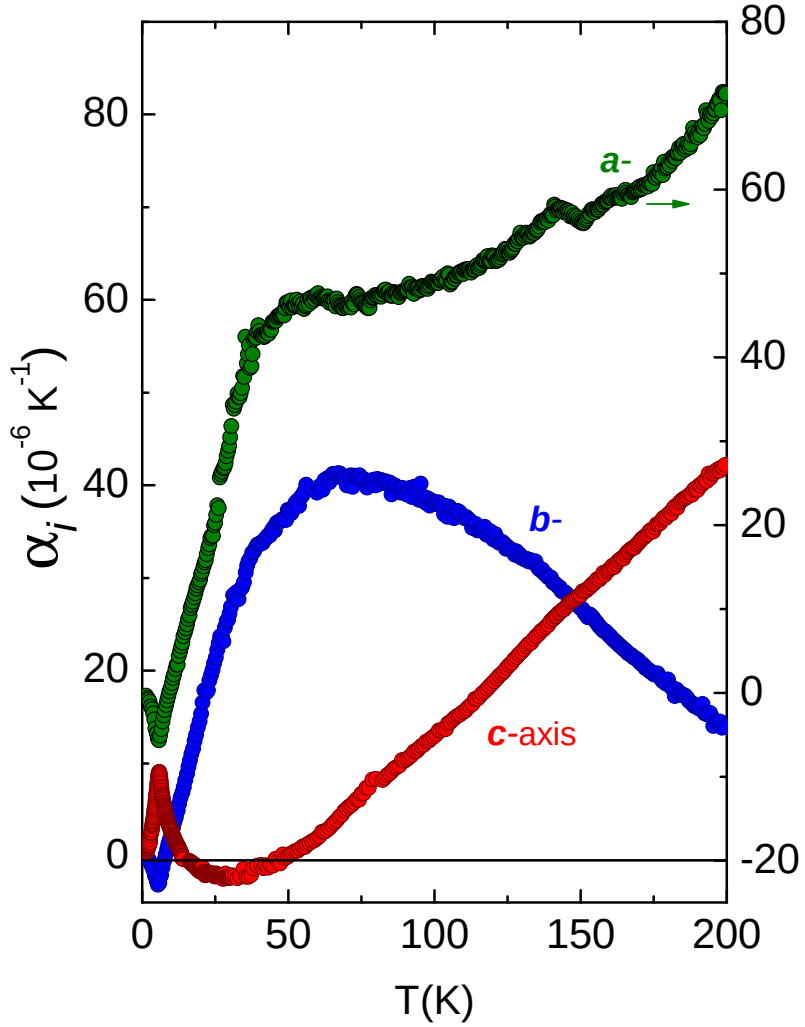

Figure 4.1.1: Uniaxial expansivities α_i of κ-(BEDT-TTF)$_2$Cu$_2$(CN)$_3$ along the in-plane $i = b$ and c axes (left scale) and along the out-of plane $i = a$ axis (right scale). Pronounced in-plane (bc) anisotropy along the b and c-axis predicts a significant distortion of the triangular-lattice. Expansivity along the c-axis was measured by Dr. M. de Souza together with the author of this thesis in the group of Prof. Dr. Michael Lang.

Fig. 4.1.1 shows the uniaxial expansivities along the in-plane $i = b$ and c axes and

along the out-of plane $i = a$[4.1.1] axis. The data along the in-plane b and c axes show a strong anisotropic behavior, both of which deviate markedly from the ordinary lattice expansion. Upon cooling, α_c decreases linearly between temperatures 200 K to 70 K. Then α_c becomes negative at 50 K, followed by a shallow minimum at 30 K. The data along α_b contrast strongly to α_c. α_b starts increasing upon cooling followed by a pronounced shoulder at $T_{max} \simeq 70$ K, which is comparable with the susceptibility data [17]. After that, it decreases rapidly till 30 K. Upon cooling the out-of plane expansivity α_a shows also a pronounced maximum at $T_{max} \simeq 70$ K. The thickness of the sample was very small (~ 0.2 mm)[4.1.2], so the signal-to-noise ratio is low along this axis. The anomalous T-dependence in α_i implies that other excitations contribute to the thermal expansion beside phonons. For example, the negative thermal expansion coefficient along the c-axis, which lacks any clear signature of the material's magnetic properties, may have different origins such as geometrical frustration and/ or quenched disorder [82]. So the in-plane expansivities clearly indicate the T-dependent lattice distortions. This effect is most prominent below 50 K where upon cooling the b-axis lattice parameter strongly contracts (α_b large, positive) while the c-axis lattice parameter expands (α_c negative). As a result, the triangular-lattice will be deformed. Since the inter-dimer hopping integrals t' and t depend on the lattice parameter, so from the data it is concluded that upon cooling in this temperature range t'/t will be increased.

Fig. 4.1.2 shows large and sharp peaks at 6 K along the in-plane (b and c-axes) where the pronounced anisotropy is also observed. It is most strongly pronounced along the c-axis compared to the b-axis. The shape and sharpness of the peaks are strong evidence for a phase transition. No hysteresis has been observed upon cooling and warming with a very slow rate $\pm$ 1.5 K/hour, consistent with a second-order phase transition. The size of this second-order phase transition can be compared with the observations made for one-dimensional (TMTTF)$_2$AsF$_6$ system where spin-Peierls (valence-bond) order has been observed [83]. As the anisotropy of the triangular-lattice at low-temperature is contrary to that of the high-temperature part, *i.e.*, upon cooling around 6 K the c-axis lattice parameter strongly contracts (α_c large, positive) while the b-axis lattice parameter expands (α_b negative), so upon cooling t'/t will be decreased. To confirm the anisotropic deformation of the triangular-lattice as a function of temperature, one has to perform X-ray diffraction measurement as a function of temperature in order to get the temperature variation of the lattice parameter and calculate t'/t accordingly. This will be discussed at the end of this chapter.

Around 3 K, α_c reveals an anomaly which is much smaller in size but reproducible in consecutive runs. The 6 K anomaly is magnetic field-independent up to 8 T (shown

[4.1.1] The out-of plane expansivity has been measured perpendicular to bc plane, *i.e.*, parallel to a^*, α_{a^*} as the crystal structure of κ-(BEDT-TTF)$_2$Cu$_2$(CN)$_3$ is monoclinic with an angle $\beta = 113.42°$ [84]. α_{a^*} is transformed to α_a according to the relation $\alpha_{a^*} = \alpha_a \cos^2(\beta\text{-}90°) + \alpha_c \sin^2(\beta\text{-}90°)$ [1].

[4.1.2] As the dimension of the sample along the out-of plane was 0.1 mm, so in order to have the better signal-to-noise ratio two samples of thickness 0.1 mm each were clapped together with Apiezon grease.

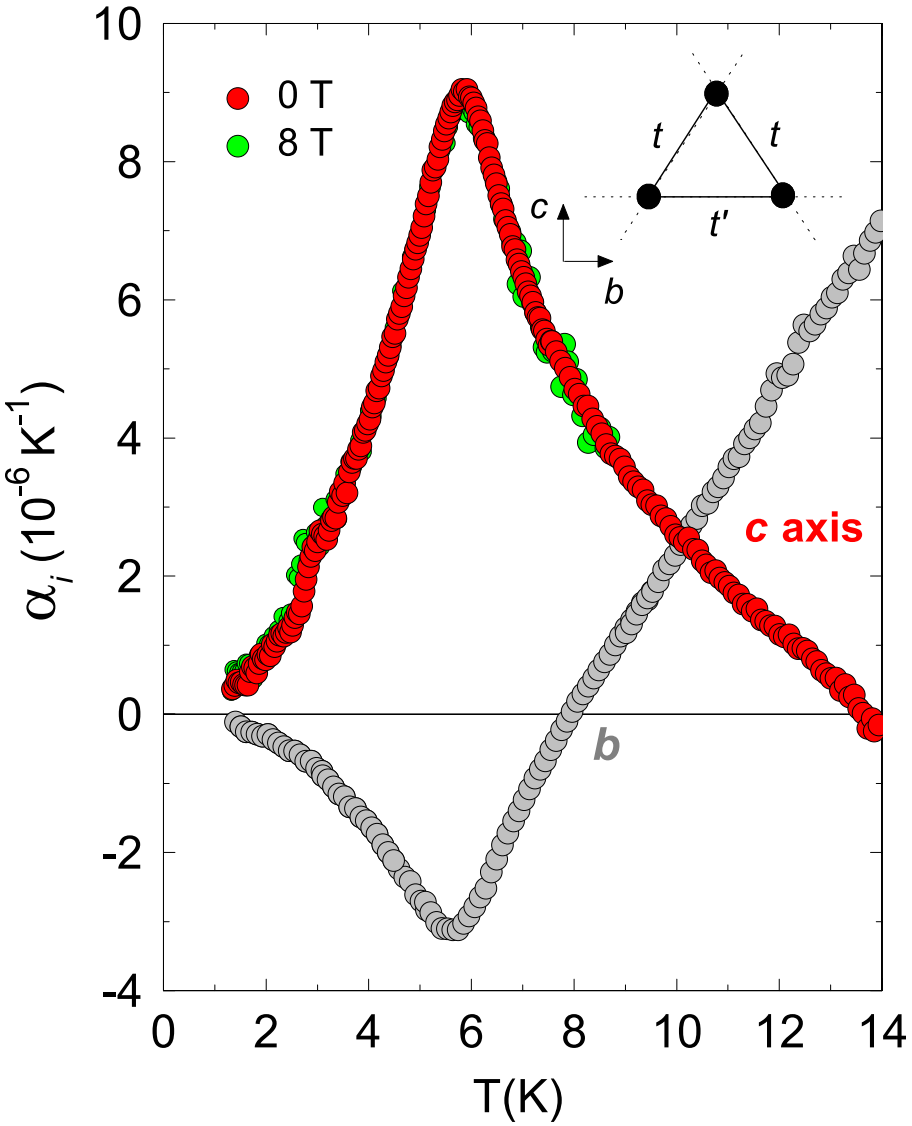

Figure 4.1.2: In-plane (bc) expansivities α_i of κ-(BEDT-TTF)$_2$Cu$_2$(CN)$_3$ on expanded scales around the 6 K phase transition. The data at 8 T of magnetic field along the c-axis coincide with the zero field data. Inset: two-dimensional triangular-lattice dimer-dimer interaction model with hopping integrals t and t'. Expansivity along the c-axis was measured by Dr. M. de Souza together with the author of this thesis in the group of Prof. Dr. Michael Lang.

in Fig. 4.1.2 along the in-plane c-axis), but distinct field dependencies have been found which set in at somewhat higher temperatures for magnetic fields along the b-axis, and will be discussed in the next section. Fig. 4.1.3 shows the volume expansion coefficient $\beta = \alpha_a + \alpha_b + \alpha_c$, where a much less peculiar behavior with a rather smooth variation with temperature is observed. Most interestingly, there is no signature in β at 6 K and T_{max}, rather it shows a small kink at around 5 K and a rounded shoulder near 50 K. The vanishing of an anomaly in β at 6 K implies that, according to the Poisson's effect,

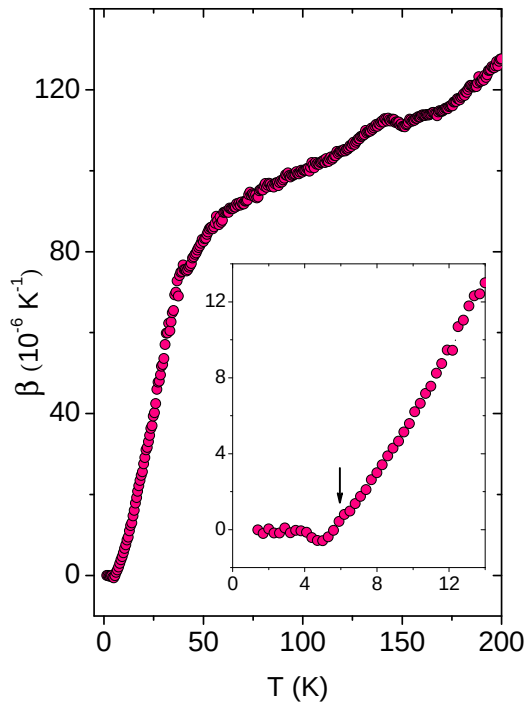

Figure 4.1.3: The temperature dependence of the volume expansion coefficient (β) of κ-(BEDT-TTF)$_2$Cu$_2$(CN)$_3$. Inset: low-temperature variation of β on expanded scale. β lacks any anomaly at 6 K (position of the arrow), rather it shows a small kink at around 5 K.

upon cooling the c-axis lattice parameter contracts (α_c large, positive) while the lattice parameters along b and a-axes expands (α_b and α_a negative) and finally they compensate each other in terms of volume expansion. According to the thermodynamic Ehrenfest relation, a $\Delta\beta = 0$ implies that there is no shift of the $T = 6$ K phase transition under hydrostatic pressure.

$$\left(\frac{\partial T}{\partial P}\right)_{P\to 0} \sim \frac{\Delta\beta}{\Delta C} \approx 0 \tag{4.1.1}$$

This is consistent with the data reported by Prof. Kanoda [85]. The fact that there is a superconducting transition temperature $T_c = 4.5$ K [3] under finite pressure, may suggest some inter-relation between the 6 K phase transition and the superconductivity.

4.2 Entropy calculation from specific heat

Fig. 4.2.1 shows the results of the specific heat on a small single crystal of mass ≤ 100 μg for temperatures 2 K $\leq T \leq$ 10 K. The data reveal a smooth increase as a function

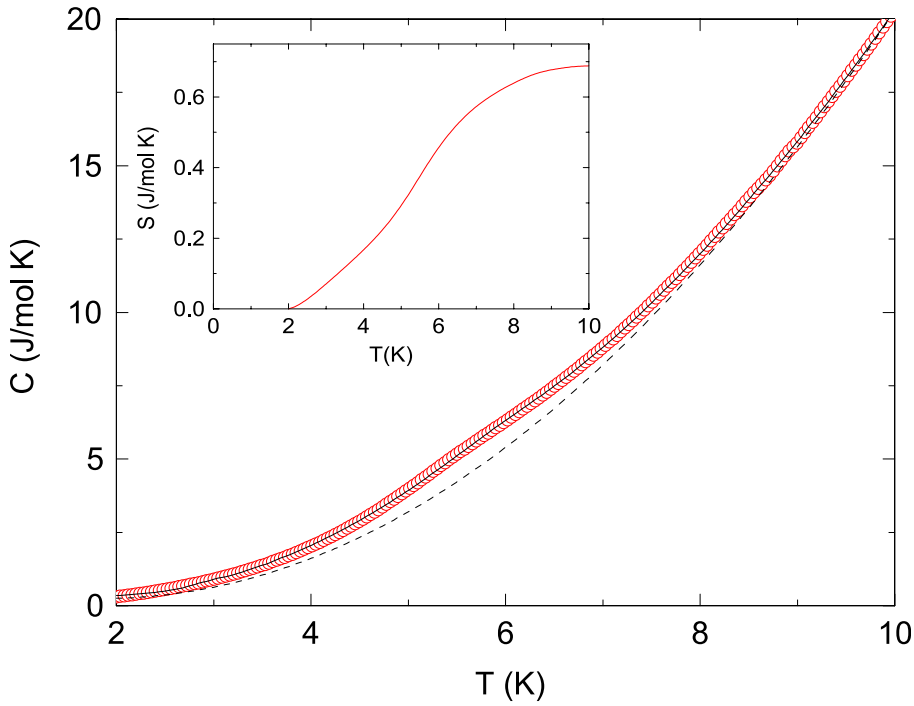

Figure 4.2.1: The specific heat data of κ-(BEDT-TTF)$_2$Cu$_2$(CN)$_3$ between the temperatures 2 K and 10 K. By applying a Grüneisen-scaling Ansatz a fitting function $C_{fit}(T)$ (solid line) has been fitted to the data with a smooth background C^{bg} (broken line). Inset shows the entropy S^{an} release at the phase transition by integrating $\delta C^{an}/T$ from the temperatures 2 K to 10 K. These measurements have been performed by Dr. A. Brühl in the group of Prof. Dr. Michael Lang.

of temperature, followed by a hump-like feature at around 6 K which is consistent with literature results [65]. There is some sample-to-sample dependence observed (not shown here), typical for organic samples. In order to calculate the entropy associated with the phase transition at 6 K, it is important to know the specific heat contribution δC^{trans} precisely involved with it. But it is difficult to estimate the background contribution. Yamashita *et al.* assumed the data of κ-(BEDT-TTF)$_2$Cu(NCS)$_2$ give a phonon background C^{ph} [65]. If the background contribution is only due to the lattice specific heat, then this approach is appropriate. But in the present case, it may also contain some other contributions. In order to take into account all the background contribution, one Ansatz, *viz.*, Grüneisen-scaling is used here. The assumption of this Ansatz is that the contribution of the thermal expansion is proportional to the corresponding contribution of the specific heat provided one relevant energy scale is involved [86]. To apply this Ansatz, it is necessary to know the contribution of the thermal expansion associated with the phase transition at 6 K.

Fig. 4.2.2 shows the phase transition anomalies at 6 K by means of thermal expansion, specific heat and magnetic susceptibility measurements. After subtracting a smooth background from the thermal expansion curves along the in-plane b and c-axes, $\delta\alpha_b^{an}$ and

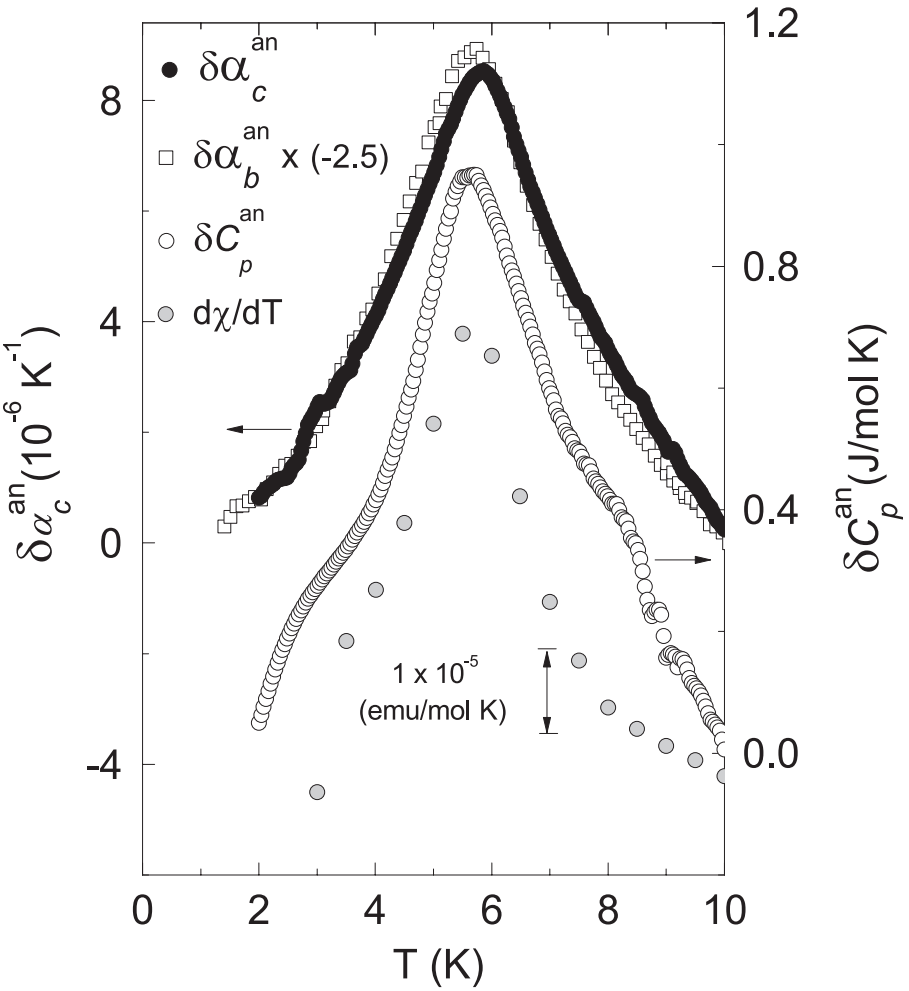

Figure 4.2.2: Phase transition anomalies at 6 K observed by means of thermal expansion, specific heat and the derivative of the magnetic susceptibility. The thermal expansion anomaly along the c-axis is –2.5 times bigger than the anomaly along the b-axis. Different arrows indicate the respective axes and scales. The specific heat was measured by Dr. A. Brühl and expansivity along the c-axis as well as the susceptibility were measured by Dr. M. de Souza together with the author of this thesis in the group of Prof. Dr. Michael Lang.

$\delta\alpha_c^{an}$ are calculated respectively. The anomaly along the c-axis is –2.5 times bigger than the anomaly along the b-axis, cf. Fig. 4.2.2. The magnetic susceptibility[4.2.1] data show a nice agreement with the literature data [17]. Interestingly the derivative of the susceptibility, *i.e.*, $d\chi/dT$ shows also a distinct peak at the phase transition, consistent with the thermal expansion anomalies. Such a transition [87] in the magnetic susceptibility indicates that the spin degrees of freedom are associated with this transition. To calculate the specific heat anomaly δC^{an} at the transition, the Grüneisen-scaling Ansatz

[4.2.1]The magnetic susceptibility measurements have been performed by using a SQUID magnetometer (Quantum Design Magnetic Property Measurement System). A large number of randomly oriented single crystals together of mass 18.0 mg are used to perform this experiment.

is used in the temperature range 2 K $\leq T \leq$ 10 K, discussed above. As the thermal expansion anomaly along the c-axis is larger compared to the other in-plane b-axis, the background does not influence the resulting $\delta\alpha_c^{an}$ much. With the help of the function below, a least-squares fit to the specific heat has been performed.

$$C_{fit}(T) = \delta C^{an} + C^{bg} = \frac{1}{\gamma_c}\delta\alpha_c^{an} + C^{bg} \tag{4.2.1}$$

where γ_c is a generalized Grüneisen parameter [86]. A second-order polynomial was used for C^{bg}, $C^{bg} = a_0 + a_1 T + a_2 T^2$. $C_{fit}(T)$ fits nicely to the experimental specific heat data and the broken line shows a smooth background, cf. Fig. 4.2.1. The resulting $\delta C^{an} = C_{fit}(T)$ - C^{bg} shows a sharp anomaly at 6 K, similar in shape as the feature in α and $d\chi/dT$, cf. Fig. 4.2.2.

The inset of Fig. 4.2.1 shows the entropy S^{an} release at the phase transition by integrating $\delta C^{an}/T$ from the temperatures 2 K up to 10 K. The value of the entropy is (0.69 ± 0.05) J mole^{-1} K^{-1} taking into consideration that one mole substance contains $2{\cdot}N_A$ dimers (spins), where N_A denotes Avogadro's constant. For a hypothetical system containing N_A spins with $S = 1/2$, the value of the full spin entropy is Rln2, where $R = 8.314$ J mole^{-1} K^{-1}, the universal gas constant. The calculated entropy S^{an} associated with the transition is about (6 ± 0.4)% of the system's full spin entropy. This entropy value can be compared to available theoretical spin models. The two-dimensional triangular-lattice $S = 1/2$ model would be an ideal model to compare this magnetic entropy, but this is only available for the isotropic triangular-lattice where $t = t'$. Bernu *et al.* developed a method to determine the specific heat of the lattice spin systems, based on the high-temperature series expansions, the system's total entropy and the expected low-temperature behavior of the specific heat [88]. Based on this model, the entropy can be calculated for a pure Heisenberg antiferromagnet. The value of the entropy is (2.3 ± 0.1)% of Rln2 for $J/k_B = 250$ K and temperature $T \leq 10$ K. One can take into account the ring exchange process which is likely to be significant near the Mott transition. Then the value of the entropy release at the phase transition will be higher. Motrunich *et al.* studied the triangular-lattice spin-1/2 system with antiferromagnetic Heisenberg and ring exchanges by using a variational approach and which they then applied to the realization of the spin-liquid state in κ-(BEDT-TTF)$_2$Cu$_2$(CN)$_3$ [89]. It was found that the ring exchanges destabilize the antiferromagnetic ordered state in favor of a fermionic spin-liquid state. This spin-liquid state is characterized by the spinon Fermi surface. One could calculate the specific heat associated with it which is $C_{spinon} = \gamma_{spinon}{\cdot}T$, where $\gamma_{spinon} = (\pi^2/3)k_B^2 N_A n(E_F)$. The density of states at the "Fermi surface" $n(E_F)$ in the spinon band structure is determined by the spinon "hopping amplitude" t_{spinon} and this value is set to the Heisenberg exchange energy $t_{spinon} \sim J$. For a half-filled triangular-lattice, the density of states at the "Fermi surface" is $n(E_F) = 0.28/t_{spinon}$ per triangular-lattice site, including its spin. By taking into consideration all the above points, the value of γ_{spinon} has been calculated which is $\gamma_{spinon} = 30$ mJ mole^{-1}K^{-2} and the remaining spinon

entropy of 5.2% of Rln2 for $T \leq 10$ K.

Grover *et al.* studied the energetics of Gutzwiller-projected BCS states of various symmetries for the triangular-lattice antiferromagnet with a four-particle ring exchange, using variational Monte Carlo methods and applied this method to the experimentally measured specific heat data which was found to be consistent. It is also predicted from this model how the behavior will be of the specific heat as a function of temperature in the case of mean-field-type and gauge fluctuation, which is beyond a mean-field type [75]. However, by estimating possible errors, there is a significant mismatch between the residual spinon entropy S^{spinon} and the experimental calculated entropy across the transition S^{an}. The reason for this is mainly due to the peculiar non-mean-field shape of the experimentally observed transition, which required a truncation of the high- and low-temperature flanks in δC^{an}. The error associated with the value of S^{trans}/S^{an} is probably in the range 1.2–1.4. In addition, for an anisotropic triangular-lattice system ($t' < t$) which is the case for this compound, the value of the entropy will be further reduced compared to the calculated value. As a matter of fact, the available spin entropy (5.2% of Rln2) calculated from the theoretical models is significantly lower than the experimentally determined entropy release at the phase transition S^{trans} (7–8% of Rln2). This result reflects that the spin degrees of freedom alone are insufficient to account for the phase transition at 6 K [33, 90]. A good guess for this discrepancy would be the action of charge degrees of freedom. In fact, it is theoretically predicated by Qi *et al.* that due to the formation of neutral charge pairs of charge +e and -e fermions, an excitonic condensation can form near a Z_2 spin-liquid of bosonic spinons, breaking the lattice space group symmetry [24]. Objections against this scenario may be derived from the absence of clear signatures for a charge modulation below 6 K in ^{13}C-NMR studies. The lack of evidence there, however, might be due to the anomalous inhomogeneous broadening of the NMR spectra [72, 91], which may have obscured a potential line splitting.

Optical conductivity measurements show that the charge gap in this material is strongly suppressed indicating the material's close proximity to the insulator-metal transition [92]. Alternatively, one might consider charge fluctuations at elevated temperatures, giving rise to fluctuating electrical dipoles. Recent dielectric measurements show that relaxor-like dielectric relaxation behavior occurs below around 60 K, predicting the randomly oriented electric dipoles. Due to the collective motion of the electric dipoles, dielectric relaxation is observed. There is no clear phase transition observed in this experiment, but the dielectric displacement D indicates that somehow the electric dipoles order at 6 K in an antiferromagnetic nature [93]. In order to explain this phenomenon, quantum electric dipoles on dimers are considered as a model where within the BEDT-TTF dimers, charge disproportionation happens, driven by the intermolecular Coulomb interaction V [94, 95]. The paired-electron crystal (PEC) scenario, consisting of charge-rich sites separated by pairs of charge-poor sites, demonstrates the coexistence of charge order and spin gap in a two-dimensional quarter-filled band on an anisotropic triangular-lattice [96, 97, 98].

Due to the ionic nature of the material, ordering phenomena in the charge sector are expected to give rise to distinct lattice effects as, *e.g.*, demonstrated for the charge-ordering transition in related materials [83, 99]. Since the charge distribution also affects the magnetic exchange constants, a response in the magnetic susceptibility is expected as well.

4.3 Magnetic field dependency in κ-(BEDT-TTF)$_2$Cu$_2$(CN)$_3$

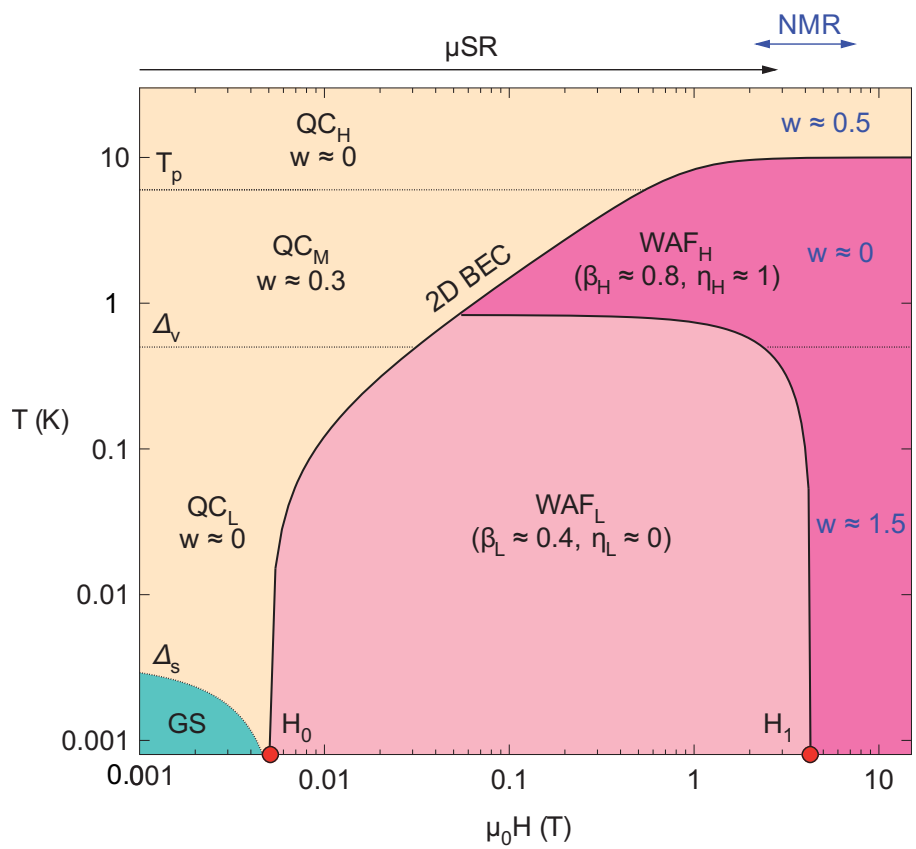

Figure 4.3.1: Magnetic phase diagram of κ-(BEDT-TTF)$_2$Cu$_2$(CN)$_3$ based on μSR and NMR measurements for different magnetic field ranges (adapted from ref. [101]). Different phases (QC: quantum critical, WAF: weak-moment antiferromagnetic) of the phase diagram are defined based on their characteristic critical parameters β, η and w as a function of T or H (L: low, M: intermediate, H: high). Gapped spin-liquid (GS) regime also found for $T < \Delta_s(H) = 3.5$ mK. $H_0 = 5$ mT and $H_1 = 4$ T are the two quantum critical points.

A quantum spin-liquid (QSL) is a quantum mechanical ground state in which there is no long-range magnetic order ($LRMO$) and no breaking of spatial (rotational or translation) symmetries even at $T = 0$ K. Geometrical frustration plays an important role in

order to form the spin-liquid ground state. Previously, NMR measurements have been performed at low temperatures under external fields. It was concluded from these measurements that the phenomenon is related to inhomogeneous staggered moments which could be related to impurities and other defects embedded in an underlying spin-liquid [72]. Thermal conductivity measurements also show the magnetic field dependency of the low-temperature state of this compound. There is a parallel shift between the κ/T vs T^2 curves for 0 T and 10 T in the low-temperature regime ($T < 300$ mK). Such an enhancement of the thermal conductivity value by the application of a magnetic field is related to a magnetic contribution κ_{mag} to κ even at low-temperature [68]. This enhancement of the thermal conductivity at low-temperature has been suggested in terms of closing the gap for magnetic excitations [100]. Recently, by performing μSR experiments at a small magnetic field, κ-(BEDT-TTF)$_2$Cu$_2$(CN)$_3$ was found to show a quantum phase transition (QPT) between the spin-liquid phase and an antiferromagnetic phase with a strongly suppressed moment which can be explained as Bose-Einstein condensation of spin excitations with an extremely small gap ($\Delta_s(H) = 3.5$ mK). As the moment of the muon is much larger than that of nuclear spins, it was possible to measure the μSR at much lower field than that of NMR measurements. Fig. 4.3.1 shows the magnetic phase diagram of κ-(BEDT-TTF)$_2$Cu$_2$(CN)$_3$ based on these μSR and NMR measurements for different magnetic field ranges. Different magnetic phases are found like a quantum critical (QC) and a weak-moment antiferromagnetic (WAF) phase based on their characteristic critical parameters β, η and w as a function of T or H (L: low, M: intermediate, H: high). Two quantum critical points, namely, at H_0 (5 mT) and at H_1 (4 T) are observed with well-separated field values. The 6 K anomaly was explained as the result of a fraction of fermionic spins forming bosonic pairs at this temperature [101]. There are some theoretical proposals based on these field-induced phenomena regarding Mott insulators where the antiferromagnetic ordering is due to the orbital electric currents. So the spin currents and the external magnetic field are coupled to each other [102, 103, 104]. Very recently, field-induced freezing of a quantum spin-liquid on the Kagome lattice has been discovered by means of ^{17}O-NMR measurements for the compound ZnCu$_3$(OH)$_6$Cl$_2$. A similar kind of T-H phase diagram has been observed compared to κ-(BEDT-TTF)$_2$Cu$_2$(CN)$_3$, but showing only one quantum critical point at a small magnetic field $\mu_0 H_c = 1.55$ T. This phenomenon has been explained in terms of a perturbing Dzyaloshinskii-Moriya interaction which was theoretically proposed to sustain a quantum critical regime for the quantum Kagome Heisenberg antiferromagnet model [105].

4.3.1 Field-induced effect in thermal expansion

Whereas the 6 K phase transition is insensitive to the magnetic field up to 10 T, the highest field accessible, distinct field dependencies [106] have been found which set in at somewhat higher temperatures for magnetic fields along the in-plane b-axis of high-quality crystals. Fig. 4.3.2 shows the relative length changes $\Delta l_b(T)/l_b = [l(T)\text{-}l(T_0)]/l(T_0)$, with $l(T_0) = 300$ K, as a function of temperature at different magnetic fields along the

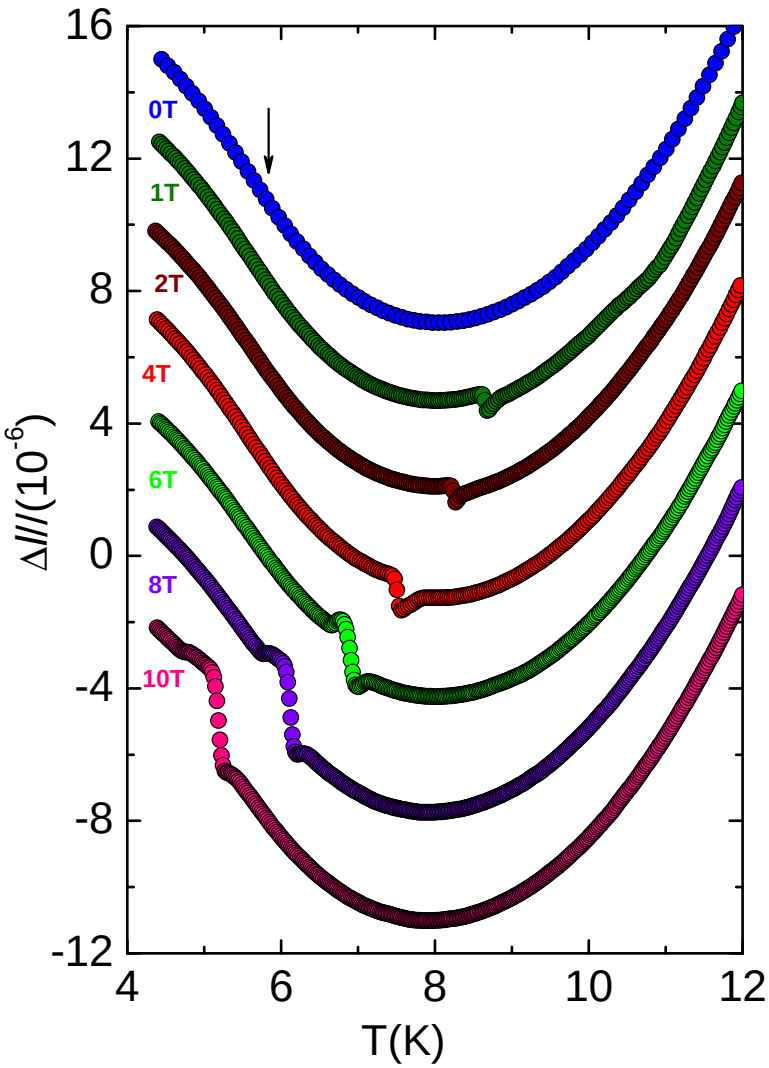

Figure 4.3.2: Magnetic field dependence along the b-axis in terms of relative length changes for a particular high-quality sample (batch - KAF 5078#1). The various curves have been shifted along the y-axis for clarity. The arrow indicates the anomaly at 6 K, giving rise to a peak in α, which is insensitive to the magnetic field.

specified direction. The magnetic field is applied parallel to the b-axis. The data set have been shifted along the y-axis to display the effect clearly. For fields $B \geq 1$ T, the data reveal a jump-like anomaly which grows in size and shifts to lower temperatures with increasing the fields. The effect does not depend on whether the system is field cooled (FC) or zero-field cooled (ZFC), *i.e.*, the position of the magnetic field-induced anomaly does not depend on whether the system is FC or ZFC, but the size of the

anomaly slightly reduces if one applies the field near to the phase transition temperature $T = 6$ K. So in order to get the maximum effect, the field was applied at $T = 12$ K. The results at zero field show a broad minimum centered around 8 K, corresponding to a change of sign along the b-axis thermal expansion coefficient $\alpha_b = l_b^{-1}\partial l_b/\partial T$, cf. Fig. 4.1.2. The arrow in the figure indicates that the abrupt change in the slope in $\Delta l_b(T)/l_b$, giving rise to a sharp minimum in α_b where the 6 K phase transition happens, cf. Fig. 4.1.2. One needs at least 1 T magnetic field to observe the jump-like feature at 8.7 K. A peculiarity of this B-induced anomaly is the undershoot (overshoot) behavior on the high (low)-temperature side of the discontinuity.

There is no such discontinuity in the length change at low-temperature in the case of zero magnetic field and 0.5 T (not shown here), suggesting that a finite magnetic field is required in order to observe this effect. So the critical field would be 0.5 T $< B_c <$ 1 T.

Fig. 4.3.3 shows the relative length changes as a function of temperature at a constant magnetic field of 8 T upon cooling and warming with a small rate of $\pm$ 1.5 K/hour. There was no hysteresis observed within this temperature range. Generally an abrupt change in length is a signature of a first-order transition. In the case of a first-order transition, however, one would expect a hysteresis upon warming and cooling and different slopes in $\Delta l_b/l_b$, implying different thermal expansion coefficients α_b, above and below the transition. Ref. [2] shows the example of a first-order phase transition in the case of a Mott transition by performing thermal expansion measurements for the deuterated κ-(ET)$_2$Cu[N(CN)$_2$]Br compound. So the observations are against the interpretation in terms of a first-order phase transition. However, a higher warming and cooling rate do not effect the anomaly which is an indication that there is no spin glass-like behavior.

Fig. 4.3.4 shows the plot of the $\Delta l_b/l_b$ data at $B = 0$ and 10 T from Fig. 4.3.2 without employing a vertical shift. The arrow indicates the position of the break in the slope of the zero-field data, corresponding to a second-order phase transition anomaly in the coefficient of thermal expansion, at around 6 K. The 6 K transition is virtually unchanged also in the data taken at 10 T. Interestingly, the data collapse both at the high- and low-T end, but deviate from each other at intermediate temperatures. This demonstrates that the total change of the b-axis lattice parameter upon cooling from 12 K down to 4.5 K is virtually unaffected by the presence of a magnetic field of 10 T. The same observation holds true, within the uncertainty of the experiment, for all other $B =$ constant curves in Fig. 4.3.2 (not shown here). Apparently, the gradual growing departure of the $B =$ const. data from the zero-field curve upon cooling, *i.e.*, an additional B-induced lattice strain, is released by the jump-like anomaly.

In order to map out the position of the B-induced anomaly in the temperature-field plane, magnetostriction measurements at varying constant temperatures have been carried out. Fig. 4.3.5 shows the length changes as a function of magnetic field at a particular

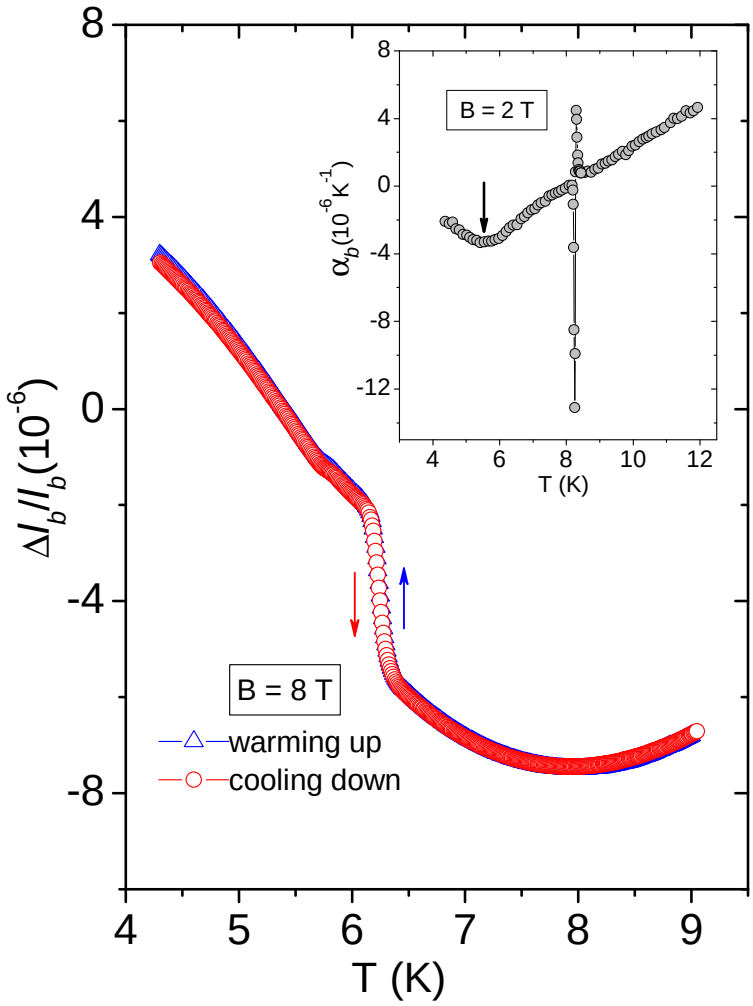

Figure 4.3.3: Relative length changes as a function of temperature measured at a very slow rate of $\pm$ 1.5 K/hour for the magnetic field $B = 8$ T. Inset: thermal expansion coefficient as a function of temperature under a magnetic field of 2 T to show that the 6 K phase transition anomaly is not effected by the application of magnetic field. The arrow indicates the position of the 6 K phase transition.

temperature $T = 6$ K. In these magnetostriction measurements,[4.3.1] another anomaly has been found at lower field together with the anomaly which was observed as a function of temperature at different constant field values. The sweep rate of the magnetic field was $\pm$ 120 mT/min[4.3.2]. The oscillations in the curve are due to the quantum oscillations of gallium (Ga). This is unavoidable because Ga is necessary for affixing the sample in

[4.3.1] Cell effect was not subtracted as the magnetic field was varying, but the field effect was so pronounced to detect the anomalies.

[4.3.2] Other field sweep rates are also used, but the effects were independent on the field sweep rates.

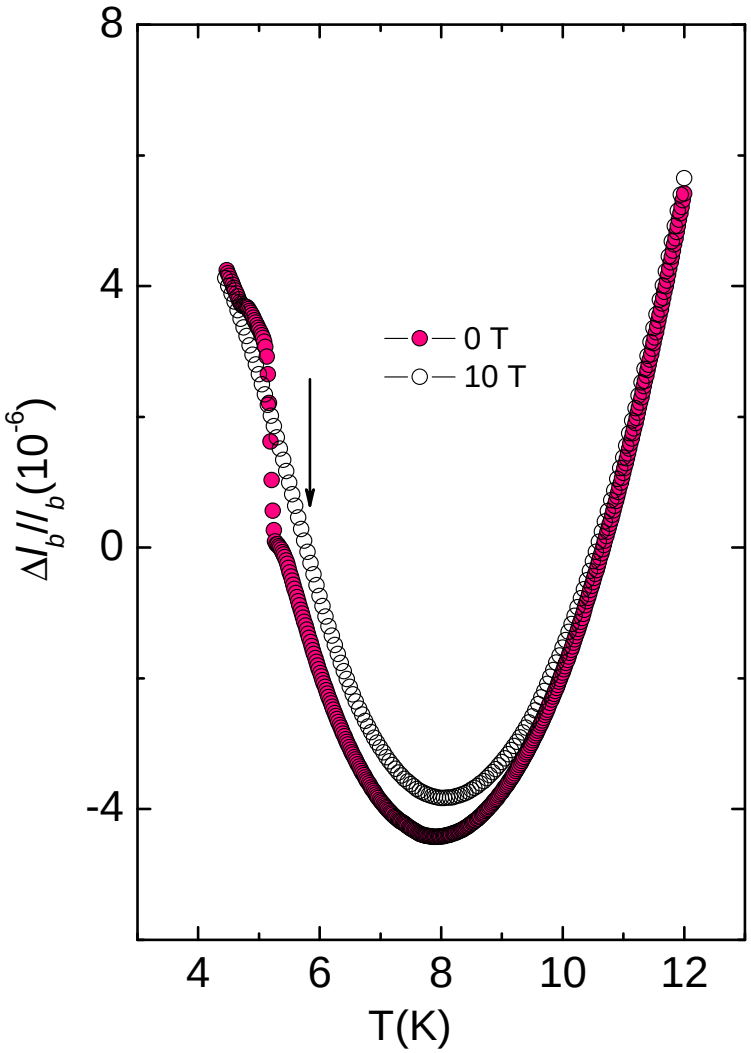

Figure 4.3.4: Plot of the $\Delta l_b/l_b$ data at $B = 0$ and 10 T from Fig. 4.3.2 without employing a vertical shift. The arrow indicates the position of the break in the slope of the zero-field data, corresponding to a second-order phase transition anomaly in the coefficient of thermal expansion, at around 6 K. The 6 K transition is virtually unchanged also in the data taken at 10 T.

a preferred direction. Based on the measurements as a function of temperature at constant field and isothermal field sweeps, an anomaly diagram was able to be constructed, shown in Fig. 4.3.6[4.3.3]. From the anomaly diagram it is clear that the magnetostriction

[4.3.3]The anomalies are shifted after the next cool down, but the anomaly diagram looks similar with some parallel shift of the curves (not shown here). Since the cooling rate was not equal for both the cool down process from room temperature, the reason for the shifting of the peaks position could be due to

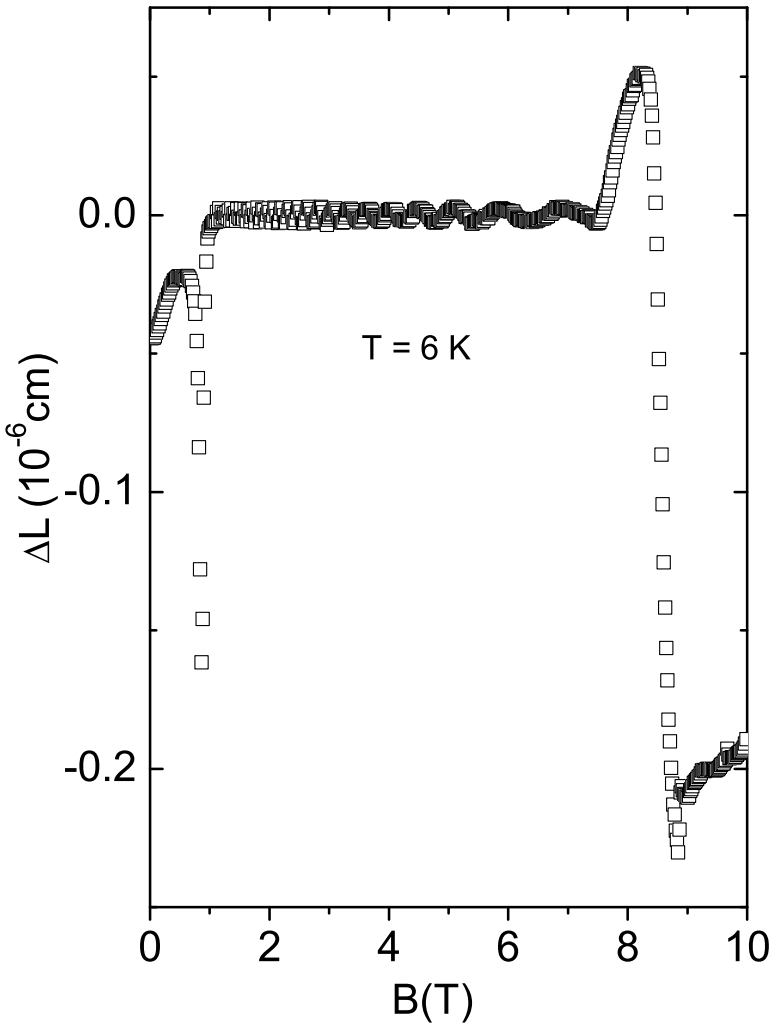

Figure 4.3.5: Magnetostriction measurements, *i.e.*, length changes as a function of magnetic field at the temperature $T = 6$ K. Two pronounced anomalies are observed at well-separated field values. The anomaly at the higher field is also observed for temperature sweeps while the magnetic field is kept constant. But the lower-field anomaly, found only in magnetostriction measurements, is sharp and step-like.

measurements are consistent with the measurements of the temperature-dependence at constant magnetic field values. Two distinct magnetic field-induced features have been found which are most strongly pronounced and well-separated at low temperatures, while the anomalies merge together at around 8.4 K.

the history dependency.

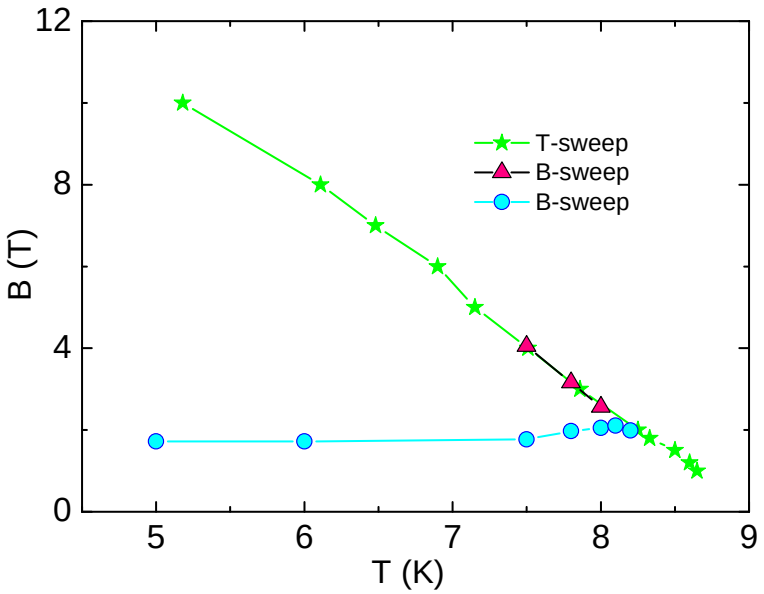

Figure 4.3.6: Position of the B-induced anomalies in $\Delta l_b/l_b$ for B applied parallel to the b-axis as determined from measurements as a function of T at B = const. and as a function of B at T = const.

The temperature-field phase diagram obtained from μSR measurements [101] has been modified by including the positions of the anomalies in the thermal expansion data, shown in Fig. 4.3.7. One of these anomalies lies close to the phase boundary between a quantum critical (QC_H) and a weak antiferromagnetic (WAF_H) phases. But there is no indication of the other anomaly at lower fields, obtained only from magnetostriction measurements. It is important to note that the magnetic field-induced effect in the thermal expansion is obtained only along the in-plane b-axis ($B \parallel b$) while there is no such field effect observed for fields aligned along the in-plane c- [33] and out-of plane a-axes (not shown here). Here it is important to note that μSR measurements have been performed on a polycrystalline sample with a mass of 70 mg which was made up of a mosaic of many small crystals [101]. This magnetic field effect is reminiscent of "flux-pinning-related" effects. The pinning effect could be related to some molecular defects, dislocations, grain boundaries, or twinning planes [8]. If this holds true, then one should expect to see some hysteresis across the anomaly upon warming and cooling, but unfortunately this is not the case. Alternatively, one might think of field-induced orbital motions of the electrons which may affect the hopping amplitudes, and by this, the exchange coupling constants. In addition, on the basis of the present data, the question of whether or not the B-induced anomaly manifests a phase transition cannot be definitely answered. It needs a microscopic model to explain this effect.

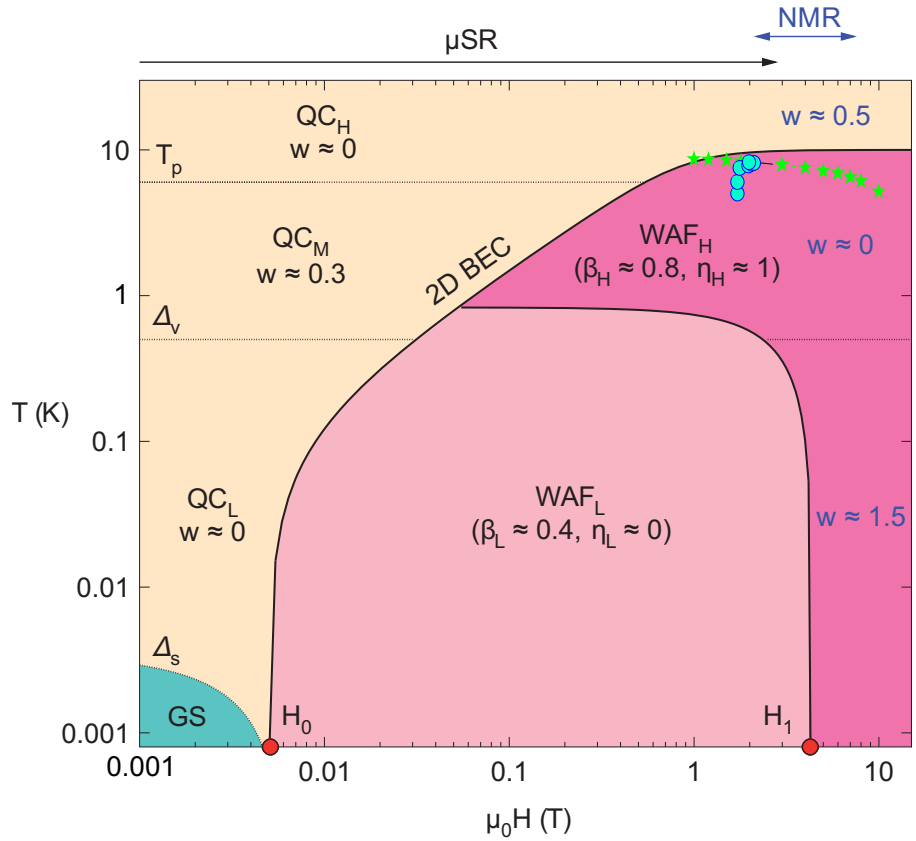

Figure 4.3.7: Modified version of the phase diagram, reported by the ref. [101] by including the positions of the anomalies obtained from the thermal expansion and magnetostriction measurements. Green stars lie close to the phase boundary between quantum critical (QC_H) and weak antiferromagnetic (WAF_H) phases.

There is some sample-to-sample dependence observed in this compound measured along the b-axis, shown in Fig. 4.3.8. The magnetic field-induced anomaly is observed for the samples KAF5078#1 and KAF5078#4 where the 6 K phase transition is bigger compared to the effect seen in samples KAF5078#2 and KAF5078#3. This suggests that the size of the 6 K anomaly at $B = 0$ T is related to the magnetic field dependency, *i.e.*, when the 6 K anomaly is bigger in size, the magnetic field dependency is more pronounced.

4.4 Temperature dependence of structural and electronic properties

Structural and electronic properties of κ-(BEDT-TTF)$_2$Cu$_2$(CN)$_3$ change significantly as a function of temperature. The crystal structure of this compound for their κ and κ'

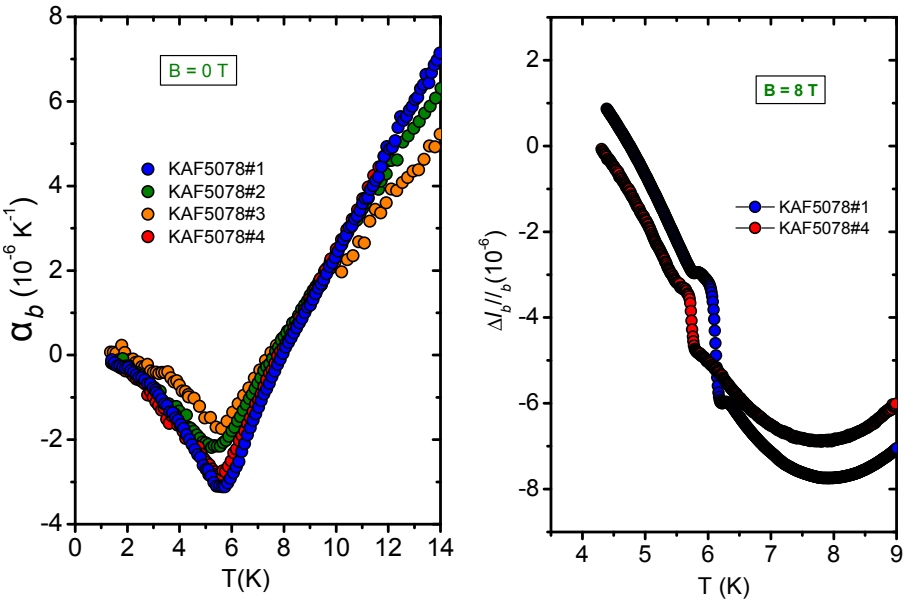

Figure 4.3.8: Left panel: sample-to-sample dependence of α_b for κ-(BEDT-TTF)$_2$Cu$_2$(CN)$_3$ around the $T = 6$ K phase transition at $B = 0$ T. Right panel: comparison of the relative length changes as a function of temperature under magnetic field 8 T for two different samples. Samples KAF5078#1 and KAF5078#4 show magnetic field dependency near the 6 K phase transition. Samples (KAF5078#1 and KAF5078#4) which show the bigger anomaly at 6 K, show the magnetic field dependency.

	300 K	**250 K**	**200 K**	**150 K**	**100 K**	**20 K**	**5 K**
a (Å)	16.0919(3)	16.0848(3)	16.0781(3)	16.0703(3)	16.0746(6)	16.072(4)	16.062(3)
b (Å)	8.5722(2)	8.5749(1)	8.5737(1)	8.5664(2)	8.5593(3)	8.536(2)	8.544(2)
c (Å)	13.3889(2)	13.3373(2)	13.2964(2)	13.2698(3)	13.2678(5)	13.262(3)	13.271(2)
β (°)	113.406(1)	113.853(1)	114.273(1)	114.609(1)	114.852(1)	115.088(3)	115.093(2)
V (Å^3)	1694.93(6)	1682.43(4)	1670.86(4)	1660.72(6)	1656.51(1)	1647.8(6)	1649.3(5)

Table 4.1: Crystal structure data of κ-(BEDT-TTF)$_2$Cu$_2$(CN)$_3$ for the temperatures 5, 20, 100, 150, 200, 250 and 300 K by performing single crystal X-ray diffraction measurements (adapted from ref. [114]).

phases has reported several times in the literature at room temperature [84, 107, 108, 109, 110, 111, 112]. Later on, the lattice parameters were available for 300 K and 30 K [113], but not for the whole temperature range. In order to see how the structure of this material changes as a function of temperature, single crystal X-ray diffraction technique is used. Full data set for the structural analysis were collected at temperatures of 5, 20, 100, 150, 200, 250 and 300 K [114]. All the crystal structure data for the mentioned temperatures are shown in Table 4.1.

Fig. 4.4.1 shows the relative lattice parameters normalized by their values at $T =$ 20 K along the three crystallographic axes as a function of temperature as derived from

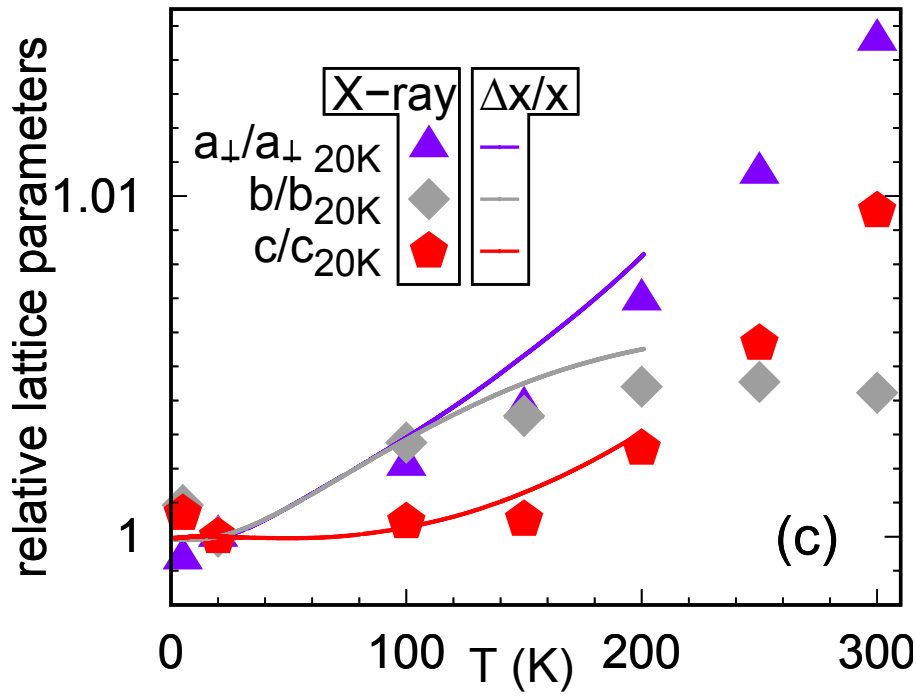

Figure 4.4.1: Relative lattice parameters normalized to their values at $T = 20$ K, as a function of temperature (adapted from ref. [114]). Single crystal X-ray diffraction data are shown in symbols while the solid lines (relative length changes) are obtained from thermal expansion measurements. Single crystal X-ray diffraction measurements were performed by Dr. J. A. Schlueter and Dr. M. de Souza.

single crystal diffraction experiments [114]. The data is in good agreement with the temperature dependent relative length changes determined by thermal expansion measurements. In fact, the derivative of these relative length changes gives the thermal expansion coefficients already shown in Fig. 4.1.1.

Based on the crystal structures at different temperatures, the evolution of the electronic properties have been simulated by using density functional theory and tight-binding methods. Fig. 4.4.2 shows how the nearest-neighbor transfer integrals t and t' (see Fig. 4.0.5 for details) and the interaction strength (U/t) in an anisotropic triangular-lattice change as a function of temperature. The value of t increases upon cooling, then shows a hump at round 200 K and finally decreases at lower temperature. The reversed behavior is found for t' upon cooling. Interestingly, t'/t which determines the degree of frustration in an anisotropic triangular-lattice shows a hump-like anomaly at around 150 K. Even though the change in t'/t is not so much from room temperature down to 5 K in terms of their absolute values, there is a significant change in the value at around 150 K. The Coulomb interaction strength (U) is defined as $U \approx 2t_1$, where t_1 is the intradimer hopping integral. The interaction strength (U/t) increases monotonically upon cooling from room temperature.

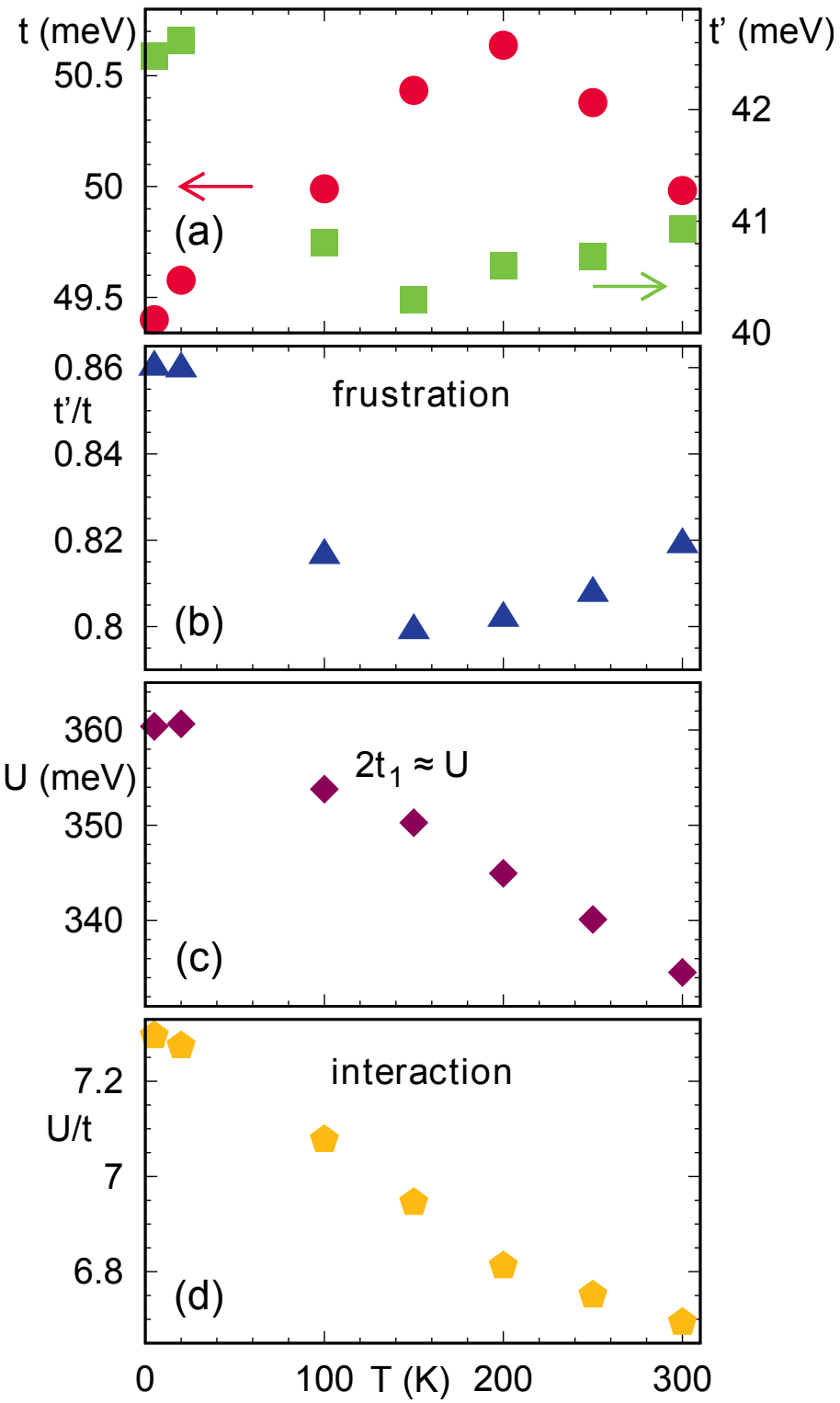

Figure 4.4.2: Temperature dependence of nearest-neighbor hopping integrals (t and t') and interaction strength (U/t) (adapted from ref. [114]). Calcuations were performed by Dr. H. O. Jeschke and Prof. Dr. R. Valentí.

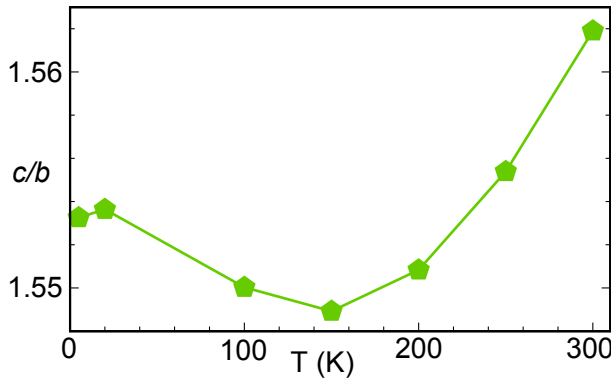

Figure 4.4.3: Ratio of the in-plane c and b lattice vectors as a function of temperature (adapted from ref. [114]). Single crystal X-ray diffraction measurements were performed by Dr. J. A. Schlueter and Dr. M. de Souza.

Fig. 4.4.3 shows the ratio between the in-plane c and b lattice vectors as a function of temperature. From the triangular-lattice arrangement, b effects the t' whereas c has an effect on t, cf. Fig. 4.0.5. So the ratio of c/b has an influence on the ratio t'/t. Interestingly, the c/b ratio shows also a hump at around 150 K. An anomaly around this temperature has also been observed in ^{1}H-NMR relaxation rate [3] and thermopower [4] measurements. The ordering of the ethylene groups could be the reason for this anomaly. From the data analysis, it is found that the ordering of ethylene groups in a staggered configuration gradually increases from room temperature (77%) to 200 K (93%) and fully order below 150 K. As the measurement steps were of the order of 50 K, it was difficult to estimate the exact ordering temperature. Thermal expansion measurement along the out-of plane a-axis (cf. Fig. 4.1.1) also shows a step-like anomaly at around 150 K. This is consistent with the observations made in ^{1}H-NMR measurements yielding a strong contribution from thermally activated vibrations of the ethylene group which vanishes below 150 K [3]. As the thermopower is the energy derivative of the density of states at the Fermi level [115], the temperature dependence of t'/t could be related to the drastic change in the thermopower at around 150 K.

5

Azurite – $Cu_3(CO_3)_2(OH)_2$

The natural mineral azurite, $Cu_3(CO_3)_2(OH)_2$, was used in ancient days as a pigment because of its deep blue color. In the last couple of years, this material was also quite popular from physics point of view because it has been proposed as an experimental realization of quasi-one-dimensional distorted diamond-chain. In this material, Cu^{2+} ions form a triangular-lattice arrangement via O^{2-} ions along the chain direction, *i.e.*, the crystallographic b-axis. The spins are arranged in an antiferromagnetic fashion in a triangular-lattice, causing frustration [116]. The crystal structure of azurite is monoclinic with a space group $P2_1/c$ and the lattice parameters $a = 5.01$ Å, $b = 5.85$ Å, $c = 10.35$ Å, $\beta = 92.43°$ and $z = 2$ [117, 118].

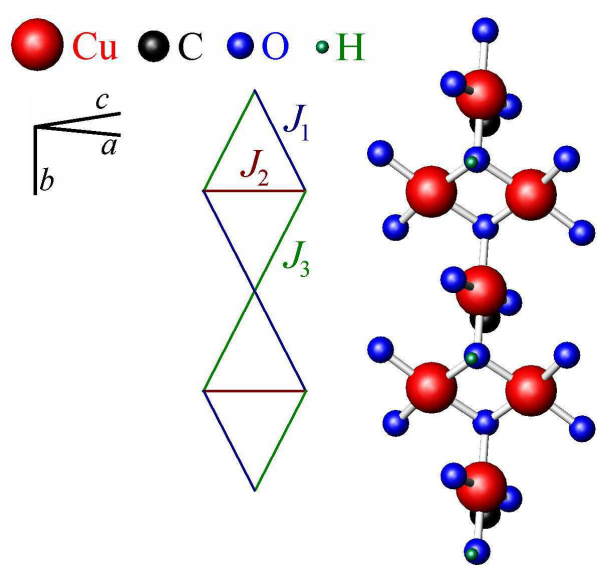

Figure 5.0.1: Chemical structure of azurite together with the exchange interactions (J_1, J_2 and J_3) based on the distorted diamond-chain model (adapted from ref. [119]). Different atoms are shown in different colors.

Fig. 5.0.1 shows the crystal structure of azurite. The microscopic model, which can explain the main properties of azurite at low-temperature, is the monomer-dimer model, *i.e.*, monomer spins $S = 1/2$ are separated by the $S_{dimer} = 0$ dimers on the diamond-chain backbone. The exchange coupling between the spins are denoted by J_1, J_2 and J_3. The magnetic properties of the distorted diamond-chain calculated at $T = 0$ K imply that there are different phases which can be obtained, depending on their J values, namely, ferrimagnetic phase, the spin-fluid (SF) state and the dimerized phase [27, 28]. Fig. 5.0.2 shows the different phases of the distorted diamond-chain model and Fig. 5.0.3 shows the corresponding phase diagram in the $\tilde{J}_2$-$\tilde{J}_3$ plane, where $\tilde{J}_2 \equiv J_2/J_1$ and $\tilde{J}_3 \equiv J_3/J_1$.

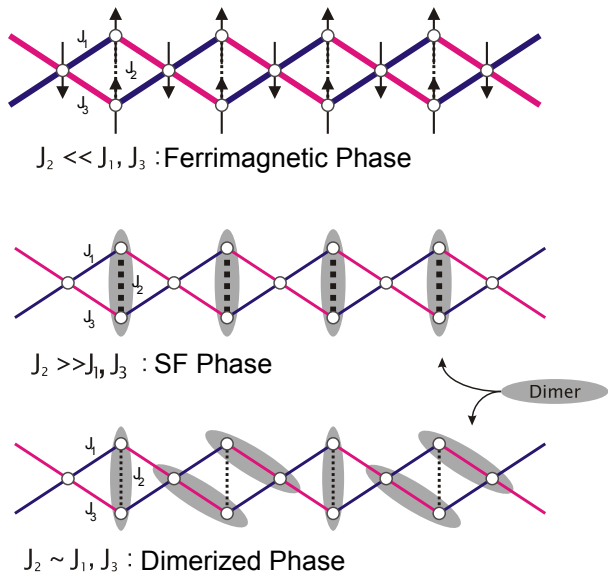

Figure 5.0.2: Ground states of the $S = 1/2$ distorted diamond-chain model consisting of ferrimagnetic phase, the spin-fluid (SF) state and the dimerized phase. The shadowed ellipse consists of two spins to form a dimer [27] (adapted from ref. [120]).

Many experiments have been performed on the $S = 1/2$ diamond-chain quantum magnet azurite in the last couple of years. Fig. 5.0.4 shows the temperature dependence of the specific heat at ambient-pressure and at zero magnetic field. Two round-shaped peaks are observed upon cooling at around 18 K and 4 K which coincide with anomalies observed in magnetic susceptibility measurements, shown in Fig. 5.0.5. There is a little mismatch of the above-mentioned peak positions for the two different quantities. The $T \approx 20$ K anomaly refers to the dimer $S_{dimer} = 0$ formation whereas the short-range ordering of monomer spins happens at $T \approx 4$ K. Moreover, a sharp and huge peak is observed in the specific heat data at around 1.88 K which corresponds to the three-dimensional antiferromagnetic long-range magnetic ordering [29]. A large structural distortion is also observed in thermal expansion, sound velocity and neutron scattering (NS) measurements which coincides with the long-range ordering at 1.88 K [121, 122].

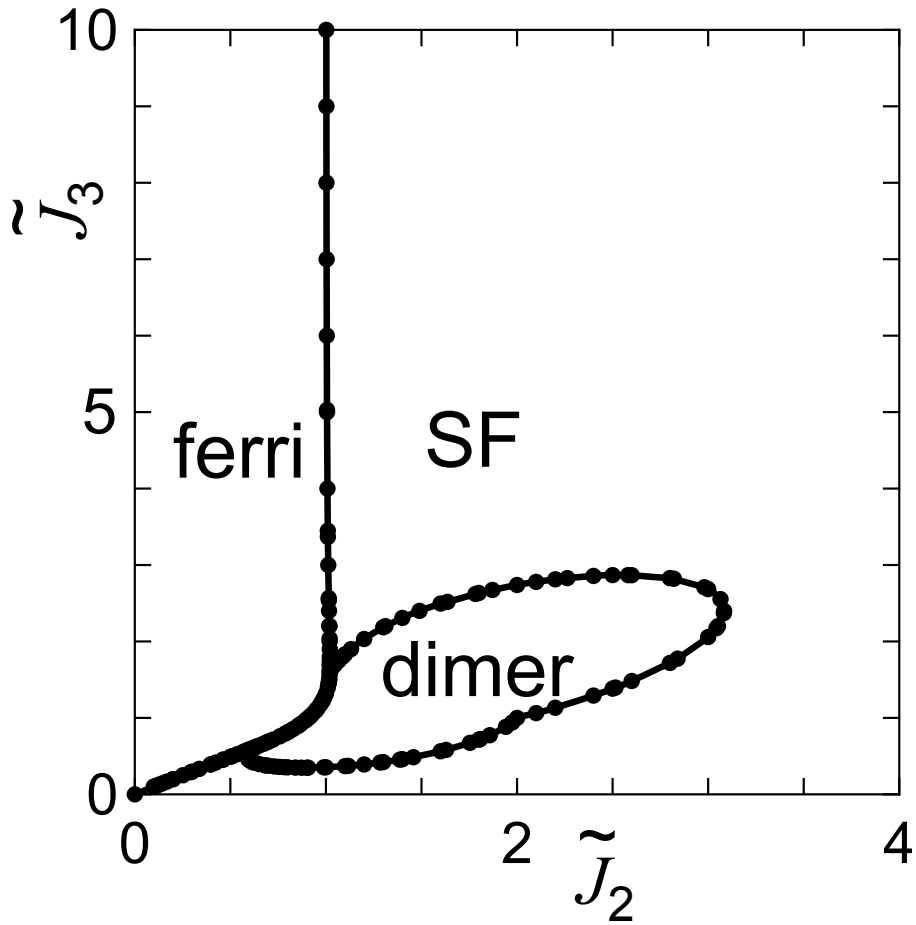

Figure 5.0.3: The phase diagram of the distorted diamond-chain model in the $\tilde{J}_2$-$\tilde{J}_3$ plane, where $\tilde{J}_2 \equiv J_2/J_1$ and $\tilde{J}_3 \equiv J_3/J_1$ (adapted from ref. [28]).

From the magnetization measurement, shown in Fig. 5.0.6, a magnetization plateau at 1/3 of the saturation magnetization M_s, was found when the magnetic field is applied parallel to the b-axis. Three distinct anomalies were observed in the magnetization as a function of magnetic field. The effect became more pronounced as the temperature is lowered. Among the three anomalies (H_{c1} = 16 T, H_{c2} = 26 T and H_{c3} = 32.5 T), H_{c1} and H_{c2} are the most spectacular ones as here the magnetization values remain at the constant value of 0.3 μ_B, μ_B is the Bohr magneton. This constant magnetization is almost 1/3 of saturation magnetization (M_s) and it can be explained by the theoretical distorted diamond-chain model. This phenomenon is also observed when the magnetic field is applied perpendicular to the b-axis with slightly different H_{c1} and H_{c2} values. The 1/3 magnetization plateau indicates the polarization of the monomer spins with an applied magnetic field. By performing ^{63,65}Cu-NMR measurements in high-magnetic field, the 1/3 magnetization plateau of azurite was also characterized. These measurements provide evidence for a quantum plateau containing the dimers in a singlet state and the fully polarized monomers [123]. Thermal expansion and magnetostriction mea-

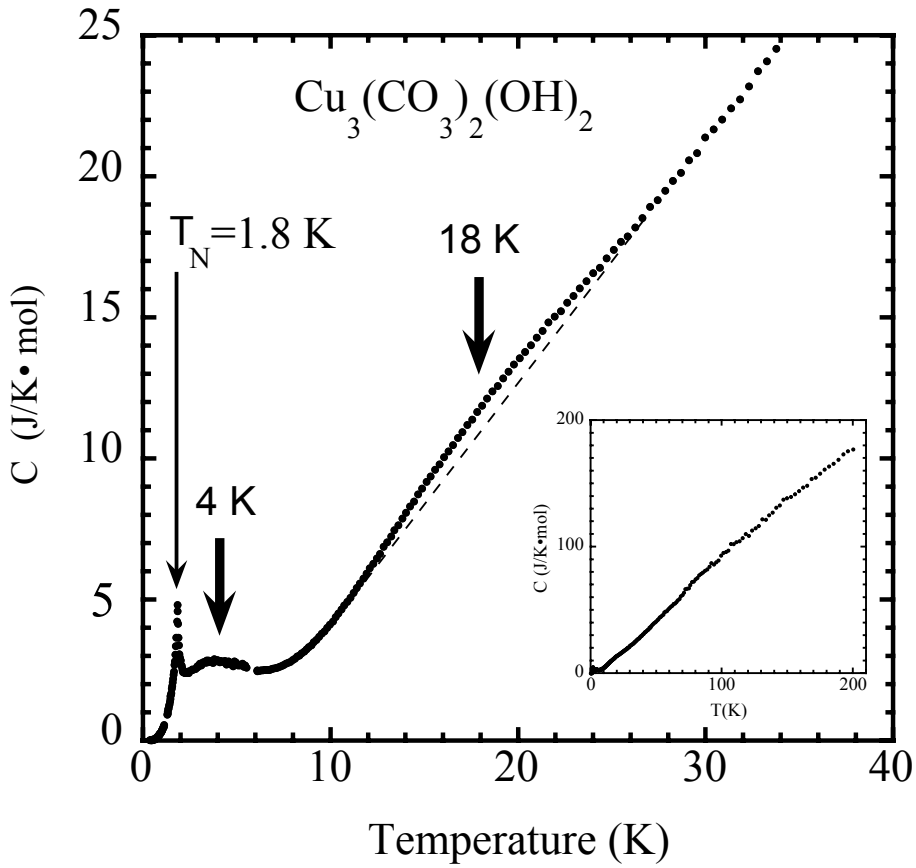

Figure 5.0.4: Low-temperature specific heat data showing three distinct anomalies (adapted from ref. [29]). The broken line is the guide for the eyes to highlight the anomaly at around 18 K. Inset: specific heat data over the wide temperature range.

surements have been carried out at very low-temperature (0.05 - 2.30 K) and magnetic fields up to 31 T showing a pronounced structural distortions accompanies the transition to the long-range antiferromagnetic ordering and the transition to the 1/3 magnetization plateau [124]. Ultrasonic measurements (c_{22}) at high magnetic fields suggest that the spin-phonon interaction in this material plays a significant role [125]. There is a controversy of the exchange coupling constants [29, 126, 127]. Susceptibility data have been analyzed using exact diagonalization (ED), density matrix renormalization group ($DMRG$), and high-temperature series expansion, cf. Fig. 5.0.5. The best fit was achieved for the exchange coupling constant values $J_1 = 19$ K, $J_2 = 24$ K and $J_3 = 8.6$ K (J_1:J_2:J_3 = 1:1.25:0.45) [29]. But these parameters fail to fit the low-temperature behavior of azurite. By using the parameters given in ref. [29], finite-temperature transfer matrix renormalization group ($TMRG$) gives a nice fitting to the two round-shaped peaks at low-temperature in the magnetic susceptibility data with the exchange coupling constants J_1:J_2:J_{3z} = 1:1.19:-0.3 and $J_1 = 23$ K [128]. Recently, Jeschke *et al.* proposed a microscopic model based on density functional theory (DFT) as well as state-of-the-art numerical many-body calculations which can explain all the available experiments:

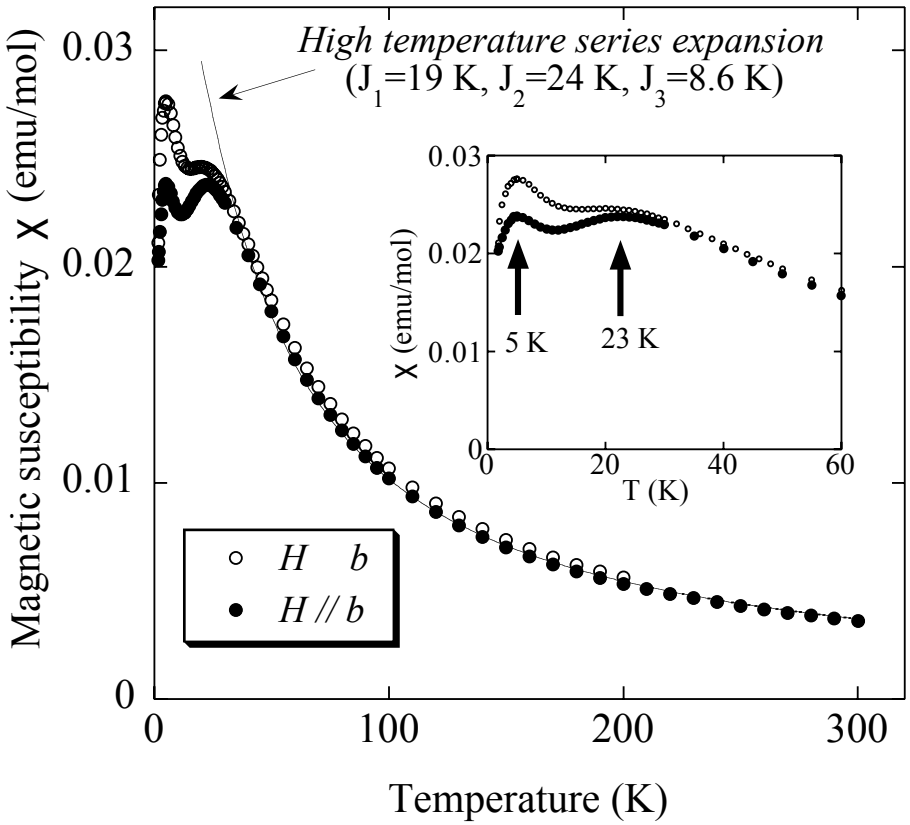

Figure 5.0.5: Temperature dependance of the magnetic susceptibility of azurite for the magnetic field parallel and perpendicular to the b-axis (adapted from ref. [29]). Solid line corresponds to a fit obtained from the high-temperature series expansion to extract the exchange coupling constants (J_1 = 19 K, J_2 = 24 K and J_3 = 8.6 K). Inset: low-temperature anomalies on expanded scales.

low-temperature magnetization, inelastic neutron scattering, nuclear magnetic resonance, magnetic susceptibility, and specific heat measurements. Moreover, based on the full potential local orbital (*FPLO*) GGA+U calculations with U = 8 eV for various models, different possible exchange coupling values are calculated. From this calculation, additional 3D coupling constants between dimer ions J_4 and J_7, monomer and dimer ions J_5, J_6, monomer-monomer coupling J_m, nearest-neighbor Cu dimer interaction along the chain J_d have been calculated. The values of the exchange coupling constants obtained from different models are shown in Table 5.1 [127]. It is also shown by performing high-resolution inelastic neutron-scattering measurements that the interchain coupling and an anisotropic staggered field are important to describe the complete dynamics of azurite [129].

	J_1	J_2	J_3	J_4	J_5	J_6	J_7	J_m	J_d
1 full model	13.5	42.8	12.5	2.7	0.6	4.4	-1.7	2.6	-0.4
2 minimal model	17.9	43.9	12.0	...	...	...	...	2.4	...
3 refined model	15.51	33.0	6.93	...	...	...	...	4.62	...

Table 5.1: Exchange coupling constants based on full potential local orbital (*FPLO*) method with GGA+U calculations (adapted from ref. [127]).

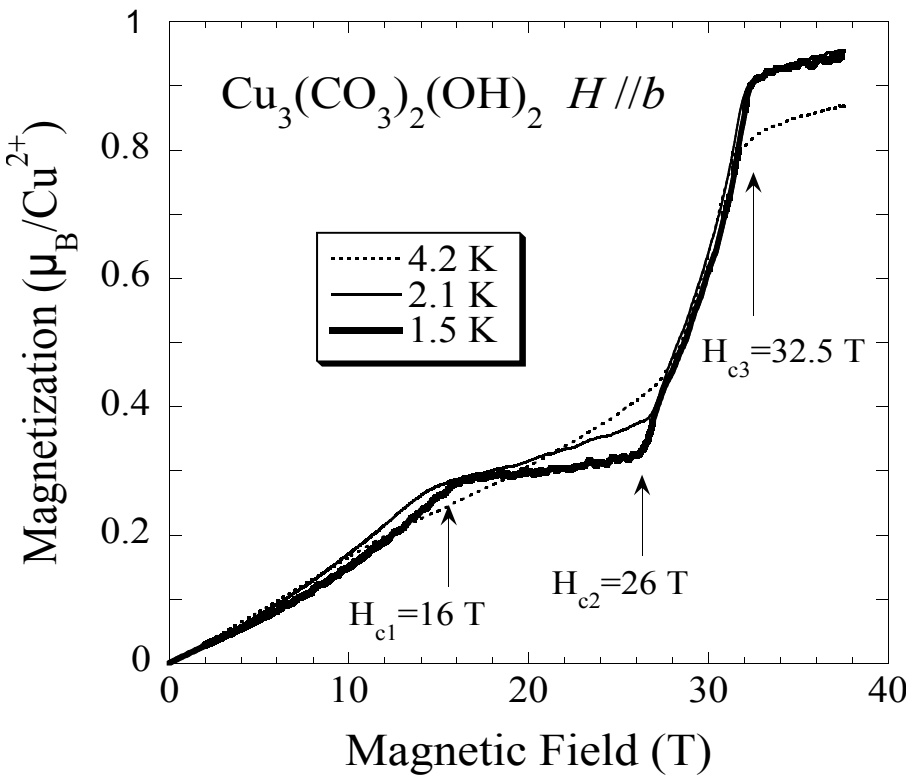

Figure 5.0.6: Magnetization measurements as a function of magnetic field for azurite taken at different constant temperatures of 1.5 K, 2.1 K and 4.2 K (adapted from ref. [29]). The field is applied parallel to the b-axis. The magnetization plateau is observed at 1/3 of the saturation magnetization.

5.1 Thermal expansion at ambient-pressure

The performance of the new setup, 'thermal expansion under pressure' has been checked first at ambient-pressure ($P \simeq 0$) on a single crystal of azurite, $Cu_3(CO_3)_2(OH)_2$. Fig. 5.1.1 shows the uniaxial thermal expansion coefficient (α) along the [010]-direction, *i.e.*, b-axis of azurite from $T = 1.5$ K to $T = 100$ K at ambient-pressure[5.1.1]. The crystal of azurite used for this experiment, was cut from the same large single crystal explored ref. [121]. The data show three distinct anomalies upon cooling which can be explained

[5.1.1] The calculation of cell effect for this new instrument has been explained elaborately in chapter 2.

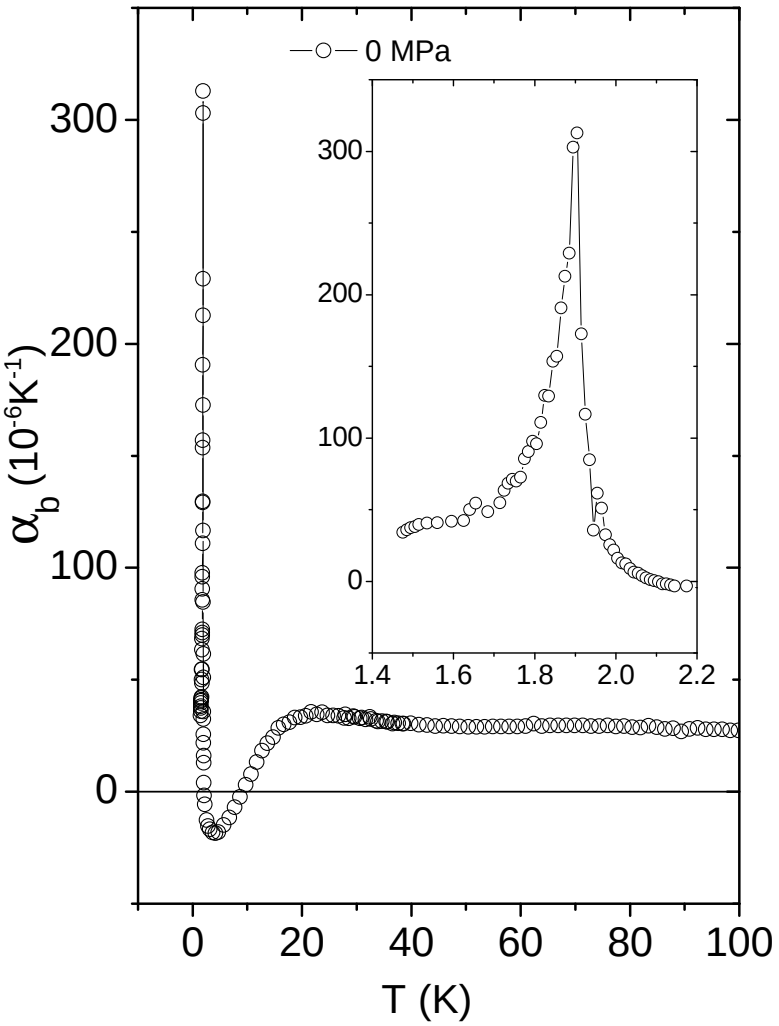

Figure 5.1.1: Thermal expansion measurements of azurite along the chain direction, *i.e.*, b-axis at ambient-pressure for temperatures $T \leq 100$ K. The data show three distinct anomalies mentioned in the text. Inset: 3D long-range antiferromagnetic order at $T_N = 1.88$ K on expanded scales.

by the distorted diamond-chain model. The formation of spin singlet $S_{dimer} = 0$ dimers happens at $T \approx 20$ K and it is associated with two-thirds of the material's Cu^{2+} spins. The short-range ordering of the monomer spins occurs at $T \approx 4$ K, which involves the remaining one-third of the Cu^{2+} spins. The dominant energy scale of the system is an antiferromagnetic intra-dimer exchange coupling $J_2/k_B \simeq 33$ K, associated with the spin-singlet formation of the $S_{dimer} = 0$ dimers. The corresponding antiferromagnetic monomer-monomer exchange coupling is $J_m/k_B \simeq 4.6$ K [127]. Upon cooling down further, long-range antiferromagnetic order was observed at $T_N = 1.88$ K as a consequence

of weak three-dimensional magnetic interactions. The data coincide with the published data [121, 122, 130].

5.2 Pressure effect on T_N

At a second-order phase transition, the discontinuities in the thermal expansion and specific heat are related via the Ehrenfest relation to give the pressure dependence of the transition temperature in the limit of vanishing pressure:

$$\left(\frac{\mathrm{d}T_c}{\mathrm{d}P}\right)_{P\to 0} = V_{mol}T_c\frac{\Delta\beta}{\Delta C_P} \tag{5.2.1}$$

From this relation one can calculate the pressure effect of the phase transition temperature (T_c). As the long-range order of azurite occurs at $T_N = 1.88$ K, the pressure effect of T_N can be calculated, provided the volume expansion and the specific heat are known across the transition. The volume expansion coefficient[5.2.1] across the transition is $\Delta\beta \simeq 550\times10^{-6}$ K^{-1} [130] and the specific heat discontinuity is $\Delta C \simeq 8$ J mol^{-1}K^{-1} [126]. So a positive discontinuity in the shift of T_N of 12 mK per MPa, *i.e.*, $\mathrm{d}T_c/\mathrm{d}P = 12$ mK/MPa is expected, where the molar volume of azurite is $V_{mol} = 9.14\times10^{-5}$ m^{3}mol^{-1}.

As the pressure medium in our experiment is helium (^4He), the pressure should not exceed ~ 2.5 MPa to avoid solidification of ^4He at low temperatures [37].

5.3 Thermal expansion under pressure

5.3.1 Experimental conditions and limitation

There are a couple of experimental limitations which crop up as the thermal expansion under helium (^4He) gas pressure deals with many parameters. As the volume of the pressure cell (V_1) is as large as 81.4 cm^3, measurements as a function of temperature at constant-pressure conditions require that the volume of the high-pressure reservoir (V_2) should be several liters at minimum. Thus the condition $V_2 \gg V_1$ can be met only by using a ^4He-gas bottle ($V_2 = 50{,}000$ cm^3), the maximum pressure of which is limited to 18 MPa. More experimental details are discussed in chapter 2.

[5.2.1] Volume expansion coefficient is nothing but the summation of thermal expansion coefficients along three different directions. There is a very small error associated with it as the crystal structure of azurite is monoclinic with an angle $\beta = 92.43°$.

The capacitive dilatometer works only when helium is in the gaseous or liquid phase. So in order to perform the pressure experiment down to very low temperatures, one has to be careful that helium should not go to the solid phase. According to the pressure-temperature phase diagram [37, 38] of helium, the pressure value should stay below 2.5 MPa in order to measure the thermal expansion down to 1.3 K by using this setup. For this reason, for azurite, measurements are performed at temperatures down to 2.7 K and 3.4 K for pressure values 6.2 MPa and 9.5 MPa, respectively. The precise value of the pressure was checked by employing a pressure gauge (heavily doped *n-InSb*) and cross-checked via the helium solidification point, *viz.*, calculated the pressure value at a particular temperature where helium solidifies by using the pressure-temperature phase diagram [38].

5.3.2 Experimental observation

Fig. 5.3.1 shows the thermal expansion coefficient of azurite along the crystallographic b-axis, *i.e.*, [010]-direction for temperatures $T \leq 100$ K at ambient-pressure and finite pressure values. The measurements were done with a sweep rate of $\pm$ 0.5 K/hour to $\pm$ 1.5 K/hour at ambient-pressure and different constant-pressures 1.0, 2.0, 6.2 and 9.5 MPa. The thermal expansion coefficient shows large changes, especially at low temperatures and finite pressures, suggesting a strong pressure effect of the low-temperature properties of azurite. In order to calculate the thermal expansion coefficient under pressure, the variation of the dielectric constant of helium as a function of pressure and temperature is taken into account. However, as was discussed in chapter 2.6, within the van der Waals approximation this is only a small effect and accordingly the values of thermal expansion coefficient do not change significantly by incorporating the corresponding variation of the dielectric constant. Upon cooling till 50 K, there is no significant pressure effect on azurite, but the curves start to deviate from each other upon further cooling. From the data, it seems that the 20 K anomaly is smeared out by applying only $\sim$ 10 MPa, but as the pressure values go higher, the peak position shifts to the higher temperature. In contrast to that, the 4 K anomaly grows in size as the pressure is increased and shifts to the lower temperature. Apparently, the peak position and size of the 4 K anomaly do not follow a smooth variation with pressure, but rather show a highly non-linear behavior. The huge and sharp anomaly at small pressure value is reminiscent of a λ-type anomaly. With pressure values 1.0 and 2.0 MPa, it was possible to measure down to 1.5 K. In order to perform all the measurements in equilibrium condition, a slower temperature sweep rate ($\pm$ 1.5 K/hour) is used in general. However, at lower pressure (1.0 and 2.0 MPa) it was difficult to maintain the constant-pressure condition. As a matter of fact, a much slower temperature sweep rate of $\pm$ 0.5 K/hour was necessary. It would have been nice to measure below this pressure to see how the 4 K anomaly evolves under lower pressure, but it was difficult to ensure the constant-pressure condition here. Even though the measurements were done in a T, P range sufficiently away from the critical point of helium ($P_c = 0.227$ MPa, $T_c = 5.2$ K) [37], this might have had some influence

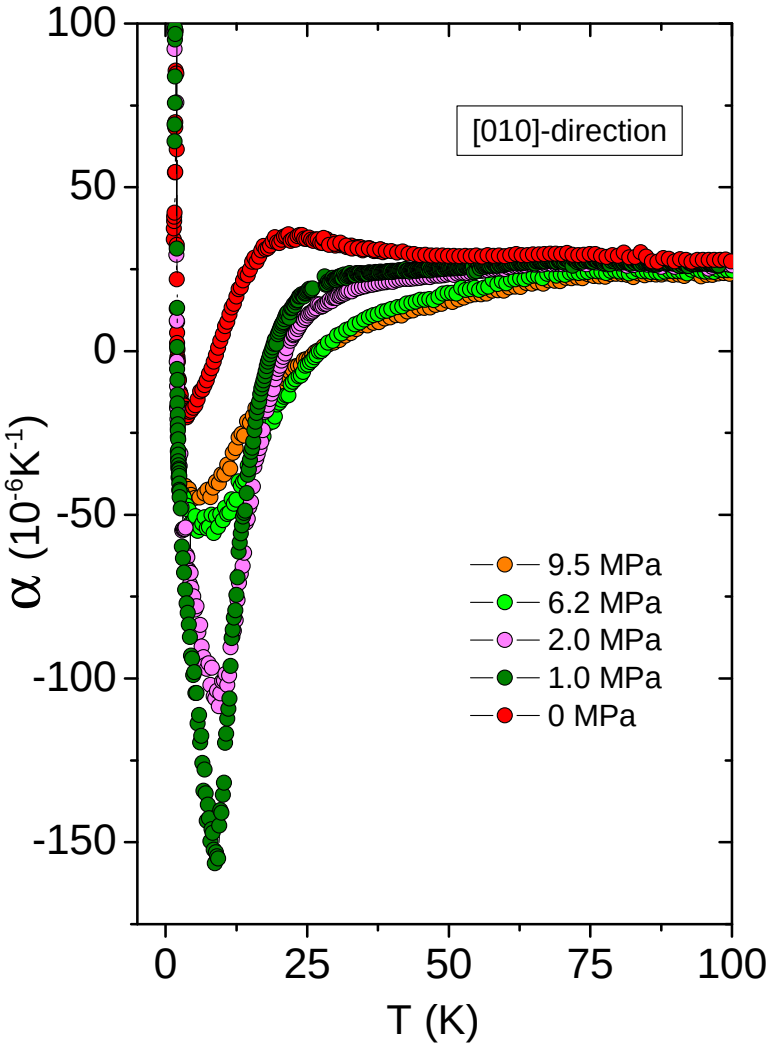

Figure 5.3.1: The variation of the thermal expansion coefficient as a function of temperature of azurite along the chain direction, *i.e.*, b-axis at ambient and finite pressure (1.0, 2.0, 6.2 and 9.5 MPa) values. The data around the Néel ordering temperature (T_N = 1.88 K) have been truncated in order to make the pressure effect around the 4 K and 20 K anomalies clearly visible. All measurements were performed with a small temperature sweep rate (0.1 K/hour to 1.5 K/hour) to ensure constant-pressure conditions. The 'pressure-induced cell effect' is not subtracted from the data.

on the constant-pressure condition and, above all, on the dielectric constant of helium. The effect of critical fluctuations is not accounted for in the calculations of the dielectric constant based on the Clausius-Mossotti and van der Waals equations, discussed in chapter 2.6. Generally, due to the large specific heat when the system is under pressure, *viz.*, the increased number of particles, one should optimize the temperature sweep rate

to nullify the hysteresis in pressure. The pressure effect on the 4 K anomaly of azurite at lower pressure (1.0 and 2.0 MPa) was unexpectedly large and as such was the motivation to measure the known reference aluminium sample of length 7 mm under these pressure values. This gives the 'pressure-induced cell effect', which is already discussed in the experimental section, cf. chapter 2.6. Such a huge "cell effect" under pressure, mainly at lower temperature could signify the influence of the critical point of helium, *i.e.*, the influence of the critical density fluctuations on ε_r.

Fig. 5.3.2 shows the very low-temperature behavior of azurite, namely, across the Néel ordering temperature (T_N) under pressure of 1.0 and 2.0 MPa in comparison with ambient-pressure. 1.0 MPa was the minimum pressure which was applied. A 20 mK positive temperature shift of $T_N = 1.88$ K was expected under 2.0 MPa pressure according to the Ehrenfest relation. Unfortunately, T_N of azurite coincides with the superfluid transition of helium at 2.0 MPa. As the specific heat is very large at the superfluid transition, so it was difficult to control the temperature across this temperature range. In order to solve this problem, discontinuous, step-wise measurements were performed with temperature steps of 10 mK and supplemented by continuous measurements at a very small sweep rate of - 0.1 K/hour. From the figure it is seen that there is a negative shift of the position of the peak anomaly in $\alpha_{[010]}$, suggesting a suppression of T_N under 1.0 and 2.0 MPa which is contradictory to the Ehrenfest relation. The reason for this might be related to the disturbing effect of the superfluid transition under pressure on the Néel ordering temperature (T_N) as two transitions overlap.

5.3.3 Discussion

Fig. 5.3.3 shows the azurite data under pressure after subtraction of the 'pressure-induced cell effect'. The 'pressure-induced cell effect' is small at around 20 K and, as such, does not influence the anomaly at 20 K, but the anomaly at 4 K where the cell effect is large, is reduced significantly. The data are shown here for the finite pressure values, *viz.*, 2.0, 6.2 MPa and 9.5 MPa because the 'pressure-induced cell effect' was also measured for these pressure values using an annealed *Al* sample. The calculation of the cell effect for the finite pressure values is discussed in the experimental section, cf. chapter 2.6. It was difficult to perform the measurements for azurite and the *Al* sample exactly at the same pressure values. So there is an error bar of ± 0.3-0.4 MPa associated with the above-mentioned data[5.3.1].

From the figure, it is seen that such small pressure values have a surprisingly strong effect on the low-temperature expansivities of azurite. While α_b at $P \simeq 0$ gradually

[5.3.1] This 'pressure-induced cell effect' has been cross-checked by measuring an annealed *Cu* sample at 6.2 MPa. The thermal expansion coefficient of the annealed *Cu* sample as a function of temperature at 6.2 MPa matches with the literature value at ambient-pressure by taking into account the above-mentioned 'pressure-induced cell effect' (which was measured for the annealed *Al* sample), as it was expected.

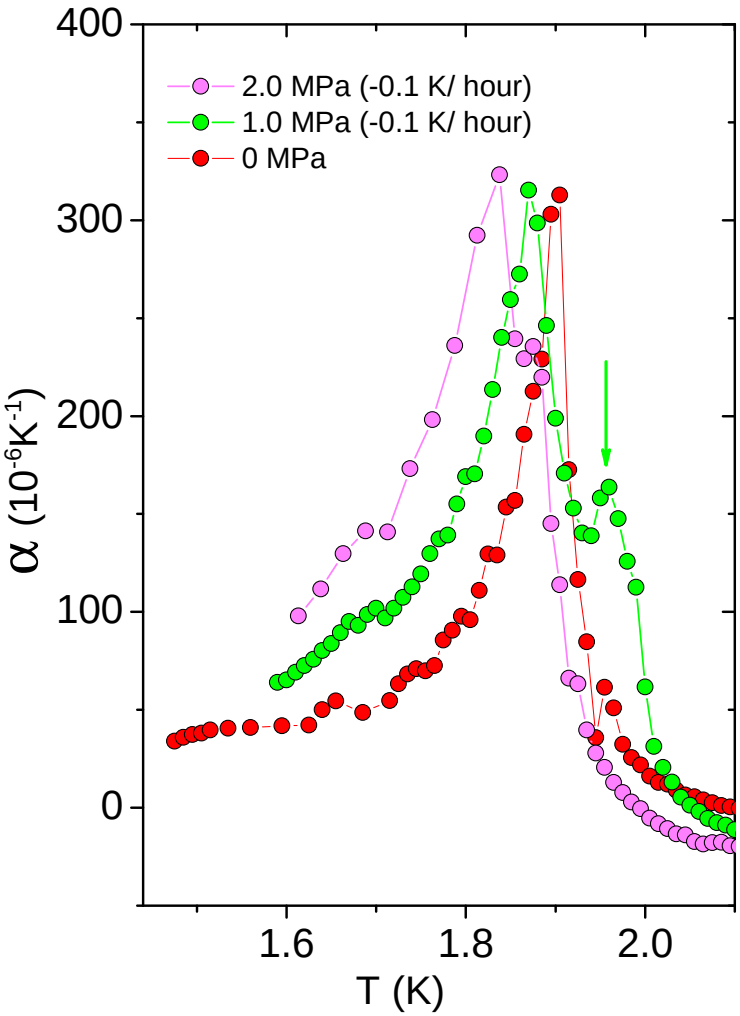

Figure 5.3.2: Pressure dependence of the Néel ordering temperature T_N. It was only possible to measure across T_N for the pressure values 1.0 and 2.0 MPa because of the experimental limitations implied by the solidification of helium. Unfortunately, the superfluid transition of helium (^4He) under pressure coincides with the Néel ordering temperature T_N of azurite under pressure. The arrow indicates the superfluid transition under a pressure of $P = 1.0$ MPa.

grows upon cooling from 100 K down to 20 K, the data at $P = 9.5$ MPa reveal a reduction with temperature. This is accompanied by a strong suppression of the pronounced maximum in α_b around 20 K, developing the form of a shoulder under pressure. By the application of hydrostatic pressure, α_b also seems to shift to the lower temperature. This is expected from the Grüneisen formalism as the volume expansion coefficient ($\beta \simeq$ -13×10^{-6} K^{-1}) around this anomaly has a negative sign [122] while the specific heat is positive [126]. For temperatures above about 120 K (not shown here), the finite pressure

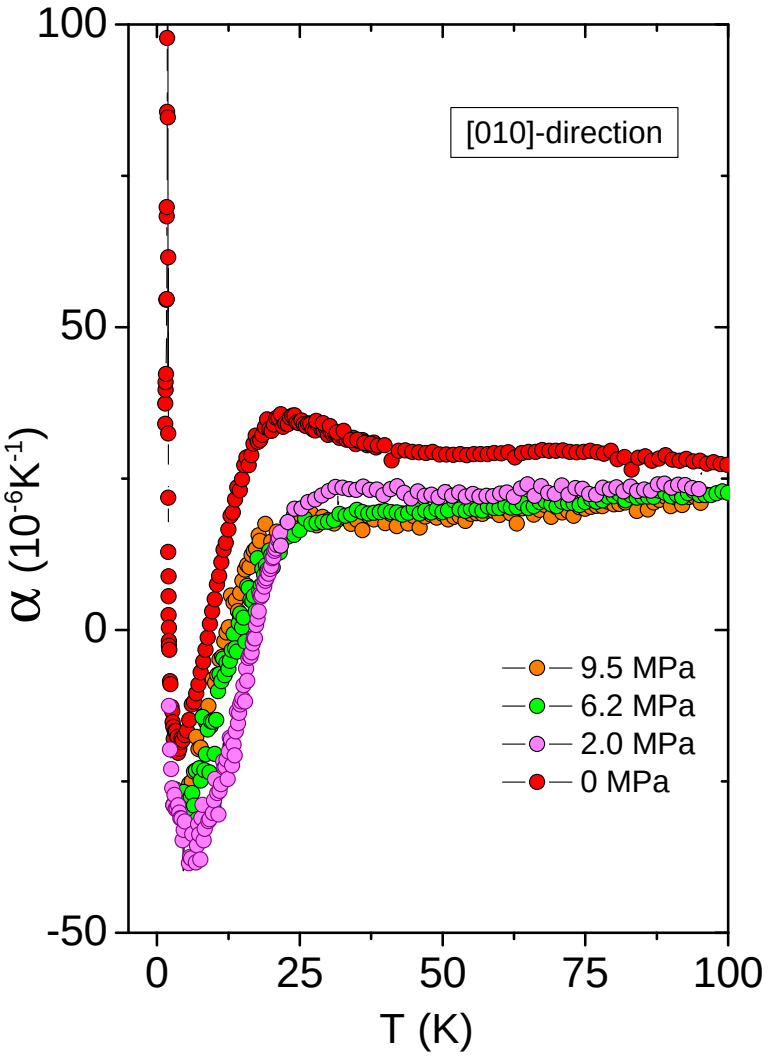

Figure 5.3.3: Temperature variation of the thermal expansion of azurite at ambient and finite pressure values after taking into account the 'pressure-induced cell effect'. The data around the Néel ordering temperature ($T_N = 1.88$ K) have been truncated in order to see the pressure effect around 4 K and 20 K anomalies more clearly.

curves merge with the ambient-pressure data. Due to the solidification of helium, it was not possible to measure down to 1.5 K for the pressure values $P \gtrsim 2.5$ MPa. There is no significant difference between the data of 6.2 MPa and 9.5 MPa. From the present data, it seems that the anomaly at 4 K also has a pronounced effect under pressure. The $P = 2.0$ MPa data show little less effect at the $T = 20$ K anomaly compared to other two higher pressure values, but the data enable to access the 4 K anomaly. α_b shows

a huge anomaly corresponding to the 4 K anomaly at 2.0 MPa and shifts to the higher temperature. From the experimental point of view, it would be relevant to study this compound at a somewhat higher pressure value like 100 MPa which is presently being performed. As partly competing exchange coupling constants play an important role in this compound, it would be interesting to study how these exchange coupling constants modify under pressure, as the thermal expansion under pressure provides a most sensitive tool for identifying and exploring the dominant interactions.

6 Summary

Thermal expansion measurements provide a sensitive tool for exploring a material's thermodynamic properties in condensed matter physics as they provide useful information on the electronic, magnetic and lattice properties of a material. In this thesis, thermal expansion measurements have been carried out both at ambient-pressure and under hydrostatic pressure conditions. From the materials point of view, the spin-liquid candidate κ-(BEDT-TTF)$_2$Cu$_2$(CN)$_3$ has been studied extensively as a function of temperature and magnetic field. Azurite, Cu$_3$(CO$_3$)$_2$(OH)$_2$ - a realization of a one-dimensional distorted Heisenberg chain is also studied both at ambient and hydrostatic pressure to demonstrate the proper functioning of the newly built setup 'thermal expansion under pressure'.

One part of the thesis was to build up the thermal expansion apparatus under hydrostatic pressure measurements. By the application of hydrostatic pressure, many properties of the materials can be studied, *e.g.*, the Mott metal-insulator transition, superconductivity, quantum phase transition, finite temperature critical end point, etc. A pressure cell made of *CuBe* has designed with a volume of 81.4 cm^3 in order to measure the thermal expansion of a material under helium gas pressure $P \leq 250$ MPa with an inner and outer diameter of 36 mm and 56 mm respectively and inner length of 80 mm. Helium gas (^4He) is used as a pressure-transmitting medium. As a pressure reservoir either a helium gas bottle (50,000 cm^3) in combination with a helium gas compressor (Unipress Gas Compressor U11) is used as a pressure source where pressures of $P \leq 18$ MPa can be applied. A heavily doped *n-InSb* single crystal is used as a pressure sensor. The thermal expansion can be measured as a function of temperature for different constant-pressure values within the pressure resolution of $\pm$ 0.1 MPa.

Measurements of the uniaxial expansivities have been performed on the organic charge-transfer salt κ-(ET)$_2$Cu$_2$(CN)$_3$, where ET = BEDT-TTF, is a spin $S = 1/2$ Mott insulator with a two-dimensional (2D) triangular-lattice structure. Because of the almost perfect geometrical frustration $t'/t \sim 0.8$ in this material, it has been proposed that quantum fluctuations destabilize the long-range magnetic order and, instead, lead to

liquid-like properties of the spin system. Issues of high current interest include the nature of the low-lying elementary excitations of the spin-liquid instabilities like crossover from a thermally disordered state to a quantum disordered state, phase transition associated with the formation of spinons and exciton condensation near a Z_2 spin-liquid of bosonic spinons, gapless, spin-gapped are discussed in the literature. The specific heat and magnetic susceptibility measurements also have been performed in order to understand the low-lying elementary excitations of this material. The specific heat and thermal conductivity measurements have been reported in the literature yielding an anomaly at 6 K. However, it was not possible to discover whether it is a crossover or a phase transition. Thermal expansion measurements along the three different axes show a huge and sharp anomaly at 6 K which strongly couples to the lattice degrees of freedom, identifying this feature as a phase transition. The lack of hysteresis across this transition proved that it is a second-order phase transition. The in-plane (bc) thermal expansivity shows a clear anisotropic behavior corresponding to a significant distortion of the triangular-lattice. The temperature derivative of the magnetic susceptibility shows also a peak at 6 K, indicating that the spin degrees of freedom are involved in the transition. By employing a Grüneisen-scaling Ansatz, the corresponding contribution to the specific heat has been determined, which also shows a clear anomaly at 6 K and the entropy release at the phase transition suggests that the charge degrees of freedom are involved in the transition. The volume expansion coefficient shows a much less peculiar behavior and lacks any anomaly at 6 K. The absence of an anomaly in the volume expansion coefficient signifies that, according to the Ehrenfest relation, the 6 K anomaly is insensitive to the application of hydrostatic pressure.

Thermal expansion measurements show the strong magnetic field dependence in κ-(BEDT-TTF)$_2$Cu$_2$(CN)$_3$ along the particular crystallographic direction, *viz.*, in-plane b-axis, while the other two axes are field insensitive. The results at zero field show a broad minimum centered around 8 K, corresponding to a change of sign along the b-axis thermal expansion coefficient α_b. The 6 K phase transition is insensitive to the magnetic fields $B \leq 10$ T, the maximum field applied, but a finite field 0.5 T $< B_c \leq 1$ T is required in order to observe this effect. The anomaly grows in size and shifts to the lower temperature as the field is increased. A peculiarity of this B-induced anomaly is the undershoot (overshoot) behavior on the high (low)-temperature side of the discontinuity. The magnetostriction measurements show two step-like anomalies with increasing the magnetic field. From the field-temperature anomaly diagram, it is seen that the two anomalies merge together at around 8.4 K. One of these anomalies in the thermal expansion lies close to the phase boundary between a quantum critical (QC_H) and a weak antiferromagnetic (WAF_H) phase recently reported in the literature. This phenomenon is reminiscent of "flux-pinning-related" effects, but the lack of hysteresis upon warming and cooling is puzzling. Alternatively, field-induced orbital motions of the π-electrons and their effect on the exchange coupling constants are worth to be considered. Higher warming and cooling rates do not effect the anomaly which is an indication that there is no spin glass-like behavior. Some sample-to-sample dependence is observed in this

compound measured along the b-axis. The size of the 6 K anomaly at $B = 0$ T is related to the magnetic field dependency, *i.e.*, when the 6 K anomaly is bigger in size for a given crystal, the magnetic field dependency is also more pronounced.

Temperature-dependent structural and electronic properties also play an important role for this spin-liquid compound. On measuring the crystal structure of this material for a series of temperatures between 5 K and 300 K by single crystal X-ray diffraction, the electronic structures have been evaluated by using density functional theory and tight-binding methods. It is shown that the degree of frustration and interaction strength change significantly as a function of temperature. Interestingly, t'/t which determines the effect of frustration in an anisotropic triangular-lattice, shows a hump-like anomaly at around 150 K. The interaction strength (U/t) increases monotonically upon cooling from room temperature. The ratio between the in-plane c and b lattice vectors which has an influence on the ratio of t'/t, also changes significantly as a function of temperature, showing a hump at around 150 K. This anomaly could be associated with the ordering of the ethylene groups.

The performance of the 'thermal expansion under pressure' setup has been checked first at ambient-pressure ($P \simeq 0$) on a single crystal of azurite, $Cu_3(CO_3)_2(OH)_2$ - a realization of a one-dimensional distorted diamond-chain. Small finite pressure values (2.0 MPa, 6.2 MPa, 9.5 MPa) have a surprisingly strong effect on the low-temperature expansivities of azurite. The maximum allowed pressure $P = 9.5$ MPa reveals a reduction with the temperature which is accompanied by a strong suppression of the pronounced maximum in α_b around 20 K, developing the form of a shoulder under pressure. By the application of hydrostatic pressure, α_b also seems to shift to the lower temperature. This is expected from the Grüneisen formalism as the volume expansion coefficient ($\beta \simeq$ -13×10^{-6} K^{-1}) around this anomaly has a negative sign. As competing exchange coupling constants play an important role in this compound, it would be interesting to study how these exchange coupling constants modify under pressure as the thermal expansion under pressure provides a most sensitive tool for identifying and exploring the dominant interactions.

7 Outlook

In this thesis, thermodynamic measurements have been performed on the low-dimensional materials, *viz.*, spin-liquid candidate κ-$(ET)_2Cu_2(CN)_3$ and azurite, $Cu_3(CO_3)_2(OH)_2$. From the experimental point of view, mainly thermal expansion measurements have been performed both at ambient and finite hydrostatic pressure values. There are many aspects which can be extended in the future based on the achievements made in this thesis.

From an instrumentation point of view, the 'thermal expansion under pressure' setup can be modified by using a specially-designed ^4He-gas compressor. The main principle of this setup is to measure the thermal expansion of a material as a function of temperature at different constant-pressure values. In order to maintain the constant-pressure condition, the volume of the pressure cell should be very small compared to the volume of the pressure reservoir in order to compensate the pressure changes due to temperature changes. The large volume of the pressure cell $V = 81.4$ cm^3 which is needed to place the dilatometer cell, makes it particularly difficult to ensure constant-pressure conditions. So in the present case, a bigger volume of a ^4He-gas bottle is used and connected via the compressor where the constant-pressure condition is maintained. But there is a limitation of the maximum pressure of 18 MPa. For that reason the ^4He-gas compressor can be modified by employing an enlarged volume of the high-pressure stage and an active pressure control device which includes a step-motor-driven micropump in order to compensate for the pressure changes due to temperature changes inside the pressure cell.

Once the above setup is ready with all the modifications, many low-dimensional systems can be explored. Out of these, organic conductors, namely, κ-$(ET)_2Cu[N(CN)_2]Cl$ shows a first-order Mott metal-insulator transition by applying only ≈ 30 MPa. This first-order Mott transition line ends up at a second-order critical end point. This Mott criticality can be studied by applying pressure and the question will be answered whether it follows an unconventional or a two-dimensional Ising-type critical behavior.

In the case of the spin-liquid system κ-(BEDT-TTF)$_2$Cu$_2$(CN)$_3$ more studies are necessary to understand the nature of the 6 K phase transition, mainly to unreveal the order parameter associated with it. From the thermodynamic analysis, *viz.*, by employing the Ehrenfest relation, it is shown in this thesis that the 6 K phase transition is insensitive to the application of hydrostatic pressure. So it would be interesting to check this experimentally and to extend the studies to the pressure range where superconductivity shows up. As the superconducting transition temperature of this compound under finite pressure is $T_c = 4.5$ K, there might be an inter-relation between the 6 K phase transition and superconductivity. Based on the single crystal diffraction measurements at different temperatures, the evolution of the electronic properties have been simulated by using density functional theory and tight-binding methods. As the measurement steps were of the order of 50 K, it is difficult to estimate the exact ordering of ethylene groups temperature $T \simeq 150$ K. Continuous measurements or a smaller step widths would be helpful for this. To check whether there is a symmetry breaking associated with the phase transition at 6 K neutron scattering experiment could be performed. Recently, one more spin-liquid compound, EtMe$_3$Sb[Pd(dmit)$_2$]$_2$, was discovered. This compound is also a dimer-based organic Mott insulator and has the spin-liquid instability like κ-(BEDT-TTF)$_2$Cu$_2$(CN)$_3$ together with an anomaly at 3.7 K. This could also be an interesting study for future thermal expansion measurements along all the crystallographic axes.

As there was a pressure limitation of the 'thermal expansion under pressure' setup, with the installation of the new ^4He-gas compressor system, containing an active pressure control, high-pressure experiments can be performed in order to understand the strong pressure effects in azurite. This also includes measurements along the other crystallographic axes *viz.*, a' and c^*-axes. In particular, it is interesting to study the evolution of the 4 K and 20 K anomalies at high pressure (> 10 MPa).

Bibliography

[1] T. H. K. Barron, J. G. Collins, and G. K. White, Adv. Phys. **29**, 609 (1980).

[2] M. de Souza, A. Brühl, Ch. Strack, B. Wolf, D. Schweitzer, and M. Lang, Phys. Rev. Lett. **99**, 037003 (2007).

[3] Y. Kurosaki, Y. Shimizu, K. Miyagawa, K. Kanoda, and G. Saito, Phys. Rev. Lett. **95**, 177001 (2005).

[4] T. Komatsu, N. Matsukawa, T. Inoue, and G. Saito, J. Phys. Soc. Jpn. **65**, 1340 (1996).

[5] N. F. Mott, Rev. Mod. Phys. **40**, 677 (1968).

[6] V. Dobrosavljevic, arXiv:1112.6166 (2011).

[7] M. Imada, A. Fujimori, and Y. Tokura, Rev. Mod. Phys. **70**, 1039 (1998).

[8] N. Toyota, M. Lang, and J. Müller, *Low-dimensional Molecular Metals*, Springer Series in Soild-State Sciences Vol. **154** (Springer-Verlag, Berlin, 2007).

[9] P. Kopietz, L. Bartosch, and F. Schütz, *Introduction to the Functional Renormalization Group*, Lect. Notes Phys. Vol. **798** (Springer-Verlag, Berlin, 2010).

[10] P. Limelette, A. Georges, D. Jérome, P. Wzietek, P. Metcalf, and J. M. Honig, Science **302**, 89 (2003).

[11] F. Kagawa, K. Miyagawa, and K. Kanoda, Nature (London) **436**, 534 (2005).

[12] F. Kagawa, K. Miyagawa, and K. Kanoda, Nat. Phys. **5**, 880 (2009).

[13] L. Bartosch, M. de Souza, and M. Lang, Phys. Rev. Lett. **104**, 245701 (2010).

[14] S. Papanikolaou, R. M. Fernandes, E. Fradkin, P. W. Phillips, J. Schmalian, and R. Sknepnek, Phys. Rev. Lett. **100**, 026408(2008).

[15] P. W. Anderson, Mater. Res. Bull. **8**, 153 (1973).

[16] L. Balents, Nature (London) **464**, 199 (2010).

[17] Y. Shimizu, K. Miyagawa, K. Kanoda, M. Maesato, and G. saito, Phys. Rev. Lett. **91**, 107001 (2003).

[18] M. Yamashita, N. Nakata, Y. Senshu, M. Nagata, H. M. Yamamoto, R. Kato, T. Shibauchi, and Y. Matsuda, Science **328**, 1246 (2010).

[19] R. Coldea, D. A. Tennant, and Z. Tylczynski, Phys. Rev. B **68**, 134424 (2003).

[20] H. D. Zhou, E. S. Choi, G. Li, L. Balicas, C. R. Wiebe, Y. Qiu, J. R. D. Copley, and J. S. Gardner, Phys. Rev. Lett. **106**, 147204 (2011).

[21] G. Misguich, C. Lhuillier, B. Bernu, and C. Waldtmann, Phys. Rev. B **60**, 1064 (1999).

[22] B. J. Powell and R. H. McKenzie, Rep. Prog. Phys. **74**, 056501 (2011).

[23] S.-S. Lee, P. A. Lee, and T. Senthil, Phys. Rev. Lett. **98**, 067006 (2007).

[24] Y. Qi and S. Sachdev, Phys. Rev. B **77**, 165112 (2008).

[25] F. D. M. Haldane, Phys. Rev. Lett. **67**, 937 (1991).

[26] A. P. Ramirez, Annu. Rev. Mater. Sci. **24**, 453 (1994).

[27] K. Okamoto, T. Tonegawa, and M. Kaburagi, J. Phys.: Condens. Matter **15**, 5979 (2003).

[28] K. Okamoto, T. Tonegawa, Y. Takahashi, and M. Kaburagi, J. Phys.: Condens. Matter **11**, 10485 (1999).

[29] H. Kikuchi, Y. Fujii, M. Chiba, S. Mitsudo, T. Idehara, T. Tonegawa, K. Okamoto, T. Sakai, T. Kuwai, and H. Ohta, Phys. Rev. Lett. **94**, 227201 (2005).

[30] K. Takano, K. Kubo, and H. Sakamoto, J. Phys.: Condens. Matter **8**, 6405 (1996).

[31] L. Zhu, M. Garst, A. Rosch, and Q. Si, Phys. Rev. Lett. **91**, 066404 (2003).

[32] R. Pott and R. Schefzyk, J. Phys. E **16**, 444 (1983).

[33] R. S. Manna, M. de Souza, A. Brühl, J. A. Schlueter, and M. Lang, Phys. Rev. Lett. **104**, 016403 (2010).

[34] R. S. Manna and M. Lang, (2012) (*in prepration*).

[35] *High-pressure Helium Gas Cell (HGC)*, Joint development between University of Frankfurt, Frankfurt and Institute of High-Pressure Physics (unipress), Warsaw (2009).

[36] Lake Shore Model 340 (LS340) Temperature Controller User's Manual, Ohio, USA.

[37] F. Pobell, *Matter and Methods at Low Temperatures*, Springer, (1992).

[38] D. W. J. Langer, J. Phys. Chem. Solids **21**, 122 (1961).

[39] F. R. Kroeger and C. A. Swenson, J. Appl. Phys. **48**, 853 (1977).

[40] R. P. Feynman, R. B. Leighton, and M. Sands, *The Feynman Lectures on Physics*, Vol. **2**, Ch. 32 (Addison-Wesley, 1964).

[41] P. V. Rysselberghe, J. Phys. Chem. **36**, 1152 (1932).

[42] J. F. Skinner, E. L. Cussler, R. M. Fuoss, J. Phys. Chem. **72**, 1057 (1972).

[43] J. W. Schmidt and M. R. Moldover, Int. J. Thermophys. **24**, 375 (2003).

[44] J. Ferraris, D. O. Cowan, V. Walatka, and J. H. Perlstein, J. Am. Chem. Soc. **95**, 948 (1973).

[45] R. H. McKenzie, Science **278**, 820 (1997).

[46] D. Jérome, A. Mazaud, M. Ribault, and K. Bechgaard, J. Physique Lett. **41**, 95 (1980).

[47] M. Dressel, Naturwissenschaften **94**, 527 (2007).

[48] J. Wosnitza, J. Low Temp. Phys. **146**, 641 (2007).

[49] J. Müller, M. Lang, F. Steglich, J. A. Schlueter, A. M. Kini, and T. Sasaki, Phys. Rev. B **65**, 144521 (2002).

[50] H. H. Wang, K. D. Carlson, U. Geiser, A. M. Kini, A. J. Schultz, J. M. Williams, L. K. Montgomery, W. K. Kwok, U. Welp, K. G. Vandervoort, S. J. Boryschuk, A. V. S. Crouch, J. M. Kommers, D. M. Watkins, J. E. Schriber, D. L. Overmyer, D. Jung, J. J. Novoa, and M.-H. Whangbo, Synth. Met. **42**, 1983 (1991).

[51] S. Lefebvre, P. Wzietek, S. Brown, C. Bourbonnais, D. Jérome, C. Mézière, M. Fourmigué, and P. Batail, Phys. Rev. Lett. **85**, 5420 (2000).

[52] K. Kanoda, J. Phys. Soc. Jpn. **75**, 051007 (2006).

[53] K. Kanoda, Physica C **282-287**, 299 (1997).

[54] P. Limelette, P. Wzietek, S. Florens, A. Georges, T. A. Costi, C. Pasquier, D. Jérome, C. Mézière, and P. Batail, Phys. Rev. Lett. **91**, 016401 (2003).

[55] D. Fournier, M. Poirier, M. Castonguay, and K. D. Truong, Phys. Rev. Lett. **90**, 127002 (2003).

[56] K. Frikach, M. Poirier, M. Castonguay, and K. D. Truong, Phys. Rev. B **61**, R6491 (2000).

[57] M. Dion, D. Fournier, M. Poirier, K. D. Truong, and A.-M. S. Tremblay, Phys. Rev. B **80**, 220511(R) (2009).

[58] M. Poirier, M. Dion, and D. Fournier, Phys. Rev. B **83**, 132507 (2011).

[59] G. Kotliar, S. Murthy, and M. J. Rozenberg, Phys. Rev. Lett. **89**, 046401 (2002).

[60] S. Onoda and M. Imada, J. Phys. Soc. Jpn. **70**, 3398 (2001).

[61] J. Merino and R. H. McKenzie, Phys. Rev. B **62**, 16442 (2000).

[62] C. Castellani, C. Di Castro, D. Feinberg, and J. Ranninger, Phys. Rev. Lett. **43**, 1957 (1979).

[63] W. Zheng, R. R. P. Singh, R. H. McKenzie, and R. Coldea, Phys. Rev. B **71**, 134422 (2005).

[64] K. Miyagawa, A. Kawamoto, Y. Nakazawa, and K. Kanoda, Phys. Rev. Lett. **75**, 1174 (1995).

[65] S. Yamashita, Y. Nakazawa, M. Oguni, Y. Oshima, H. Nojiri, Y. Shimizu, K. Miyagawa, and K. Kanoda, Nat. Phys. **4**, 459 (2008).

[66] A. P. Ramirez, Nat. Phys. **4**, 442 (2008).

[67] Y. Hayashi and M. Ogata, J. Phys. Soc. Jpn. **76**, 053705 (2007).

[68] M. Yamashita, N. Nakata, Y. Kasahara, T. Sasaki, N. Yoneyama, N. Kobayashi, S. Fujimoto, T. Shibauchi, and Y. Matsuda, Nat. Phys. **5**, 44 (2009).

[69] K. Nakamura, Y. Yoshimoto, T. Kosugi, R. Arita, and M. Imada, J. Phys. Soc. Jpn. **78**, 083710 (2009).

[70] H. C. Kandpal, I. Opahle, Y.-Z. Zhang, H. O. Jeschke, and R. Valentí, Phys. Rev. Lett. **103**, 067004 (2009).

[71] L. F. Tocchio, A. Parola, C. Gros, and F. Becca, Phys. Rev. B **80**, 064419 (2009).

[72] Y. Shimizu, K. Miyagawa, K. Kanoda, M. Maesato, and G. Saito, Phys. Rev. B **73**, 140407(R) (2006).

[73] H. Kawamura and S. Miyashita, J. Phys. Soc. Jpn. **53**, 4138 (1984).

[74] G. Baskaran, Phys. Rev. Lett. **63**, 2524 (1989).

[75] T. Grover and T. Senthil, Phys. Rev. B **81**, 205102 (2010).

[76] T. Grover, N. Trivedi, T. Senthil, and P. A. Lee, Phys. Rev. B **81**, 245121 (2010).

[77] Y. Zhou and P. A. Lee, Phys. Rev. Lett. **106**, 056402 (2011).

[78] S. Yamashita, T. Yamamoto, Y. Nakazawa, M. Tamura, and R. Kato, Nat. Commun. **2**, 275 (2011).

[79] T. Itou, A. Oyamada, S. Maegawa, M. Tamura, and R. Kato, Phys. Rev. B **77**, 104413 (2008).

[80] T. Itou, A. Oyamada, S. Maegawa, and R. Kato, Nat. Phys. **6**, 673 (2010).

[81] K. Kanoda and R. Kato, Annu. Rev. Condens. Matter Phys. **2**, 167 (2011).

[82] A. P. Ramirez, C. L. Broholm, R. J. Cava, and G. R. Kowach, Physica B **280**, 290 (2000).

[83] M. de Souza, P. Foury-Leylekian, A. Moradpour, J.-P. Pouget, and M. Lang, Phys. Rev. Lett. **101**, 216403 (2008).

[84] O. Drozdova, G. Saito, H. Yamochi, K. Ookubo, K. Yakushi, M. Uruichi, and L. Ouahab, Inorg. Chem. **40**, 3265 (2001).

[85] K. Kanoda, *et al.*, International Conference on Magnetism 2009 (*ICM09*), Karlsruhe, Germany, unpublished.

[86] A. Brühl, B. Wolf, V. Pashchenko, M. Anton, C. Gross, W. Assmus, R. Valentí, S. Glocke, A. Klümper, T. Saha-Dasgupta, B. Rahaman, and M. Lang, Phys. Rev. Lett. **99**, 057204 (2007).

[87] M. E. Fisher, Phil. Mag. **7**, 1731 (1962).

[88] B. Bernu and G. Misguich, Phys. Rev. B **63**, 134409 (2001).

[89] O. I. Motrunich, Phys. Rev. B **72**, 045105 (2005).

[90] M. Lang, R. S. Manna, M. de Souza, A. Brühl, and J. A. Schlueter, Physica B **405**, S182 (2010).

[91] A. Kawamoto, Y. Honma, and K. Kumagai, Phys. Rev. B **70**, 060510(R) (2004).

[92] I. Kézsmárki, Y. Shimizu, G. Mihály, Y. Tokura, K. Kanoda, and G. Saito, Phys. Rev. B **74**, 201101(R) (2006).

[93] M. Abdel-Jawad, I. Terasaki, T. Sasaki, N. Yoneyama, N. Kobayashi, Y. Uesu, and C. Hotta, Phys. Rev. B **82**, 125119 (2010).

[94] C. Hotta, Phys. Rev. B **82**, 241104(R) (2010).

[95] M. Naka and S. Ishihara, J. Phys. Soc. Jpn. **79**, 063707 (2010).

[96] R. T. Clay, H. Li, and S. Mazumdar, Physica B **405**, S253 (2010).

[97] H. Li, R. T. Clay, and S. Mazumdar, J. Phys.: Condens. Matter **22**, 272201 (2010).

[98] S. Dayal, R. T. Clay, H. Li, and S. Mazumdar, Phys. Rev. B **83**, 245106 (2011).

[99] M. de Souza, A. Brühl, J. Müller, P. Foury-Leylekian, A. Moradpour, J.-P. Pouget, and M. Lang, Physica B **404**, 494 (2009).

[100] M. Yamashita, T. Shibauchi, and Y. Matsuda, ChemPhysChem. **13**, 74 (2012).

[101] F. L. Pratt, P. J. Baker, S. J. Blundell, T. Lancaster, S. Ohira-Kawamura, C. Baines, Y. Shimizu, K. Kanoda, I. Watanabe, and G. Saito, Nature (London) **471**, 612 (2011).

[102] O. I. Motrunich, Phys. Rev. B **73**, 155115 (2006).

[103] L. N. Bulaevskii, C. D. Batista, M. V. Mostovoy, and D. I. Khomskii, Phys. Rev. B **78**, 024402 (2008).

[104] K. A. Al-Hassanieh, C. D. Batista, G. Ortiz, and L. N. Bulaevskii, Phys. Rev. Lett. **103**, 216402 (2009).

[105] M. Jeong, F. Bert, P. Mendels, F. Duc, J. C. Trombe, M. A. de Vries, and A. Harrison, Phys. Rev. Lett. **107**, 237201 (2011).

[106] R. S. Manna, M. de Souza, J. A. Schlueter, and M. Lang, Phys. Status Solidi C, 1-3 (2012).

[107] U. Geiser, H. H. Wang, K. D. Carlson, J. M. Williams, H. A. Charlier, J. E. Heindl, G. A. Yaconi, B. J. Love, M. W. Lathrop, J. E. Schirber, D. L. Overmyer, J. Ren, and M.-H. Whangbo, Inorg. Chem. **30**, 2586 (1991).

[108] T. Komatsu, T. Nakamura, N. Matsukawa, H. Yamochi, G. Saito, H. Ito, T. Ishiguro, M. Kusunoki, and K.-I. Sakaguchi, Solid State Commun. **80**, 843 (1991).

[109] G. C. Papavassiliou, D. J. Lagouvardos, A. Terzis, J. Amiell, C. Garrigou-Lagrange, P. Delhaès, B. Hilti, and J. Pfeiffer, Synth. Met. **61**, 267 (1993).

[110] H. Yamochi, T. Nakamura, T. Komatsu, N. Matsukawa, T. Inoue, G. Saito, T. Mori, M. Kusunoki, and K.-I. Sakaguchi, Solid State Commun. **82**, 101 (1992).

[111] H. Yamochi, T. Komatsu, N. Matsukawa, G. Saito, T. Mori, M. Kusunoki, and K. Sakaguchi, J. Am. Chem. Soc. **115**, 11319 (1993).

[112] X. H. Bu and P. Coppens, Z. Kristallogr. **212**, 103 (1997).

[113] X. Bu, A. Frost-Jensen, R. Allendoerfer, P. Coppens, B. Lederle, and M. J. Naughton, Solid State Commun. **79**, 1053 (1991).

[114] H. O. Jeschke, M. de Souza, R. Valentí, R. S. Manna, M. Lang, and J. A. Schlueter, Phys. Rev. B **85**, 035125 (2012).

[115] K. Miyake and H. Kohno, J. Phys. Soc. Jpn. **74**, 254 (2005).

[116] H. Kikuchi, Y. Fujii, M. Chiba, S. Mitsudo, and T. Idehara, Physica B **329-333**, 967 (2003).

[117] F. Zigan and H. D. Schuster, Z. Kristallogr. **135**, 416 (1972).

[118] V. G. Gattow and J. Zemann, Acta Cryst. **11**, 866 (1958).

[119] K. C. Rule, M. Reehuis, M. C. R. Gibson, B. Ouladdiaf, M. J. Gutmann, J.-U. Hoffmann, S. Gerischer, D. A. Tennant, S. Süllow, and M. Lang, Phys. Rev. B **83**, 104401 (2011).

[120] S. Köhler, Diploma Thesis, J. W. Goethe-Universität Frankfurt (2009).

[121] M. C. R. Gibson, K. C. Rule, A. U. B. Wolter, J.-U. Hoffmann, O. Prokhnenko, D. A. Tennant, S. Gerischer, M. Kraken, F. J. Litterst, S. Süllow, J. Schreuer, H. Luetkens, A. Brühl, B. Wolf, and M. Lang, Phys. Rev. B **81**, 140406(R) (2010).

[122] P. T. Cong, B. Wolf, R. S. Manna, M. de Souza, U. Tutsch, A. Brühl, J. Schreuer, S. Süllow, and M. Lang, (2011) (unpublished).

[123] F. Aimo, S. Krämer, M. Klanjšek, M. Horvatić, C. Berthier, and H. Kikuchi, Phys. Rev. Lett **102**, 127205 (2009).

[124] F. Wolff-Fabris, S. Francoual, V. Zapf, M. Jaime, B. Scott, S. Tozer, S. Hannahs, T. Murphy, and A. Lacerda, J. Phys. Conf. Ser. **150**, 042030 (2009).

[125] M. Lang, A. Brühl, V. Pashchenko, K. Removic-Langer, Y. Tsui, U. Tutsch, B. Wolf, T. Kretz, W. Lerner, M. Wagner, and J. Schreuer, J. Phys. Conf. Ser. **51**, 1 (2006).

[126] K. C. Rule, A. U. B. Wolter, S. Süllow, D. A. Tennant, A. Brühl, S. Köhler, B. Wolf, M. Lang, and J. Schreuer, Phys. Rev. Lett. **100**, 117202 (2008).

[127] H. Jeschke, I. Opahle, H. Kandpal, R. Valentí, H. Das, T. Saha-Dasgupta, O. Janson, H. Rosner, A. Brühl, B. Wolf, M. Lang, J. Richter, S. Hu, X. Wang, R. Peters, T. Pruschke, and A. Honecker, Phys. Rev. Lett. **106**, 217201 (2011).

[128] B. Gu and G. Su, Phys. Rev. Lett. **97**, 089701 (2006).

[129] K. C. Rule, D. A. Tennant, J.-S. Caux, M. C. R. Gibson, M. T. F. Telling, S. Gerischer, S. Süllow, and M. Lang, Phys. Rev. B **84**, 184419 (2011).

[130] A. Brühl, Ph.D. Thesis, J. W. Goethe-Universität Frankfurt (2007).

List of Figures

1.3.1 Schematic diagram of the conduction band in the case of a three-quarter filling and half filling . . . 19
1.6.1 Schematic diagram of the distorted diamond-chain model with exchange couplings constants . . . 24

2.1.1 Typical single crystal of organic conductors . . . 28
2.1.2 Picture of the sample after mounting inside the dilatometer cell . . . 29
2.2.2 The dilatometer cell is placed inside the pressure cell via an L-piece. . . . 30
2.2.1 Complete overview of the pressure cell . . . 31
2.2.3 Construction of the dilatometer cell . . . 32
2.2.4 Complete overview of the cryostat insert . . . 33
2.2.5 Concentric construction of the lower part of the cryostat insert . . . 34
2.2.6 Detailed construction of the lower section of the insert before and after insertion of the inner copper can . . . 36
2.2.7 Readout of the pressure sensor for a temperature sweep in measurements on azurite at $P \approx 9.5$ MPa . . . 37
2.2.8 Picture of the whole setup 'thermal expansion under pressure' . . . 39
2.6.1 The variation of the dielectric constant (ε_r) for a van der Waals gas (^4He) as a function of temperature for different constant pressure values . . . 44
2.6.2 The variation of the dielectric constant (ε_r) for a van der Waals gas (^4He) as a function of pressure while the temperature ($T = 302.3$ K) is fixed . 44
2.6.3 Cell effect as a function of temperature for different finite pressure values 45

3.1.1 Temperature-pressure phase diagram of quasi-one-dimensional TMTTF and TMTSF charge-transfer salts . . . 48
3.2.1 Structure of the BEDT-TTF (ET) molecule . . . 49
3.2.2 Schematic packing motifs of the ET molecules . . . 49
3.2.3 Structure of the κ-phase of the quasi-2D organic charge-transfer salts . . 50

3.2.4 T-P phase diagram of the κ-$(ET)_2X$ salts with the anion $X = Cu[N(CN)_2]Br$, $Cu[N(CN)_2]Cl$ . . . 51
3.3.1 Temperature dependence of the relative sound velocity for κ-$(ET)_2Cu[N(CN)_2]Cl$ compound under helium gas pressure . . . 52
3.4.1 Singular part of the thermal expansivity α_{sing} as a function of t and h . . 53

4.0.1 Magnetic susceptibility as a function of temperature for a polycrystalline sample of the spin-liquid compound κ-$(BEDT\text{-}TTF)_2Cu_2(CN)_3$ in comparison to the κ-$(BEDT\text{-}TTF)_2Cu[N(CN)_2]Cl$ compound . . . 56
4.0.2 Temperature dependence of ^{1}H-NMR spectra for the single crystals of κ-$(BEDT\text{-}TTF)_2Cu_2(CN)_3$ and κ-$(BEDT\text{-}TTF)_2Cu[N(CN)_2]Cl$ . . . 57
4.0.3 The temperature-pressure phase diagram of the spin-liquid compound κ-$(BEDT\text{-}TTF)_2Cu_2(CN)_3$ . . . 58
4.0.4 Specific heat and thermal conductivity measurements at low-temperature used to obtain the low-lying excitations in κ-$(BEDT\text{-}TTF)_2Cu_2(CN)_3$ . . 58
4.0.5 Crystal structure of the κ-phase charge-transfer salts and the theoretical dimer-dimer interaction model . . . 59
4.0.6 Mysterious 6 K anomaly of κ-$(BEDT\text{-}TTF)_2Cu_2(CN)_3$ detected by specific heat and thermal conductivity measurements . . . 60
4.1.1 Uniaxial expansivities α_i of κ-$(BEDT\text{-}TTF)_2Cu_2(CN)_3$ along the in-plane $i = b$ and c axes and along the out-of plane $i = a$ axis . . . 61
4.1.2 In-plane (bc) expansivities α_i of κ-$(BEDT\text{-}TTF)_2Cu_2(CN)_3$ on expanded scales around the 6 K phase transition . . . 63
4.1.3 The temperature dependence of the volume expansion coefficient (β) of κ-$(BEDT\text{-}TTF)_2Cu_2(CN)_3$ . . . 64
4.2.1 The specific heat data of κ-$(BEDT\text{-}TTF)_2Cu_2(CN)_3$ between the temperatures 2 K and 10 K . . . 65
4.2.2 Phase transition anomalies at 6 K observed by means of thermal expansion, specific heat and the derivative of the magnetic susceptibility . . . 66
4.3.1 Magnetic phase diagram of κ-$(BEDT\text{-}TTF)_2Cu_2(CN)_3$ based on μSR and NMR measurements for different magnetic field ranges . . . 69
4.3.2 Magnetic field dependence along the b-axis in terms of relative length changes for a particular high-quality sample (batch - KAF 5078#1) . . . 71
4.3.3 Relative length changes as a function of temperature measured at a very slow rate of $\pm$ 1.5 K/hour for the magnetic field $B = 8$ T . . . 73
4.3.4 Plot of the $\Delta l_b/l_b$ data at $B = 0$ and 10 T from Fig. 4.3.2 without employing a vertical shift . . . 74
4.3.5 Magnetostriction measurements at the temperature $T = 6$ K . . . 75
4.3.6 Position of the B-induced anomalies in $\Delta l_b/l_b$ for B applied parallel to the b-axis . . . 76
4.3.7 Modified version of the phase diagram, reported by the ref. [101] by including the positions of the anomalies obtained from the thermal expansion and magnetostriction measurements . . . 77

4.3.8 Sample-to-sample dependence of α_b and comparison of the relative length changes as a function of temperature under magnetic field 8 T for two different samples 78
4.4.1 Relative lattice parameters normalized to their values at $T = 20$ K, as a function of temperature 79
4.4.2 Temperature dependence of nearest-neighbor hopping integrals (t and t') and interaction strength (U/t) 80
4.4.3 Ratio of the in-plane c and b lattice vectors as a function of temperature 81

5.0.1 Chemical structure of azurite together with the exchange interactions . . 83
5.0.2 Ground states of the $S = 1/2$ distorted diamond-chain model consisting of ferrimagnetic phase, the spin-fluid (SF) state and the dimerized phase 84
5.0.3 The phase diagram of the distorted diamond-chain model in the $\tilde{J}_2$-$\tilde{J}_3$ plane 85
5.0.4 Low-temperature specific heat data showing three distinct anomalies . . . 86
5.0.5 Temperature dependance of the magnetic susceptibility of azurite for the magnetic field parallel and perpendicular to the b-axis 87
5.0.6 Magnetization measurements as a function of magnetic field for azurite taken at different constant temperatures 88
5.1.1 Thermal expansion measurements of azurite along the chain direction, *i.e.*, b-axis at ambient-pressure 89
5.3.1 The variation of the thermal expansion coefficient as a function of temperature of azurite along the chain direction, *i.e.*, b-axis at ambient and finite pressure values 92
5.3.2 Pressure dependence of the Néel ordering temperature T_N 94
5.3.3 Temperature variation of the thermal expansion of azurite at ambient and finite pressure values after taking into account the 'pressure-induced cell effect' 95

List of Tables

1.1 The values of the critical exponents (α, β, γ and δ) of Ising, XY and Heisenberg universality classes 20

4.1 Crystal structure data of κ-(BEDT-TTF)$_2$Cu$_2$(CN)$_3$ for the different constant temperatures by performing single crystal X-ray diffraction measurements 78

5.1 Exchange coupling constants based on full potential local orbital (*FPLO*) method with GGA+U calculations 88

Acknowledgements

I would like to acknowledge my sincere thanks to my supervisor Prof. Dr. Michael Lang for his guidance during my doctoral studies. It would have been difficult to complete this thesis in its present form without his support. I still remember the first day in Germany when he met me at the airport. I would like to thank him specially for giving me such innovative ideas during setting up the instrument 'thermal expansion under pressure'. It was really nice to work with him in the laboratory and to discuss physics time and again during my doctoral studies.

I would like to thank my second supervisor Prof. Dr. Martin Aeschlimann from the University of Kaiserslautern for discussing my work status and for helping me to suggest future plans during my PhD studies. I also thank Dr. John A. Schlueter from Argonne National Laboratory, USA for providing the spin-liquid samples.

I also give thanks to Dr. Mariano de Souza for introducing to me the 'thermal expansion (ambient-pressure)' setup. Thanks also go to Dr. Andreas Brühl, PD Dr. Bernd Wolf, Dr. Ulrich Tutsch for providing me useful information during experiments. It was really good to have such colleagues like Thanh Cong Pham, Sebastian Köhler and Georg Hofmann. We used to discuss frequently about experiments, physics and many other social topics! Special thanks go to Sebastian for helping me to learn all sorts of "computerese" like Test point programming, Latex writing and also for helping me to write German "Kurzfassung". I would like to express my sincere thanks to Mathias Holzhauer, Alexander Büßer, Dr. Katarina Removic-Langer, Christian Strack, Daniel Hofmann, Christian Balz, Friedrich Freund, Frank Schnelle, Stephan Knöner, Elena Gati, Lucas Hinz, Lars Postulka, and Dr. Harald Schubert for their help during my work in the laboratory. Special thanks to Siegfried Rapphahn who supplied liquid N_2 and helium when these were needed. It is my pleasure to thank Thomas Dübel and Friedhelm Isselbächer for providing, and support in the smooth flow of the general running of the laboratory. I would also like to thank all the people in the mechanical as well as the electronic work-

shops who designed/ repaired many parts on many occasions.

I thank Dr. Deepshikha Jaiswal-Nagar for her support during my PhD studies. It was really helpful to discuss physics with her. Not only discussing Physics but also spending times with her discussing the normal things in life which was also helpful.

Thanks goes to Dr. Andreas Kreisel for discussing the dielectric constant problem of helium. It was a pretty good time for me to spend time with Dr. Pintu Das discussing physics and providing positive motivation at all times. Thanks go to Dr. Sridhar Sreeramulu for his help to learn Latex precisely. I would like to thank Dr. Amir Haghighirad for annealing samples and discussing physics.

I would like to thank Carolyne Agnew for helping me to fill out official documents, checking my english and also to discuss traveling plans in Europe! I thank her also for the proofreading of this thesis. Moreover it was really nice to spend times with such a friendly person.

I would like to acknowledge SFB/ TR 49 for funding during my PhD studies. Because of this I had the opportunity to meet many prestigious people in our field of research. I would also like to thank 'GRADE - Goethe Graduate Academy' and all the organizers of GRADE for organizing interesting workshops, mainly soft skills related to doctoral studies.

Special thanks to Prof. Dr. K. G. Suresh and Prof. Dr. G. Mukhopadhyay from Indian Institute of Technology Bombay for giving me recommendation letters and positive suggestions all the time.

It was nice to discuss physics with Prof. Dr. Takahiko Sasaki from Tohoku University, Japan. I would like to thank him.

Without learning the language, it is really difficult to stay in a foreign country. I was grateful for the chance to learn the German language at our University. I would like to thank my German teacher Kerstin Sharaka for her nice teaching and telling me much about "Deutschland".

I would like to thank Swami Baneshananda, Swami Bhaswatananda, Swami Amiteshananda, Swami Atmapriyananda, Dilip Kumar Banerjee for their constant inspiration throughout my journey.

The acknowledgements would not be complete if I did not include some of my friends. Dr. Mithun Biswas was one of them, a close friend for a long time with whom I discussed plenty of things regarding physics and other subjects. I was lucky to have some friends like Dr. Rajsekhar Paul, Dr. Devrishi Goswami and Anirban Roy. It was really fun to

have them.

Finally I would like to express my sincere thanks to my parents and brothers for their constant support. Without them I cannot imagine anything. It was really hard to be away from them. Once upon a time I thought that going to Kolkata from my island would be a goal in my life. To come to this stage of my life has not been possible without their constant support and sacrifice.

Rudra Sekhar Manna
Frankfurt am Main, 2012

Curriculum Vitae

Personal Details

Name:	Rudra Sekhar Manna
Date of birth:	21.August 1984
Place of Birth:	Gobindapur Abad (India)
Nationality:	Indian

University Education

- 10/2007 - 01/2012 - PhD (J. W. Goethe-Universität Frankfurt) in Frankfurt am Main, Germany
  Advisor: Prof. Dr. Michael Lang
- 11/2006 - 10/2007 - Researcher (Pohang University of Science and Technology) in Pohang, South Korea
  Advisor: Prof. Dr. Kwang S. Kim
- 07/2006 - 10/2006 - Junior Research Fellow (Indian Institute of Technology Bombay) in Mumbai
  Advisor: Prof. Dr. K. G. Suresh
- 2004 - 2006 - Master in Physics (Indian Institute of Technology Bombay) in Mumbai
  Master thesis - Advisor: Prof. Dr. K. G. Suresh
- 2001 - 2004 - Bachelor in Physics (Ramakrishna Mission Vidyamandira, Calcutta University) in Howrah, West Bengal

School

- 1997 - 2001 - High School (Debnagar Mokshoda Dinda Higher Secondary School)
- 1993 - 1997 - Junior High School (Gobindapur Abad Bipin Bihari Sikhaniketan)
- 1990 - 1993 - Primary School (Gobindapur Basic School)
- 1987 - 1990 - Primary School (Sridharnagar Subhash Chandra Primary School)

- Experienced user of Sci-finder, Microsoft word, Latex, Microsoft Power Point, Origin.
- Computing Skills: Windows, Linux, Fortran-90.
- Language Skills: Bengali, English, Hindi, German.

LIST OF PUBLICATIONS

1. "Lattice effects and entropy release at the low-temperature phase transition in the spin-liquid candidate κ-(BEDT-TTF)$_2$Cu$_2$(CN)$_3$" - **R. S. Manna**, M. de Souza, A. Brühl, J. A. Schlueter, and M. Lang, *Physical Review Letters* **104**, 016403 (2010).

2. "Phase transition and lattice distortion in the proposed spin-liquid system κ-(BEDT-TTF)$_2$Cu$_2$(CN)$_3$" - M. Lang, **R. S. Manna**, M. de Souza, A. Brühl, and J. A. Schlueter, *Physica B: Condensed Matter* **405**, S182 (2010).

3. "Field-induced length changes in the spin-liquid candidate κ-(BEDT-TTF)$_2$Cu$_2$(CN)$_3$" - **Rudra Sekhar Manna**, Mariano de Souza, John A. Schlueter, and Michael Lang, *physica status solidi C*, 1-3 (2012).

4. "Temperature dependence of structural and electronic properties of the spin-liquid candidate κ-(BEDT-TTF)$_2$Cu$_2$(CN)$_3$" - Harald O. Jeschke, Mariano de Souza, Roser Valentí, **Rudra Sekhar Manna**, Michel Lang, and John A. Schlueter, *Physical Review B* **85**, 035125 (2012).

5. "High-resolution thermal expansion measurements under helium gas pressure" - **Rudra Sekhar Manna** and Michael Lang, (2012) (*in preparation*).

6. "Elastic and magneto-acoustic properties of distorted diamond-chain compound azurite" - P. T. Cong, B. Wolf, **R. S. Manna**, M. de Souza, U. Tutsch, A. Brühl, J. Schreuer, S. Süllow, and M. Lang, (2012) (*in preparation*).

Other Publications

1. "Magnetic Properties of $CoFe_2O_4$ synthesized by solid State, citrate precursor and polymerized complex methods: A comparative study" - P.C. Rajath Varma, **Rudra Sekhar Manna**, D. Banerjee, Manoj Raama Varma, K.G. Suresh, and A.K. Nigam, *Journal of Alloys and Compounds* **453**, 298 (2008).

2. "Controlling metal nanotoppings on the tip of silicide nanostructures" - In Chul Hwang, Rajesh Kumar, Nam Dong Kim, Young Chun, Jung Woo Lee, Pavan Kumar,

Rudra S Manna, Changhoon Choi, Jae Rhung Lee, and Kwang S Kim, *Nanotechnology* **20**, 245605 (2009).

TALKS

1. Thermodynamic studies on the proposed 2D spin-liquid state in κ-$(ET)_2Cu_2(CN)_3$ - German spring meeting (Deutsche Physikalische Gesellschaft) - Dresden, Germany (22nd-27th March, 2009).

2. Invited talk: Collective phenomena in organic charge-transfer salts at very low-temperature - Ramakrisha Mission Vidyamandira, Belur Math, India (24th April, 2009).

3. Anomalous lattice effects in the proposed 2D spin-liquid state in κ-(BEDT-TTF)$_2$Cu$_2$(CN)$_3$ - International Conference on Magnetism (ICM) - Karlsruhe, Germany (26th-31st July, 2009).

4. Thermal expansion studies on the proposed 2D spin-liquid state in κ-(BEDT-TTF)$_2$Cu$_2$(CN)$_3$ - TR 49 College (SFB): Student workshop - Seehotel Gelterswoog, Kaiserslautern (10th-11th September, 2009).

5. Lattice effects and entropy release at the low-temperature phase transition in κ-(BEDT-TTF)$_2$Cu$_2$(CN)$_3$ - Annual retreat SFB/TR 49 - Akademie Gesundes Leben, Oberursel (24th -25th September, 2009).

6. Thermodynamic studies showing anisotropic lattice effects and entropy release at the mysterious 6 K phase transition in κ-(BEDT-TTF)$_2$Cu$_2$(CN)$_3$- studierendenseminar zur Festkoerperphysik (Departmental solid state physics student seminar) - Physikalisches Institut, J. W. Goethe-Universität Frankfurt (25th January, 2010).

7. Thermal expansion under pressure - measurements on azurite, $Cu_3(CO_3)_2(OH)_2$ - TR 49 College (SFB): Student workshop - Weingut Sandwiese, Worms, Germany (23rd-25th February, 2011).

8. Field-induced thermal expansion in the spin-liquid candidate κ-$(ET)_2Cu_2(CN)_3$ - Annual retreat SFB/TR 49 - Best Western Alzey, Germany (15th-16th September, 2011).

PRESENTED POSTERS IN CONFERENCES

1. Lattice effects and entropy release at the low-temperature phase transition in κ-(BEDT-TTF)$_2$Cu$_2$(CN)$_3$ - Annual retreat SFB/ TR 49 - Akademie Gesundes Leben,

Oberursel (24th -25th September, 2009).

2. Collective phenomena in organic charge-transfer salts close to the Mott transition - SFB International Symposium on "Novel states in correlated condensed matter - from model systems to real materials" - Berlin, Germany (2nd-4th March, 2010).

3. Field-induced effects near the mysterious low-temperature phase transition in the proposed spin-liquid system κ-(BEDT-TTF)$_2$Cu$_2$(CN)$_3$- German spring meeting (Deutsche Physikalische Gesellschaft) - Regensburg, Germany (21st-26th March, 2010).

4. Collective phenomena in organic charge-transfer salts close to the Mott transition - Annual retreat SFB/ TR 49 - Seehotel Gelterswoog, Kaiserslautern, Germany (7th-8th October, 2010).

5. Thermal expansion under pressure - test measurements on azurite, $Cu_3(CO_3)_2(OH)_2$ - German spring meeting (Deutsche Physikalische Gesellschaft) - Dresden, Germany (13th-18th March, 2010).

6. Field-induced thermal expansion in the spin-liquid candidate κ-(ET)$_2$Cu$_2$(CN)$_3$ - Annual retreat SFB/ TR 49 - Best Western Alzey, Germany (15th-16th September, 2011).

7. Field-induced length changes in the spin-liquid candidate κ-(ET)$_2$Cu$_2$(CN)$_3$ - 9th International Symposium on Crystalline Organic Metals, Superconductors and Ferromagnets (ISCOM 2011) - Gniezno, Poznań, Poland (25th-30th September, 2011).

TEACHING ASSISTANTSHIP

1. Winter Semester 2007-2008 - Teaching Assistant for the experiment "*Infrared Spectroscopy*" - Advance laboratory course for Physics students, J. W. Goethe-Universität Frankfurt, Germany.

2. Summer Semester 2008, Winter Semester 2008-2009, Summer Semester 2009, Winter Semester 2009-2010, Summer semester 2010, Winter Semester 2010-2011, Summer semester 2011 - Teaching Assistant for the experiment "*Magnetic Resonance (NMR)*" - Advance laboratory course for Physics students, J. W. Goethe-Universität Frankfurt, Germany.

3. Summer Semester 2009 - Teaching Assistant for the experiment "*Sound Propagation is Crystals*" - Advance laboratory course for Physics students, J. W. Goethe-Universität Frankfurt, Germany.

4. Summer Semester 2011, winter semester 2011-2012 - Teaching Assistant for the

experiment "*Josephson Effect*" - Advance laboratory course for Physics students, J. W. Goethe-Universität Frankfurt, Germany.

PROFESSIONAL ACTIVITIES AND HONORS RECEIVED

- German language course of level B2 has been completed - J. W. Goethe-Universität Frankfurt, Germany.
- Qualified German language course of level A1 (GOETHE-ZERTIFIKAT A1) with a grade sehr gut (very good) from Goethe Institute-Frankfurt, Germany.
- Junior Research Fellow (Physics) in 2006, Indian Institute of Technology Bombay.
- Master of Science (Physics) in 2006, Indian Institute of Technology Bombay.
- Ranked 63 (general) in JAM (Joint Admission Test to M.Sc.) in Physics all over the India.
- First class in Bachelor of Science (Physics) in 2004, University of Calcutta.